UNIVERSITÀ DEGLI STUDI DI GENOVA
SCUOLA POLITECNICA

Department of Mechanical, Energy, Management and Transportation Engineering

Research Doctorate: MACHINE AND SYSTEMS ENGINEERING FOR ENERGY, ENVIRONMENT AND TRANSPORT

Curriculum: Machine and System Engineering for Energy, Environment and Propulsion

"Design and commissioning of a rotating test facility simulating a LPT hub cavity system for the investigation of cavity flows in aeroengines"

Tutor: Prof. Eng. *Daniele Simoni*

Author: *Roberto Guida*

SUMMARY

NOMENCLATURE

a	Cavity Inner Radius	[mm]
A	Labyrinth Seal Passage Area	[mm^2]
b	Cavity Outer Radius	[mm]
C	Vane Chord	[mm]
C_z	Vane Axial Chord	[mm]
d	Distance from Vane Trailing Edge	[mm]
D	Diameter	[mm]
g	Vane Pitch Length	[mm]
L	Cavity Streamwise Length	[mm]
$\dot{m}$	Mass Flow Rate	[kg/s]
n	Blade/Vane Count	
p	Static Pressure of the Fluid	[Pa]
p_{amb}	Ambient Pressure	[Pa]
p_t	Total Pressure of the Fluid	[Pa]
R	Labyrinth Seal Radius	[mm]
R_{tip}	Main Annulus Tip Radius	[mm]
R_{gas}	Gas Constant	[J/kg K]
r	Radial Coordinate	[mm]
s	Axial Rotor-Stator Inner Cavity Distance	[mm]
s_c	Cavity Rim Seal Clearance	[mm]
S	Span	[mm]
T_t	Total Temperature	[K]
v	Velocity	[m/s]
y	Pitchwise Length	[mm]
z	Axial Coordinate	[mm]
α	Absolute Flow Angle	[°]
Δp	Pressure Difference	[Pa]

μ	Dynamic Viscosity	[Pa s]
ν	Kinematic Viscosity	[m^2/s]
ρ	Flow Density	[kg/m^3]
τ	Shear Stress	[Pa]
Φ	Circumferential Coordinate	[°]
ω	Flow Angular Velocity	[rad/s]
Ω	Disk Rotational Speed	[rad/s]

Dimensionless

C_D	Discharge Coefficient	$\dot{m}/\dot{m}_{id}$
C_w	Non Dimensional Mass Flow Rate	$\dot{m}/\mu r$
C_p	Static Pressure Coefficient	$(p - p_{amb})/\Delta p_{vane}$
C_{p_t}	Total Pressure Coefficient	$\frac{p_{t,1}(r,y) - p_{t,2}(r,y)}{0.5\rho v_{2,id}^2}$
$C_{\overline{p_t}}$	Averaged Total Pressure Coefficient	$\frac{\overline{p_{t,1}}(r) - \overline{p_{t,2}}(r)}{0.5\rho v_{2,id}^2}$
$C_{\overline{p_{t,1}}}$	Non dimensional Inlet Total Pressure	$\frac{p_{amb} - \overline{p_{t,1}}(r)}{p_{amb} - \overline{p_{t,mid}}}$
Ma	Isentropic Mach Number	$\frac{v}{\sqrt{kR_{gas}T}}$
Re	Reynolds Number	$\frac{v_z L}{\nu}$
S_w	Swirl Factor	$\frac{v_\phi}{\Omega r}$
Tu	Turbulence Intensity	
β	Total to Static Pressure Ratio	p_t/p
φ	Flow Coefficient	$\frac{v_{z,}}{\Omega r}$

Subscript and Superscript

0	Stationary Quantities
c	Coolant Flow
eff	Effective Leakage Value
ent	Entrained Flow
FP	Main Annulus Flow Path Value
id	Ideal Adiabatic Iso-Entropic
l	Leakage Flow Quantities
mid	Main Annulus at Midspan
rim	Rim Seal Flow Quantities
1	Inlet Vane Plane
2	Outlet Vane Plane
$\bar{}$	Pitchwise Averaged Quantities

Chapter 1 - INTRODUCTION

Modern aeroengines need to be more efficient and contribute to the reduction on environmental impact of air transportation. They must reach dedicated standards of performance by reducing emissions and creating significant savings in operating costs. In order to ensure the technological breakthrough, new aeroengines are designed to have higher overall pressure ratios (OPR) to increase the thermal efficiency and higher by-pass ratios (BPR) to improve the propulsive efficiency, leading to smaller and hotter high pressure cores. To achieve these goals, there is the necessity to develop adequate technologies in order to adapt sub-systems to the new constrains of temperature and pressure.

Interstage cavities in the low pressure turbine (LPT) modules are one of the most relevant components in engine sub-systems. The cavities are located adjacent to the hub in order to avoid contact between the rotor and the static disks. On the other hand, they constitute an alternative path to the mainstream through the stator row. Consequently, a portion of the main annulus flow can be ingested into the cavity and flows through it due to the vane pressure drop. This leakage flow represents a direct source of losses for the engine since the pressure reduction is achieved only by loss generation resulting in a lower enthalpy of the cavity flow than the main annulus, but accompanied by a significant entropy rise. The ingestion of hot gasses in the rotor-stator wheelspace can lead to the overheating of the disks, reducing the component life.

Contactless sealing systems, such as labyrinth seals, are installed within the cavity to reduce the amount of leakage fluid. In addition, a proper amount of cold air is delivered to prevent overheating of the disks as well as to pressure sealing the cavity in order to avoid or limit the ingestion of hot gasses. These cooling flows are bled from compressor stage, around 20% of the main flow rate, and thus have a parasitic effect on engine performances. It is straightforward that increasing the OPR, hence the vane pressure drop, the amount of leakage flow and the required coolant flow rate as well, will suddenly increase. An additional source of losses is related to the flow entering and leaving the cavity that interacts with main annulus flow in the close to the hub region altering the main flow properties. Particularly, a reduction of flow incidence at the subsequent row inlet and stronger secondary flow structures are caused.

The research on this component is mainly focused on providing a major understanding of the cavity flow behaviour and its related effects on the stage efficiency in order to support the design of new optimized geometry. Particularly, it is of considerable importance the development of tools that allow predicting the amount of leakage fluid that pass through the

cavity and the coolant flow rate needed to prevent thermomechanical failure of the disks for every operating conditions of the engine.

To this end, CFD methods are used with increasing frequency for the analysis of flows in rotating cavities. However, these components are characterized by a rotational dominated flow and a shear driven mixing region within the cavity and at the rim as well. These phenomena are poorly reproduced by Reynolds-Averaged Navier Stokes (RANS) approaches. On the other hand, Large Eddy Simulations (LES) techniques are much more reliable but computationally expensive. However, the prediction of wall bounded flows is still inherently problematic for LES computations. Therefore, representative test facilities are of great importance for providing accurate experimental data and validate CFD results as well.

Taking into account these considerations, a dedicated test facility for cavity flow investigations has been designed and commissioned through this Ph.D. research activity. The rig is installed at the Aerodynamics and Turbomachinery Laboratory of the University of Genova. The test section has been equipped with a realistic cavity geometry located at the bottom of a LPT vane row and two secondary air systems simulating cold air injection in the cavity. The cavity is reproduced with an increased length scale of 50% with respect to engine dimensions in order to increase the spatial resolution of the problem and to facilitate the access to the probes. The rotational speed, cavity pressure ratio and the coolant flow rate ejected into the cavity can be independently adjusted in order to reproduce a wide set of different operating conditions of the engine. In addition, the rig has been designed with a modularity concept in order to allow an easy substitution of test section components to investigate different geometries. Finally, the facility has been heavily instrumented in order to provide an in deep characterization of the flow evolving within the cavity and in the main annulus as well.

The experimental results presented in this thesis highlight the capabilities of the new rig to provide an extensive description of the cavity flow related effects, as well as to indicate the effects due to the different parameters on the cavity flow and mainstream aerodynamic behavior. Particularly, large efforts have been made to develop a calibration procedure for measuring the leakage mass flow rate during the tests. Tests conducted with a “locked flow path” configuration allow formulating a calibration function linking the leakage mass flow rate with the pressure drop of the flow across the seal, which has been adopted to evaluate the discharge coefficient of the cavity. Further measurements have investigated the effect of the coolant flow and rotational speed on the cavity flow, particularly revealing the coolant flow rate that prevent the ingestion of gasses from the main annulus. Finally, measurements of the total pressure distributions in the main annulus reveal the influence of the coolant flow rate and the rotational speed variation on the secondary flow structures of the vane. This complex

interaction mechanism, due to the cavity presence, should be properly accounted for during the design phase of the stage, and correctly reproduced in simplified cascade testing.

The rig realization and experimental campaign are part of a research joint between the University of Genova and *AvioAero-a GE Aviation Business* that provided the cavity geometry and supported the test program. The research leading to these results has been carried out in the frame of the European research project E-Break and received founding from the European Seventh Framework Program (FP7/2007-2013).

Chapter 2 - LITERATURE REVIEW

The aim of this chapter is to give an overview of the governing flow physics associated to hub interstage cavities of LPT modules in aeroengines and a review of the relevant researches on this topic. The flow evolving in these components is complex since it is strongly affected by the pressure drop across the stage, the rotation of the disk and the cooling flow. The interaction between the cavity and the main annulus flow further contribute to make complex the overall flow field. Therefore, in the first section of this chapter a description of the flow field that is expected to establish in the cavity is given in order to distinguish each factor in turn. Then, each factor will be described in detail.

2.1 Expected Cavity Flow Field

A typical geometry of a hub interstage cavity system in provided in figure 2.1. The high rotational speed of the engine requires avoiding contact between rotor and stator disks. Therefore, the space between the rotor disks and the stator, named "wheelspace", is constituted by two rotor-stator cavities upstream and downstream of the vane row that are separated by an interstage labyrinth seal. Rim seals are located at the outer radius of the cavities and separate the flow into the wheelspace from the mainstream.

The literature review, presented in this chapter, allows the identification of four different flow patterns developing into the wheelspace that interact to establish the actual flow field. They are schematically represented in figure 2.2 and listed in the following:

1. The leakage flow that passes through the cavity due to stage pressure ratio;
2. The flow field established between rotor and stator discs in the two cavities;
3. The cooling flow introduced in the fore cavity;
4. The flow evolving at the rim of the cavity that interacts with the mainstream;

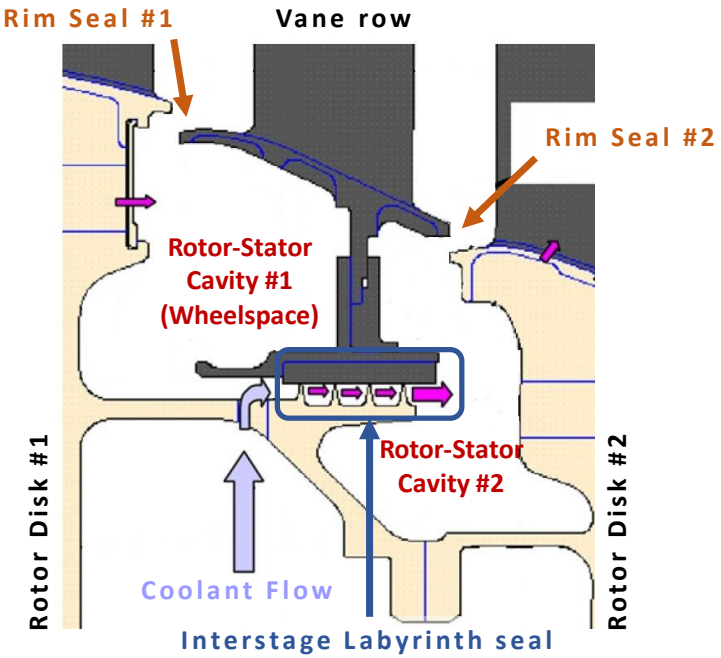

Figure 2.1 Typical geometry of an interstage hub cavity system

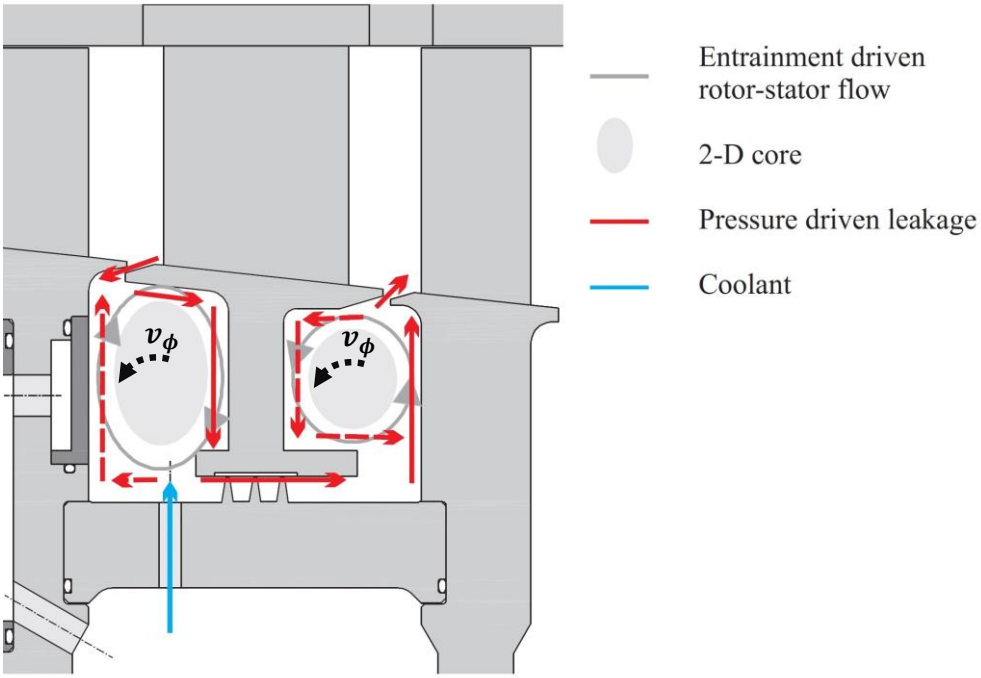

Figure 2.2 Representation of the flows that characterize the wheelspace

In an idealized environment without cooling air or rotation, the pressure drop across the vane row drives the passage of flow through the cavity and its amount depends on the discharge behavior of the labyrinth seal. This “leakage flow”, in steady conditions, constitutes the amount of hot gasses that is ingested from the upstream rim seal into the wheelepace and ejected through the downstream rim clearance.

The rotation of the disk strongly influences the wheelspace fluid motion. The viscous boundary layer of the rotating disk entrains flow from the bottom of the cavities and pumps it radially outward. The presence of the rim seals, that shroud the wheelspace, induces a recirculation of fluid where the entrained flow, pumped radially outward on the rotor surface, is supplied by a radial inflow along the stator wall. In this environment, the leakage flow is superposed to the fluid motion induced by the rotor pumping effect and could act feeding or interrupting the viscously dominated near-wall recirculation.

The recirculating flow is confined to the viscously dominated near wall region. If the distance between the disks is large compared to their radius, the boundary layers on the static and rotating walls remains separated. Then, an inviscid bi-dimensional “core flow” could establish in between. This core fluid possesses null radial and axial velocities but rotates at an intermediate rotational speed between the rotor and the stator.

The presence of the coolant further complicates the actual flow field. The coolant is supplied through the rotor disk with the double aim of providing a direct cooling of the components, in order to prevent thermomechanical failure of the discs, and to prevent the ingestion of hot gas from the outer path by pressure sealing the wheelspace. At low coolant flow rates, depending on the geometry, a portion of the coolant may supply the leakage flow without interacting with the inner cavity flow. The residual coolant remains entrained into disc pumped recirculation, hence feeding the flow recirculation described above. As the coolant flow rate is increased, the viscously dominated near wall region is gradually enlarged and starts altering the inviscid bi-dimensional core. With a sufficient flow rate, the coolant floods the cavity and then the radial velocity of the flow becomes predominant causing the bi-dimensional core flow to vanish.

Finally, the rim seals are characterized by an egress and ingress of flow from the cavity to the mainstream. This fluid motion is responsible for altering the mainstream properties in the sections upstream and downstream of the vane. The interaction between the rim seal flow and the mainstream lead to an intensification of the secondary flow structures and a reduction of the incidence angle on the subsequent blade rows. Overall, these effects constituted a remarkable source of losses for the mainstream developing throughout the stage, hence for the entire engine, that need to be deeply investigated.

2.2 Rotor-Stator Systems

The first step for understanding the flow behavior in real turbine interstage cavities, is to give an insight on the flows that occur in simplified geometries such as rotating free discs and, in particular, in rotor-stator systems [1]. The Navier-Stokes equations are well suited for describing the Newtonian flow on a rotating disk system as the one shown in figure 2.3. Governing geometrical parameters are constituted by the outer disk radius b, the distance s between the rotor and the stator and the clearance s_c of the external shroud. The cylindrical coordinates in the absolute frame of reference (r, ϕ, z) are adopted. The disk rotates with angular velocity Ω around the z-axis in the direction of positive ϕ. The plane located at $z = 0$ corresponds to the rotor and the plane $z = s$ to the stator surface. For the present discussion the flow is assumed to be steady axisymmetric, so that $\partial q/\partial t = \partial q/\partial \Phi = 0$ for all dependent variable q, and incompressible. In addition, dynamic viscosity μ and kinematic viscosity ν are assumed constant.

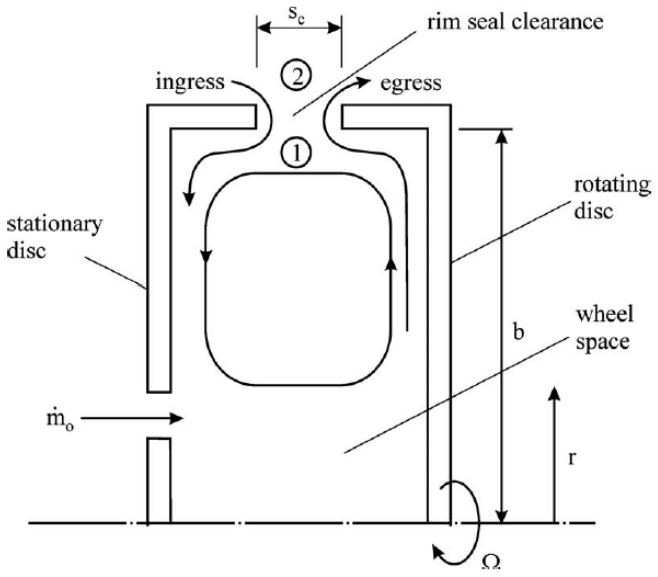

Figure 2.3 Schematic representation of a rotor-stator system

2.2.1 Equations of motion

The Navier-Stokes equations can be written in component form as follows:

$$\frac{\partial v_r}{\partial r} + \frac{v_r}{r} + \frac{\partial v_z}{\partial z} = 0 \tag{2.01}$$

$$v_r \frac{\partial v_r}{\partial r} + v_z \frac{\partial v_r}{\partial z} - \frac{v_\Phi^2}{r} = -\frac{1}{\rho}\frac{\partial p}{\partial r} + \nu\left(\nabla^2 v_r - \frac{v_r}{r^2}\right) \tag{2.02}$$

$$v_r \frac{\partial v_\Phi}{\partial r} + v_z \frac{\partial v_\Phi}{\partial z} - \frac{v_r v_z}{r} = \nu\left(\nabla^2 v_\Phi - \frac{v_\Phi}{r^2}\right) \tag{2.03}$$

$$v_r \frac{\partial v_z}{\partial r} + v_z \frac{\partial v_z}{\partial z} = -\frac{1}{\rho}\frac{\partial p}{\partial z} + \nu\nabla^2 v_z \tag{2.04}$$

where:

$$\nabla^2 = \frac{\partial^2}{\partial r^2} + \frac{1}{r}\frac{\partial}{\partial r} + \frac{\partial^2}{\partial z^2} \tag{2.05}$$

In the case of laminar fluid, these equations are valid as they stand but in the case of turbulent flow, the hypothesis of steady flow is no longer valid. Following the Reynolds decomposition, the velocity and the pressure are split into an averaged component and a fluctuating component whose average (over a time t_0 small compared to Ω^{-1}) is zero. The variables p and v in equations (2.01) to (2.04) are replaced by $\bar{v} + v'$ and $\bar{p} + p'$ then the equations are averaged (again over a suitable time t_0) and they become:

$$\frac{\partial \bar{v}_r}{\partial r} + \frac{\bar{v}_r}{r} + \frac{\partial \bar{v}_z}{\partial z} = 0 \tag{2.06}$$

$$\bar{v}_r \frac{\partial \bar{v}_r}{\partial r} + v_z \frac{\partial \bar{v}_r}{\partial z} - \frac{\bar{v}_\Phi^2}{r} = -\frac{1}{\rho}\frac{\partial \bar{p}}{\partial r} + \nu\left(\nabla^2 \bar{v}_r - \frac{\bar{v}_r}{r^2}\right) - \frac{1}{r}\frac{\partial}{\partial r}\left(r\overline{v'^2_r}\right) - \frac{\partial}{\partial z}\left(\overline{v'_r v'_z}\right) + \frac{\overline{v'^2_\Phi}}{r} \tag{2.07}$$

$$\bar{v}_r \frac{\partial \bar{v}_\Phi}{\partial r} + v_z \frac{\partial \bar{v}_\Phi}{\partial z} - \frac{\bar{v}_r \bar{v}_\Phi}{r} = \nu \left(\nabla^2 \bar{v}_\Phi - \frac{\bar{v}_\Phi}{r^2} \right) - \frac{1}{r} \frac{\partial}{\partial r} \left(r \overline{v'_\Phi v'_r} \right) - \frac{\partial}{\partial z} \left(\overline{v'_\Phi v'_z} \right) + \frac{\overline{v'_r v'_\Phi}}{r} \tag{2.08}$$

$$\bar{v}_r \frac{\partial \bar{v}_z}{\partial r} + v_z \frac{\partial \bar{v}_z}{\partial z} = -\frac{1}{\rho} \frac{\partial \bar{p}}{\partial z} + \nu \nabla^2 \bar{v}_z - \frac{1}{r} \frac{\partial}{\partial r} \left(r \overline{v'_r v'_z} \right) - \frac{\partial}{\partial z} \left(\overline{v'^2_z} \right) \tag{2.09}$$

2.2.2 Inviscid equations

For a single disc in a fluid of large extent as well as for a rotor-stator system where the distance between the disks is sufficiently large, viscous and turbulent effects become negligible except for the near wall regions. In the case of rotor-stator systems the inviscid flow that establishes between the two boundary layers, took the name of "core flow" and it has been already mentioned in the section 2.1 of this chapter. It is therefore interesting to consider the solutions of the equations of motion when the viscous terms are negligible: if we use the subscript ∞ referred to a flow far enough from the discs, then the equations (2.02) to (2.04) become:

$$v_{r,\infty} \frac{\partial v_{r,\infty}}{\partial r} + v_{z,\infty} \frac{\partial v_{r,\infty}}{\partial z} - \frac{v^2_{\Phi,\infty}}{r} = -\frac{1}{\rho} \frac{\partial p_\infty}{\partial r} \tag{2.10}$$

$$v_{r,\infty} \frac{\partial v_{\Phi,\infty}}{\partial r} + v_{z,\infty} \frac{\partial v_{\Phi,\infty}}{\partial z} - \frac{v_{r,\infty} v_{\Phi,\infty}}{r} = 0 \tag{2.11}$$

$$v_{r,\infty} \frac{\partial v_{z,\infty}}{\partial r} + v_{z,\infty} \frac{\partial v_{z,\infty}}{\partial z} = -\frac{1}{\rho} \frac{\partial p_\infty}{\partial z} \tag{2.12}$$

In practice, the radial component of the velocity is zero throughout much of the core. Then, if we impose $v_{r,\infty} = 0$ into equation (2.01) and equations (2.10) to (2.12), the following important results are obtained:

$$v_{r,\infty} = 0, \qquad \frac{\partial v_{\Phi,\infty}}{\partial z} = 0, \qquad \frac{\partial v_{z,\infty}}{\partial z} = 0, \quad \frac{v^2_{\Phi,\infty}}{r} = \frac{1}{\rho} \frac{\partial p_\infty}{\partial r} \tag{2.13}$$

2.2.3 Boundary layer equations

In the proximity of the solid walls, as well as in the case of small distance between the disks in rotor stator systems, viscous effects are not negligible and the following approximations can be considered:

1. the axial component of the velocity v_z is much smaller in magnitude than the other two components;
2. the rate of change of the velocity component in the z-direction is much greater than its rate in the radial or tangential direction;
3. the pressure depends only on the distance from the axis of rotation.

Introducing these approximations into the set of equations of motion, the shear stress tensor for turbulent flow reduces to a vector $\tau = (\tau_r, \tau_\phi, \tau_z)$. For brevity, the approximated boundary layer equations for both laminar and turbulent flows are collapsed into a single set by omitting the overbars on the averaged velocity components, pressure and temperature. For laminar flows, the fluctuating terms in the shear stress components τ are identically zero. Hence, we obtain:

$$\frac{\partial v_r}{\partial r} + \frac{v_r}{r} + \frac{\partial v_z}{\partial z} = 0 \tag{2.14}$$

$$v_r \frac{\partial v_r}{\partial r} + v_z \frac{\partial v_r}{\partial z} - \frac{v_\Phi^2}{r} = -\frac{1}{\rho}\frac{\partial p}{\partial r} + \frac{1}{\rho}\frac{\partial \tau_r}{\partial z} \tag{2.15}$$

$$v_r \frac{\partial v_\Phi}{\partial r} + v_z \frac{\partial v_\Phi}{\partial z} - \frac{v_r v_z}{r} = \frac{1}{\rho}\frac{\partial \tau_\Phi}{\partial z} \tag{2.16}$$

$$0 = -\frac{\partial p}{\partial z} \tag{2.17}$$

where:

$$\tau_r = \mu \frac{\partial v_r}{\partial z} - \rho \overline{v_r' v_z'} \tag{2.18}$$

$$\tau_\Phi = \mu \frac{\partial v_\Phi}{\partial z} - \rho \overline{v_\Phi' v_z'} \tag{2.19}$$

It is worth noting that, similarly to what happens for the boundary layer over a flat plate, the pressure in each radial position is independent of the normal-to-the-wall coordinate z. It means that in the case of rotor-stator systems the pressure on the rotor and on stator walls is equal to the one in the inviscid core.

2.2.4 Free-disc pumping effect

Before introducing the flow evolving in a rotor-stator system it is useful to analyze an important aspect regarding the flow due to a single disk rotating in a free space. We consider only the case of a disc rotating in a quiescent flow (free-disk case). Other three "basis" cases, for which an analytical solution exists, can be identified depending on the relative rotational speed between the disk and the outer flow [1]. The centrifugal forces created by the rotation cause a radial movement of fluid within the boundary layer. Since the radial component of velocity is zero in the free-stream and on the disk, it means that a portion of external fluid is entrained axially into the boundary layer and pumped radially, as shown in figure 2.4.

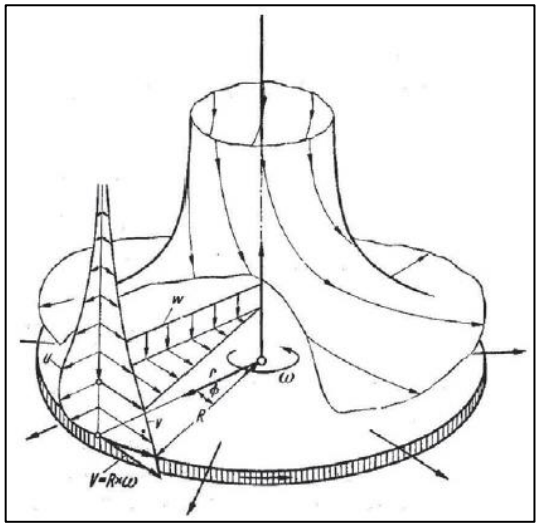

Figure 2.4 Quiescent flow evolving on a free-disc

To compute analytically the amount of pumped flow rate we must distinguish between the two boundary layer flow regimes. The flow inside the boundary-layer may be either laminar or turbulent depending on the value of the local rotational Reynolds number $x^2 Re_\phi = \Omega r^2/\nu$ where $x = r/b$ is the non-dimensional radial coordinate (b is the outer disk radius). Generally, the flow in the proximity of the axes of rotation is laminar regardless of the rotational speed but transition could occur at low radius whenever the rotational speed is high. The experimental results of *Gregory et al. (1955)* [2] (also reported in [1]) indicate that transition

occurs for x^2Re_ϕ around 2x10^5 and the flow is completely turbulent for x^2Re_ϕ between 2.7x10^5 and 2.99x10^5. The boundary conditions for the velocity components for both turbulent and laminar flows, valid in the region of $0 < r < b$, are:

$$v_r = 0, \qquad v_\phi = \Omega r, \qquad v_z = 0 \tag{2.20}$$

at $z = 0$ and:

$$v_r \to 0, \qquad v_\phi \to 0 \tag{2.21}$$

for $z \to \infty$. The value of v_z far from the disc provides the amount of fluid necessary to feed the pumping effect. The mass flow rate that is entrained by the boundary layer on one side of the disk is equal to the axial flow rate that moves towards the boundary layer from outside, so that $\dot{m}_{ent} = 2\pi\rho \int_0^r r v_z|_{z\to\infty}\, dr$. Major details about the momentum integral equations and their solution techniques are given in the first volume of *Owen and Rogers (1989)* [1].

For laminar flow (solved first by Von Karman in 1921) it results that the boundary layer thickness δ, that is evaluated as the distance from the disc at which $v_\phi = 0.01\Omega r$, is independent of the radial coordinate but only of the rotational speed, so that $\delta = K(\nu/\Omega)^{0.5}$, where *K* is a constant (usually *K*=5.5). The resulting non-dimensional local mass flow rate on the disk is:

$$C_{w,FD} = \frac{\dot{m}_{ent}}{\mu r} = 2.779(x^2Re_\phi)^2 \tag{2.22}$$

On the other hand, the solution of the boundary layer equations for turbulent flow gives the following relation for the local non-dimensional mass flow rate:

$$C_{w,FD} = \frac{\dot{m}_{ent}}{\mu r} = 0.219(x^2Re_\phi)^{0.8} \tag{2.23}$$

Finally, *Chew (1998)* [3] derived the following relationship that allows evaluating the non-dimensional mass flow rate entrained on a partial disk $C_{w,ent}$ with inner radius a to the free disk entrainment value $C_{w,FD}$:

$$\frac{C_{w,ent}}{C_{w,FD}} = 1 - \left(\frac{a}{b}\right)^5 \tag{2.24}$$

2.2.5 Flow regimes in rotor-stator systems

For an enclosed rotor-stator system (thus with rim clearance $s_c = 0$), *Daily and Nece (1960)* [4] classified four regimes of flow developing between the disks depending on the relative magnitude between the gap ratio $G = s/b$ and the rotational Reynolds number Re_ϕ. The boundaries of the four regimes are indicated in the plot of figure 2.5 and the main features of each one are summarized in table 2.1. The flow may be either laminar or turbulent depending on Re_ϕ for each value of the gap ratio G. When G is small (regimes I and III) a *Couette-type* flow is expected in which the viscous region fills the whole space between the disks. This regime was first described by Stewartson in 1958 [5] and the expected velocity profiles in the wheel-space are plotted in figure 2.6(a). Particularly, the tangential velocity decreases monotonically from the value on the rotating disc to zero on the stator while the radial velocity keeps positive for the entire distance s. On the contrary, if the clearance is large compared to the radius, a *Batchelor-type* flow occurs (regimes II and IV). The boundary layers that generate on the disc surfaces are separated by an inviscid core flow that rotates with angular velocity ω. The ratio $v_\phi/\Omega r$ in the core region for $G = 0.1$ and $Re_\phi = 5.5 \times 10^4$ (i.e. for laminar flow) has been measured equal to 0.4 [6]. The velocity profiles expected for these flow regimes are plotted in figure 2.6(b). It is possible to observe that the radial component of the velocity is almost null in the middle. On the other hand, the axial velocity profiles for the *Stewartson* and *Batchelor-type* flows are similar. The presence of superposed flows injected into the cavity or ejected, affects the boundaries but the same flow regions can be observed. In rotor-stator cavities of interest within gas turbine, flow is often of regime IV.

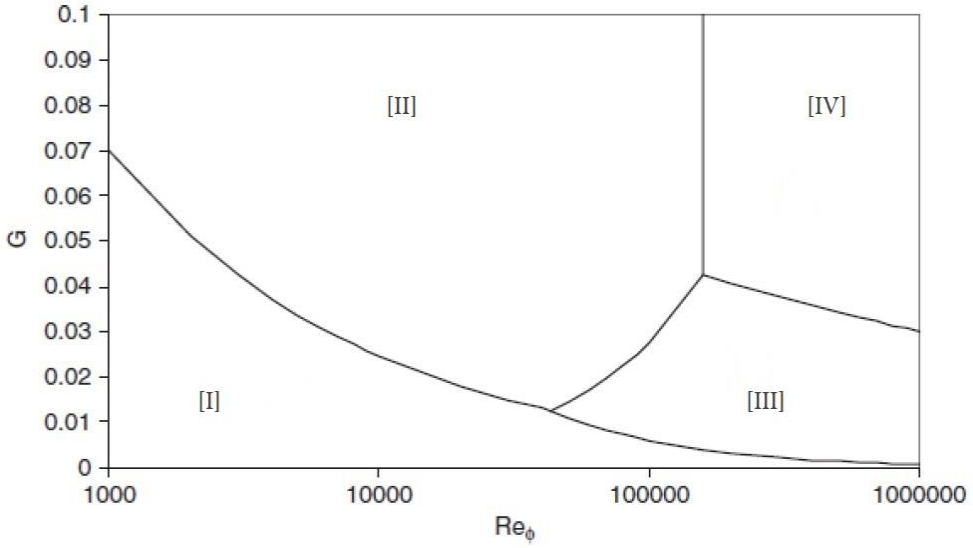

Figure 2.5 Flow regime in the wheelspace of enclosed rotor-stator systems

Regime	Clearance	Flow
[I]	Small	Laminar
[II]	Large	Laminar
[III]	Small	Turbulent
[IV]	Large	Turbulent

Table 2.1 Main features of flow regimes

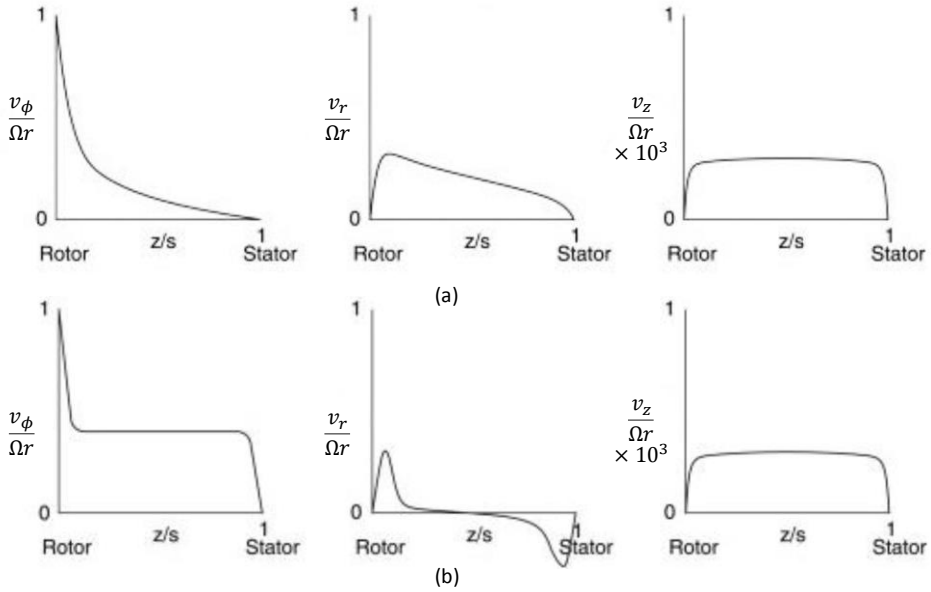

Figure 2.6 Velocity profiles for Stewartson-type flow (a) and Batchelor-type flow (b) in enclosed rotor-stator systems

2.2.6 Sealing rotor-stator systems

For rotor-stator systems with open rim seal clearance like the one of figure 2.3, we can identify two different mechanisms that cause the ingress of external air flow into the cavity. First, if we consider a quiescent environment with constant pressure, the presence of a rotating fluid in the wheelspace (the core flow) creates a radial adverse pressure gradient $\partial p/\partial r > 0$. Consequently, the pressure inside the cavity can drop below the one in the outer space. Therefore, the disc pumping effect causes a radial outflow of fluid in correspondence of the rotor disk, while the low pressure in the wheelspace causes ingress of external fluid through the rim seal into the cavity. This mechanism is referred in the literature as *Rotational Induced Ingress* (RI) [7] [8]. In gas-turbines there also exists another mechanism named *Externally*

Induced Ingress (EI) that is related to the presence of an external air flow and a circumferential pressure gradient due to the potential field of the blades [9] [10]. The ingress and egress occurs in the part of the seal clearance where the pressure in the outer annulus is higher and lower than the one in the cavity, respectively as shown in figure 2.7.

In LPT cavities such that of figure 2.1, the ingress of hot gas from the main annulus is also governed by the labyrinth seal demand driven by the pressure drop across the vane. Cooling air is supplied into the cavity with the double aim of pressure sealing the cavity in order to avoid ingress of hot gas, and directly removing heat from the disks in order to prevent overheating.

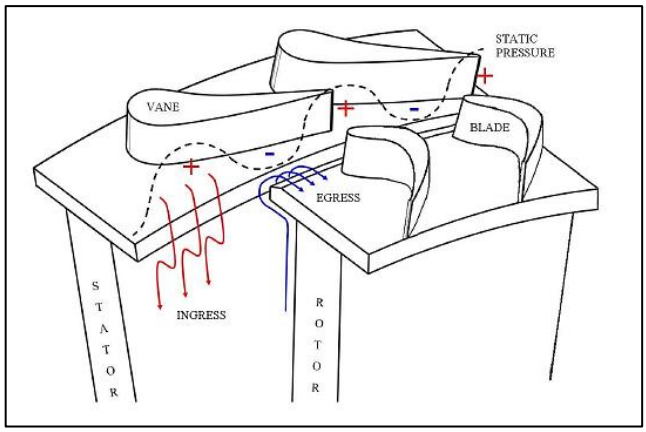

Figure 2.7 ***Externally Induced Ingress*** **mechanism**

The presence of a radial inflow from external sources (i.e. due to the coolant) strongly alters the cavity flow structures. Particularly, in regime IV there is a tendency to cause transition from *Batchelor-type* to a *Stewartson-type* flow depending on the amount of the coolant flow rate $\dot{m}_c$ [11] [12]. To this end, the flow regime can be evaluated using the non-dimensional coolant flow rate $C_{w,c} = \dot{m}_c/\mu R_c$, where R_c is the radius at which the coolant flow is delivered. As far as the coolant flow rate is lower than the entrainment capacity of the disk such that $C_{w,c} < C_{w,0}$ (see equations 2.22 to 2.24), then the coolant remains confined into the rotor boundary layer and the flow remains characterized by a rotating core flow. However, as more coolant flow rate is delivered into the cavity, the viscously dominated near wall region enlarges and the rotating core flow diminishes. When $C_{w,c} > C_{w,0}$, the radially forced flow prevails and the core flow could result almost entirely suppressed [13].

Several studies have been made with the purpose of evaluating the minimum coolant flow rate that prevents the ingress of mainstream hot gas $C_{w,min}$. *Bayley and Owen (1970)* [14] carried out experiments on a rotor-stator system in a quiescent environment for Re_ϕ<4x10^6

and different gap ratios. The minim value of $C_{w,min}$ was determined as the one that provides a zero pressure difference through the rim seal. No significant effects of the gap ratio were found and the results were correlated by:

$$C_{w,min} = 0.61 G_c Re_\phi \tag{2.25}$$

where G_c=s_c/b is the shroud clearance ratio. In the case of quasi-axisymmetric external flow, it has been found that the value of $C_{w,min}$ depends on the ratio between the rotational Reynolds number Re_ϕ and the external-flow Reynolds number $Re_w = Wb/\nu$, where W is the axial velocity of the external flow. Results obtained by *Phadke and Owen (1988)* [15] for a geometry with axial rim clearance, are shown in figure 2.8.

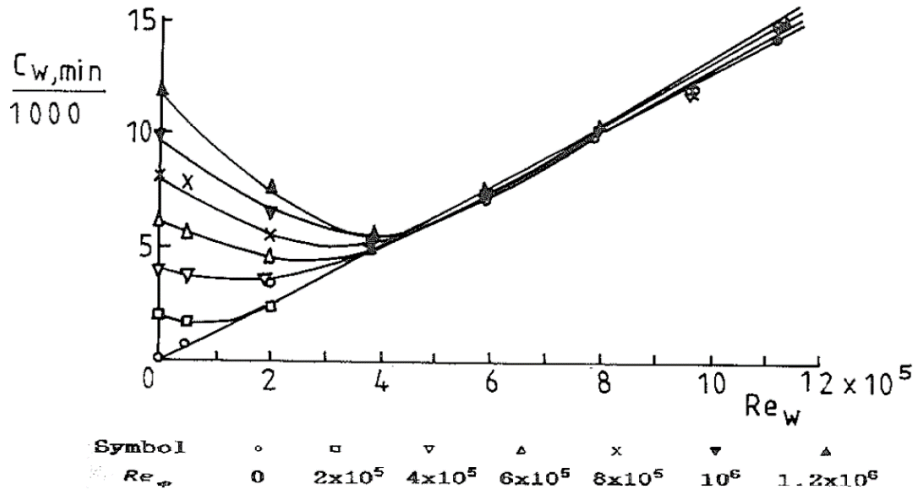

Figure 2.8 Effect of Re_ϕ and Re_V on $C_{w,min}$ for an axial rim clearance [15]

It can be observed that for $Re_W = 0$, $C_{w,min}$ increases linearly with Re_ϕ as predicted by the correlation of *Bayley and Owen (1970)*. For $Re_w \geq 0.6 \times 10^6$ there is an external-flow-dominated regime in which $C_{w,min}$ becomes independent of Re_ϕ and increases as Re_W increases. In the middle, $C_{w,min}$ may either increase or decrease depending on the ratio of Re_W and Re_ϕ.

In the externally dominated flow regime, the EI ingress prevails and it is useful to introduce a non-dimensional pressure asymmetry defined as:

$$C_{p,max} = \frac{\Delta p_{max}}{0.5 \rho W^2} \tag{2.26}$$

where Δp_{max} is the maximum difference that can be observed between the external and internal flow along the circumferential direction. *Phadke and Owen (1988)* [9] derived a simplified formulation for $C_{w,min}$ for the EI ingress:

$$C_{w,min} = 2\pi K G_c P_{max}^{0.5} \tag{2.27}$$

where $K = (2A)^{0.5} C_D$ is a constant related to the area of the rim seal clearance A and its discharge coefficient C_D while $P_{max} = 0.5 C_{p,max} Re_W$ is a pressure coefficient related to the external flow Reynolds number and the non-dimensional pressure asymmetry. Figure 2.9 provides a comparison between several data measured for different rim seal geometries and the correlation of equation (2.27) for which K is constant and equal to 0.6.

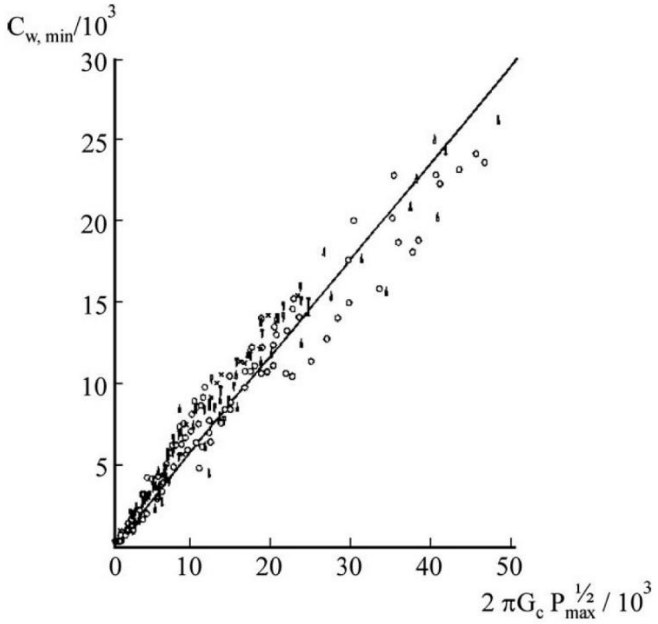

Figure 2.9 Comparison between measured $C_{w,min}$ and correlation (2.27) [9]

2.3 Labyrinth Seals

Contactless labyrinth seals are the most important and widely used elements in turbomachinery for reducing leakage flow from high to low pressure regions through the gaps between rotating and stationary parts [16]. Major advantages of this technology include structural simplicity, reliability and the capacity to operate in a wide range of operating conditions in terms of high temperature and high pressure. If we consider a generic labyrinth seal geometry as in figure 2.10, the energy dissipation is achieved by a combination of constrictions and expansions. When the air flow passes through the constriction between the tooth and the upper surface ("land"), a part of the pressure energy is converted into kinetic energy which is subsequently dissipated through turbulence and viscosity in the cavity that follows. This mechanism increases the flow resistance and reduces the leakage flow rate [17].

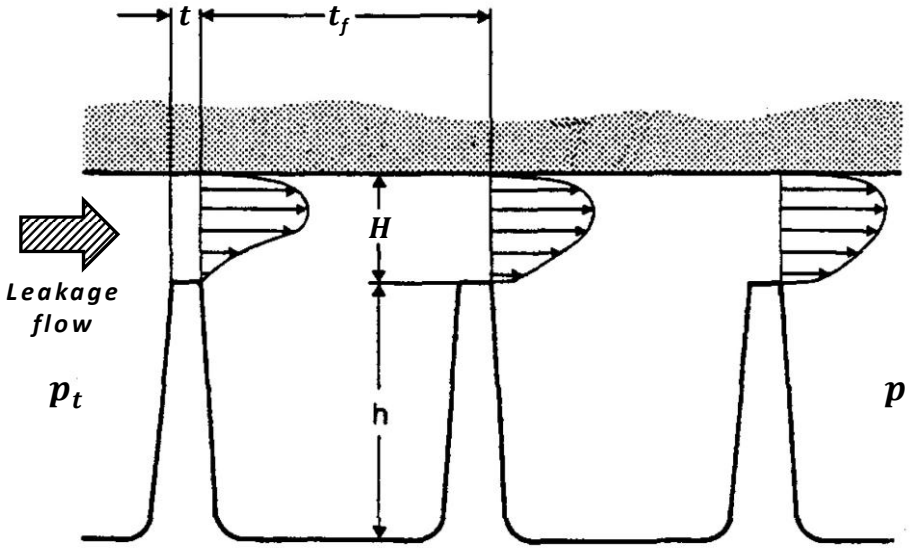

Figure 2.10 Straight-through labyrinth seal geometry

Two major design configurations can be found in gas-turbines depending on the direction that the leakage flow follows from the inlet to the outlet sections:

- **Straight-through seal**: inlet and outlet sections are located at the same radial position so that the mean leakage flow direction is parallel to the axis of rotation;
- **Stepped seal**: inlet and outlet sections are located at different radius. The seal is *divergent* if the leakage flow moves from the inlet to the outlet section towards higher radius, and *convergent* vice versa;

other geometrical parameters that characterize the labyrinth seal design are the number of tooth N, the fin tip thickness t, the clearance height H and the local radius of the passage area.

The sealing performances of labyrinth seals are characterized through the discharge coefficient C_D defined in *Witting et al. (1983)* [18] as the ratio between the actual leakage mass flow rate ($\dot{m}_l$) and the flow rate of an isentropic fluid ($\dot{m}_{id}$) that flow through an ideal nozzle with the same pressure ratio and cross-sectional area of the labyrinth seal:

$$C_D = \frac{\dot{m}_l}{\dot{m}_{id}} \tag{2.28}$$

$$\dot{m}_{id} = \frac{p_t A}{\sqrt{T_t}} \sqrt{\frac{2k}{R_{gas}(k-1)} \left[1 - \left(\frac{1}{\beta}\right)^{\frac{k-1}{k}} \right]} \left(\frac{1}{\beta}\right)^{\frac{1}{k}} \tag{2.29}$$

where A is the throat area, $\beta = p_t/p$ is the expansion ratio across the seal, T_t is the inlet total temperature, while k and R_{gas} denote the type of fluid. Thus, the discharge behavior of the seal is strongly affected by geometrical parameters and the inlet and outlet conditions of the fluid.

For LPT interstage labyrinth seals it is extremely important to know the amount of flow demanded by the seal in each operating engine condition. As stated before in this chapter, the leakage flow influences the amount of coolant necessary to prevent the ingress. So far, the design of labyrinth seals is based on a large extent of experimental and CFD data available in open literature [19]. A list of correlations for calculating the seal leakage of different type of labyrinth seals is presented in *Zimmermann and Wolff (1998)* [20]. Most of these data concern stationary seals for which a well established set of depending non-dimensional numbers are known to affect the overall seal discharge coefficient. The rotation of the disk as well as the presence of an inlet pre-swirl of the flow have been found to have a deep impact on the discharge coefficient and a new set of non-dimensional parameter is needed. A brief review of all these concepts is given in the following.

Nevertheless, major obstacle for using these data for the design of new optimized seal geometries is represented by the fact that the boundary conditions of the flow within the cavity are unknown *a priori*. These strongly depend on how the flow ingested from the main annulus interacts with the flow patterns inside the cavity and the coolant flow (see figure 2.1). In open literature, there is a lack of work concerning the evaluation of the leakage flow rate and the discharge coefficient for real cavity geometries operating under realistic engine conditions.

2.3.1 Stationary seals: effect of Reynolds number and expansion ratio

The discharge coefficient for a stationary seal ($C_{D,0}$) is mainly function of the Reynolds number, the pressure drop, the flow turbulence intensity and the scale geometry [16]:

$$C_{D,0} = \mathcal{F}(Re_z, \beta, geometric\ scale, k, Tu) \tag{2.30}$$

$$Re_z = \frac{2\dot{m}_l}{\mu B} \tag{2.31}$$

where the axial Reynolds number Re_z is defined using the hydraulic diameter, which for this geometry, is two times the seal clearance *H*, being the parameter *B* the "seal width parameter" defined as $B = A/H$. In order to show the interdependence of each non dimensional number, the results of *Willenborg et al. (2001)* [16] are presented in figure 2.11 and figure 2.12. In this study, stepped stationary labyrinth seals with different geometrical parameters were considered. The Reynolds number and the pressure ratio were varied independently. Seal geometries differ for the ratio between the seal width and the fin thickness H/t, and for the ratio between the fin radius and the fin thickness R/t.

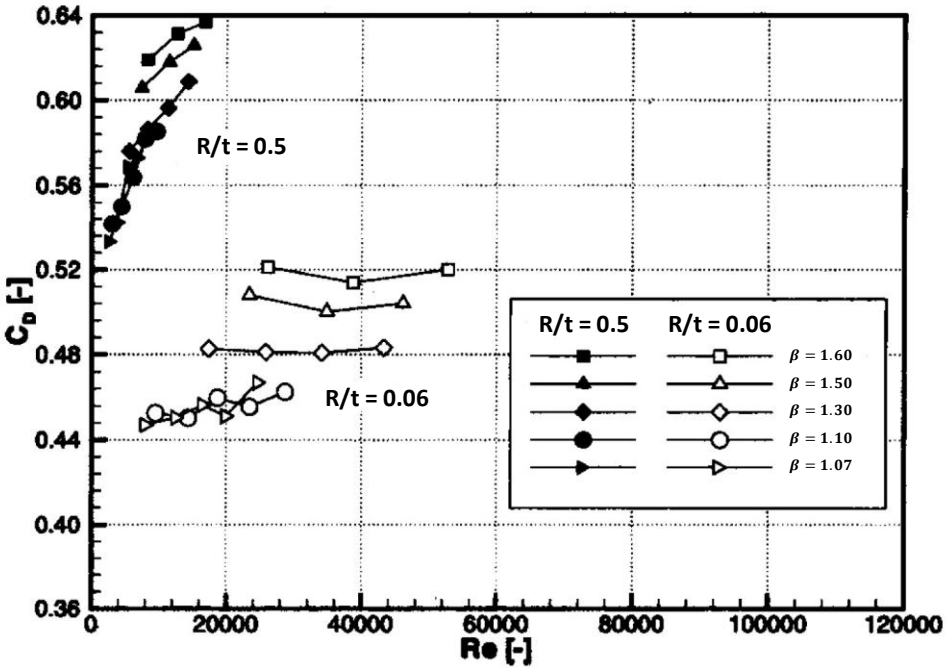

Figure 2.11 Discharge coefficient H/t=0.909 [16]

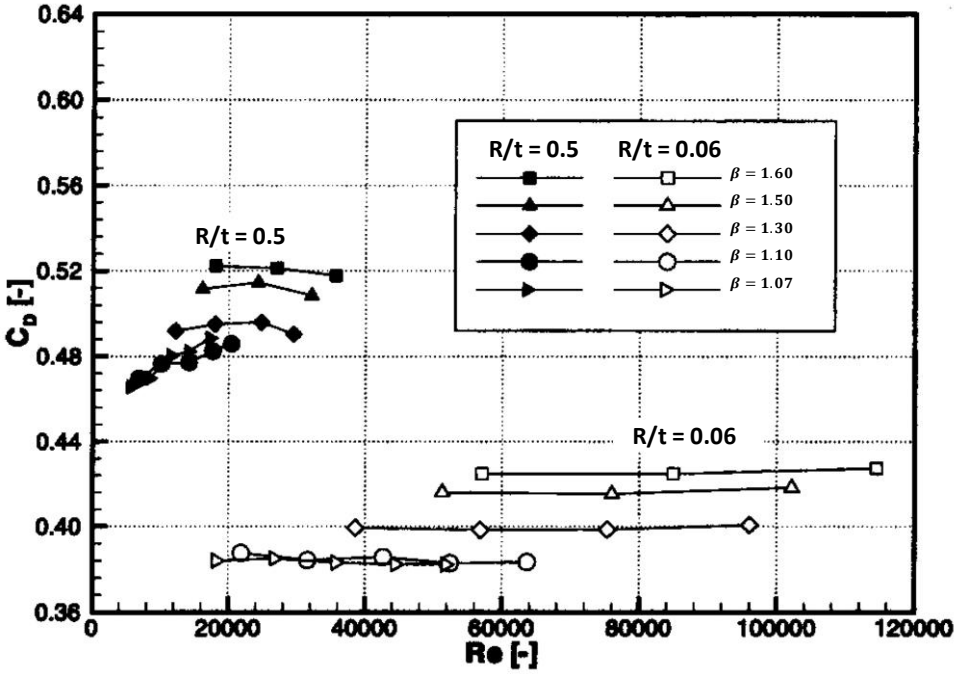

Figure 2.12 Discharge coefficient, H/t=2.424 [16]

In the case of small H (figure 2.11) the discharge coefficient increases considerably with the Reynolds number as long as $Re_z < 20000$ (black points). Increasing the seal width (figure 2.12), the discharge coefficient reduces. In this figure, in the region of low Reynolds numbers (black points), an increase of the C_D with the Re_z occurs only for small pressure ratios while a fairly uniform distribution develops for higher values of β. For large Reynolds numbers (white points in figures), the discharge coefficient of a given seal configuration becomes only dependent on the pressure ratio.

2.3.2 Effect of rotation

In literature, a generic reduction of the leakage flow rate for a datum seal geometry is observed with rotation. *Denecke et al. (2004)* [21] identified three main related effects of rotation on the leakage:

- *Effect of clearance change:* the clearance reduces with rotation due to the centrifugal forces acting on the disc and the thermal expansion. The main effect is to reduce the passage area A which is already considered into the definition of the discharge coefficient. A second order effect is the influence of the change of the fin width to clearance ratio and cause a contraction of the flow streamtubes in the throat. These considerations indicate the necessity to keep monitoring the seal clearance during experiments;
- *Effect of increased friction:* increasing the circumferential velocities, the turbulence level in the axial direction also increases. Higher *Tu* values increase the wall shear stress and lead to an additional pressure loss. The turbulence intensity in non-rotating seals is of the order of 6% to 10% [22]. Data from *Blair (1983)* [23] show that in a turbulent boundary layer over a flat plate an increasing turbulence from 4% to 8% lead to a 15% rise of the friction coefficient;
- *Effect of pumping:* this effect is observed in stepped labyrinth seals where the centrifugal forces varies due to change of the radial position of the fluid from inlet to the outlet. Then, in convergent seals the centrifugal forces act against the flow passage, that is from high to low radius, hence reducing the leakage. On the contrary, in divergent seals they act with the main flow thus increasing the leakage. The pumping effect is observed to be negligible at high pressure ratios, however for small pressure ratio it becomes relevant causing a change of the total pressure drop up to ±75%.

Figure 2.13 shows the experimental data of *Waschka et al. (1992)* [24] that measured the discharge coefficient of a six fins straight through labyrinth seals with $R/t = 50$, for different rotational speed and Reynolds number. The labyrinth seal radius R was used as characteristic length in the definition of the axial Reynolds number instead of the seal width B. Measurements have been carried out for different nominal seal clearance ($H/t = 0.2$ for the plot on the left and $H/t = 0.52$ for the right plot) and by monitoring the running value during experiments.

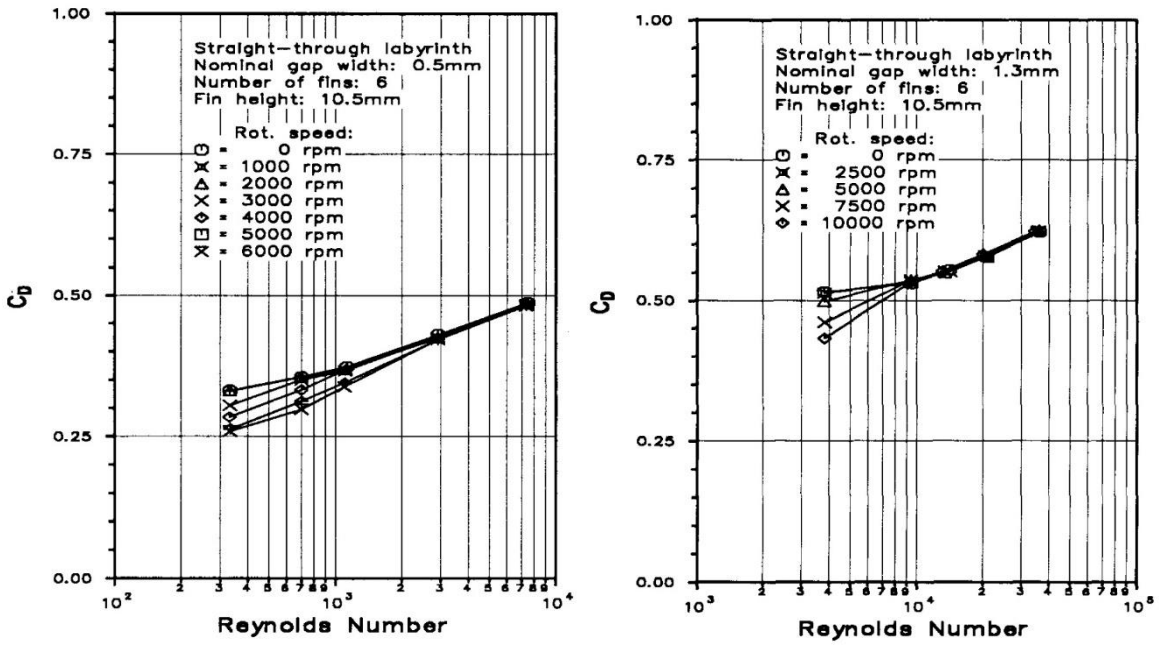

Figure 2.13 Effect of rotation and axial Reynolds number on the discharge coefficient for different nominal seal clearance [24]

Results show that the discharge coefficient keeps increasing with the Reynolds number for both seal clearances. For low Reynolds numbers, depending on the seal clearance, the rotation reduces the discharge coefficient with respect to the stationary case. The influence of rotation vanishes at high Reynolds number but the threshold level appears to depend on the clearance value. To this end, *Denecke et al. (2004)* [21] reported a correlation for determining the ratio between the discharge coefficient of a rotating seal with respect to its stationary value depending on the ratio between the axial velocity of the leakage flow and the circumferential velocity of the rotor. Then:

$$\frac{C_D}{C_{D,0}} = 1 \tag{2.32}$$

for $\frac{\Omega R}{v_z} \cdot K < 1$ and:

$$\frac{C_D}{C_{D,0}} = 0.999 - 0.071\text{x} + 0.1457x^2 - 0.494x^3 + 0.1714x^4 \tag{2.33}$$

for $\frac{\Omega R}{v_z} \cdot K \geq 1$, where $x = \log\left(\frac{\Omega R}{v_z} K\right)$. The constant parameter K has to be adapted for introducing the seal type:

- Straight- through K=1.17
- Convergent stepped K=1.06
- Divergent stepped K=1.08

2.3.3 Effect of pre-swirl

The seal inlet velocity in real engines consists of a large circumferential component of about 20% to 80% of the rotor circumferential speed. Thus, we can introduce a *Swirl factor* of the fluid defined as follows:

$$S_w = \frac{v_\phi}{\Omega R} \tag{2.34}$$

where v_ϕ is the tangential velocity of the fluid and ΩR is the tangential velocity of the rotor at the radius R. In labyrinth seals, the momentum of the circumferential velocity at the inlet does not contribute to the leakage as the momentum of the axial velocity does [21]. Therefore, an increase of the inlet swirl leads to a reduction of the effective pressure ratio of the fluid across the seal. Thus, it is proposed to introduce an *effective pressure ratio* in the determination of the discharge coefficient (equations 2.28 and 2.29), where the dynamic pressure of the inlet swirl is subtracted from the inlet total pressure according to equations (2.35) and (2.36):

$$\beta_{eff} = \frac{p_t - \Delta p_{preswirl}}{p_2} \tag{2.35}$$

$$\Delta p_{preswirl} = p_t - \frac{p_t}{\left(1 + \frac{k-1}{2} Ma_\phi^2\right)^{\frac{k-1}{k}}} \tag{2.36}$$

where $Ma_\phi = v_\phi / \sqrt{k R_{gas} T}$ is the circumferential Mach number. *Denecke et al. (2004)* considered labyrinth seals with different inlet flow swirls. The discharge coefficients calculated using the effective pressure ratio showed a less reduction with respect to the no-preswirl case. This happens also considering data from non-rotating seals [21]. The remaining deviation from the no-preswirl case is attributed to the axial development of the circumferential velocity through the seal.

2.3.4 Swirl development in rotating seals

Another important aspect concerning rotating seals in turbomachinery is represented by the axial development of the swirl parameter [25]. For instance, the interstage exit swirl $S_{w,out}$ locally changes the incidence angle of downstream blades and thereby influences the stage losses [26]. The fluid across the seal is accelerated by the wall friction on the rotor and decelerated by the stator. Thus, if we consider an ideal infinite seal with incompressible flow, the tangential velocity reaches a constant value regardless of the inlet conditions. The equilibrium swirl was derived analytically in *Denecke et al. (2008)* [26]. It depends only on the ratio between the surface area of the stator and the rotor. Typical labyrinth seals with teeth on the rotor and the smooth stator have an area ratio of about 0.7 which leads to an equilibrium swirl of about $S_{w,eq}$=0.55.

Figure 2.14 shows the result of the numerical analysis on a four-fins divergent stepped seal [27]. The plot shows the strong influence of the inlet preswirl on the outlet swirl value. All the curves tend to an asymptotic value represented by the equilibrium swirl condition. Naturally, if the inlet swirl is higher than the equilibrium the flow is decelerated across the seal, as in the case of $S_{w,in} = 0.8$.

The effective pressure ratio has only marginal effects. On the contrary, the higher the ratio $\Omega R/v_z$ the more the outlet swirl approach the equilibrium condition at the exit.

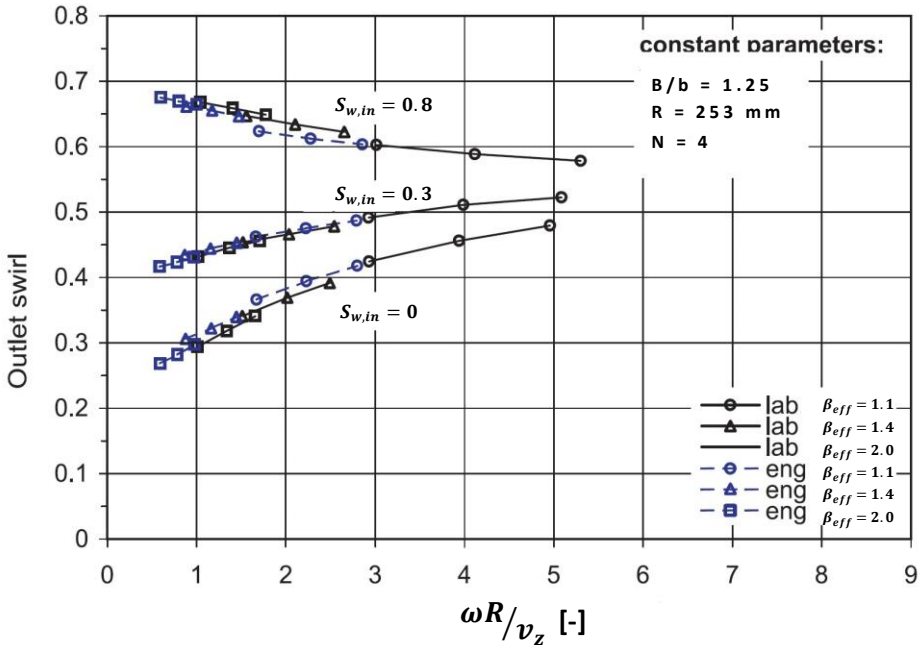

Figure 2.14 Outlet swirl of the flow as function of the inlet swirl, pressure ratio and $\omega R/v_z$ [27]

2.3.5 Dimensional analysis and scaling of rotating seals

In *Denecke et al. (2005)* [27], a dimensional analysis was presented to find a set of non-dimensional parameters capable of describing the discharge behavior and swirl development of the flow in rotating seals. The result of the dimensional analysis was further validated through a comprehensive numerical study. As conclusions, the following dimensionless numbers were found to uniquely define the discharge behavior and exit-swirl:

$$\frac{C_D}{S_{w,out}} = \mathcal{G}\left(Re_z, \beta_{eff}, S_{w,in}, \frac{\Omega R}{v_z}, geometry, k\right) \tag{2.37}$$

where all the dimensionless numbers have been already introduced and analyzed in this section. It is worth noting, if compared to the relation for stationary seal, that the inlet turbulence intensity was cancelled as it is assumed to have a minor impact on the unknowns because the overall turbulence level is dominated by the contraction across the first fin and the mixing of the wall jet in the chamber. In addition, a more general term "geometry" compares in the relation as no predominant geometrical parameter was identified.

2.4 Influence of the Coolant

As mentioned early in this chapter, a proper amount of cold air is bled from the compressor and sent directly into the interstage cavities to reduce the wall temperature of the disks, thus preventing overheating, as well as to reduce, to some degree, the ingestion of mainstream hot gas into the wheelspace. These cooling flows are bled from the compressor stages and directly reduce the overall engine efficiency as they represent around 20% of the total main gas path flow rate. These performance penalties manifest themselves in two ways, i.e., having a direct impact on the thermodynamic cycle performance, resulting from imperfect work extraction in the turbines, and in the spoiling effect of the efflux where it renters into the turbine main annulus flow, causing a reduction in the stage efficiency [28].

The design of an efficient internal cooling systems is therefore of great importance for reducing the amount of coolant and then seeking gains in efficiency and component life of the engine [29] [30]. To address this issue, it is useful to introduce the wall thermal effectiveness parameter θ_t, which is often adopted in literature to quantify the capability of the cooling system to refrigerate the walls:

$$\theta_t = \frac{T_W - T_{COLD}}{T_{HOT} - T_{COLD}} \tag{2.38}$$

where T_{COLD} and T_{HOT} are the temperature of the coolant and of the main flow respectively while T_W is the metal temperature of the surfaces.

Nevertheless, designing for cooling system effectiveness first requires an accurate understanding of how the coolant interacts with the flow patterns inside the cavity. Two main aspects have been identified to prevalently affect the cooling effectiveness: the amount of coolant flow rate and the coolant supply geometry.

2.4.1 Effect of the coolant flow rate

Andreini et al. (2008) [31] carried out an extensive numerical investigation on the effect of several coolant flow rates on the flow patterns of a LPT interstage cavity. The coolant is delivered straight radially without angling and the labyrinth seal is a three-fins straight-through seal configuration. Figure 2.15 shows the resulting time averaged vector maps of the flow within the upstream cavity for four different amounts of coolant flow rates, namely 0%, 0.6%, 1.2% and 1.8% of the main annulus mass flow rate. In the figure, the rotor is on the left side and the stator is on the right, the rate of coolant increases from left to right.

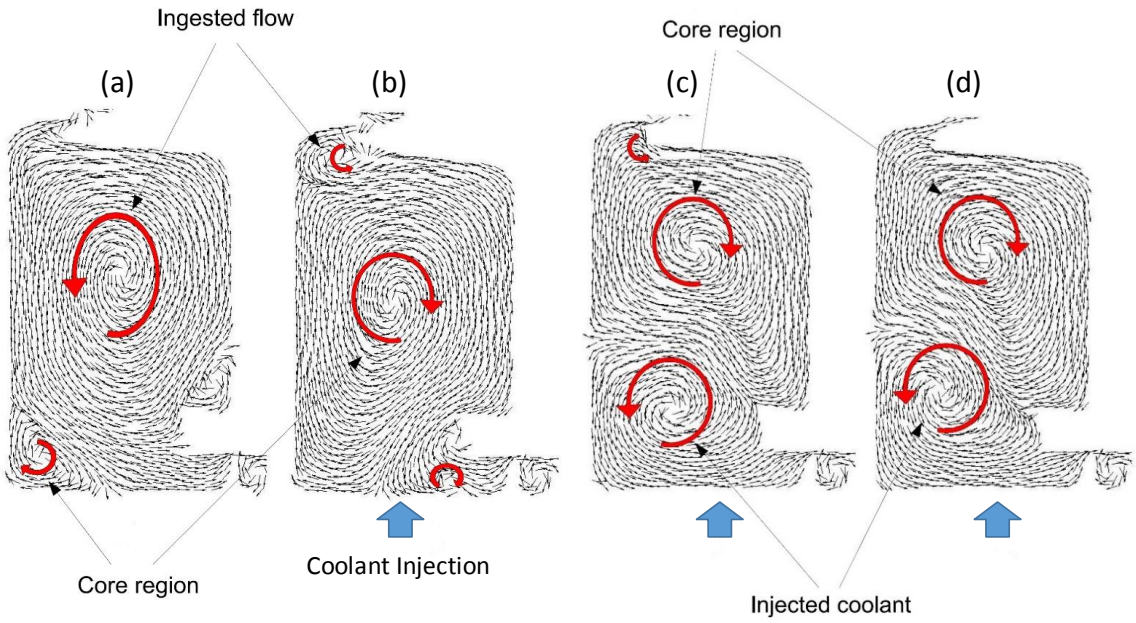

Figure 2.15 Flow field vector map in the upstream rotor-stator system of LPT interstage cavity [31]

In the absence of coolant (figure 2.15a), the flow field is dominated by the ingested flow that generates a wide counterclockwise recirculation. The core flow recirculation lead by the rotor pumping effect (see section 2.2.4), is confined in a small region at the bottom-left side of the cavity. Introducing the coolant in the position indicated by the blue arrow, a modification of the flow structures can be observed. For the lowest coolant flow rate case (figure 2.15b), a large portion of the coolant remains entrained into the rotor disk and the core flow recirculation gradually pushes the ingested flow recirculation outward. The remained coolant passes through the labyrinth seal. For higher coolant flow rates (figure 2.15c and 15d), the momentum of the coolant jet becomes strong enough to overcome the entrainment due to the disk pumping effect. As a result, a new counter-clockwise recirculation, now lead by the coolant, is generated. The disc pumping recirculation remains confined to the outer radii. Finally, in figure 2.15d the recirculation driven by the ingested flow is completely suppressed meaning that the cavity is sealed. In the downstream cavity, there is no significant effect of the coolant on the flow field. There, the flow pattern is characterized by a single counter-clockwise recirculating flow driven by the leakage flow from the labyrinth seal and the rotor pumping effect.

As previously stated, an important parameter which is influenced by the coolant flow rate is the swirl of the flow into the wheelspace. The coolant flow is delivered into the cavity with the same tangential velocity of the disc, thus with swirl factor identical one. Then, the high tangential momentum "propagating" within the cavity depends on the amount of coolant. *Andreini et al. (2008)* [31] provides the contour plots of the local swirl factor (ω/Ω), reported in figure 2.16. In the case without coolant, there is no angular momentum in the flow region dominated by the ingested flow recirculation. The angular speed increases through the seal due to the mechanism described in section 2.3.4, and then reduces in the downstream cavity resulting almost null at the outlet rim position.

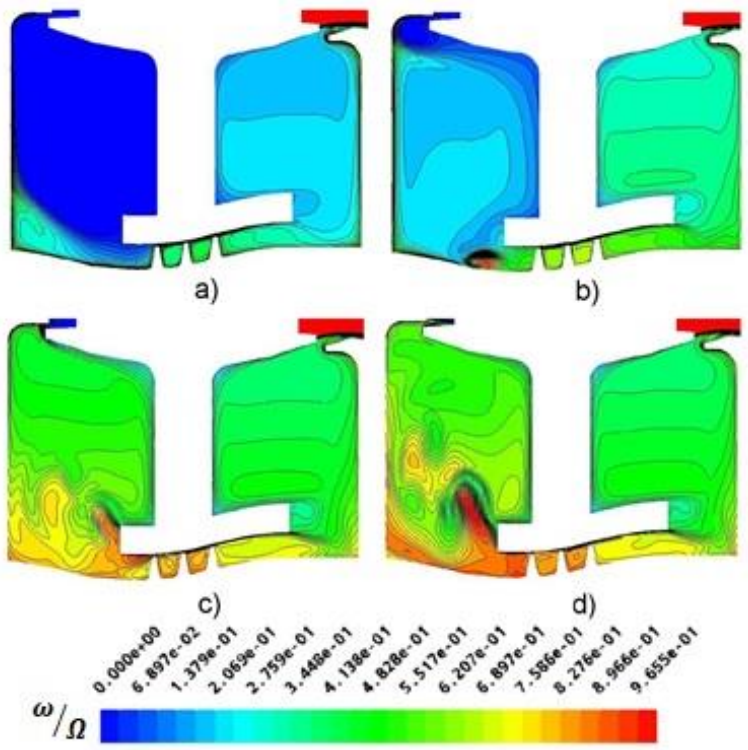

Figure 2.16 Development of the local swirl factor [31]

When the coolant is introduced (figure 2.16b,c and d), the swirl of the flow drastically increases in the region close to point of injection. The rotating core in the upstream cavity grows in magnitude with the increase of the cooling air mass flow rate and its location moves towards to the top of the cavity. In addition, it is important to notice that the swirl factor of the flow at the labyrinth seal inlet also increases with increasing cooling flow. The contours of the local swirl show evidence of a "Batchelor-type flow" in the second cavity. Moreover, the swirl in that region is observed to increase locally as the coolant flow rate is increased.

The analysis of the mass flow rates passing through the labyrinth seal shows that the leakage mass flow rate is almost independent by the cooling air mass flow rate and then mainly determined by the pressure ratio across the vane row in the main annulus. The amount of flow ingested from the main annulus throughout the first cavity rim is equal to the difference between the leakage mass flow rate and the coolant flow rate. However, the reduced labyrinth seal air flow $\dot{m}_l\sqrt{T_t}/p_t$ reduces with respect of the increase of coolant mass flow. This behavior can be related to the increasing swirl of the fluid at the interstage seal inlet described previously [32].

The works of *Schrewe et al. (2012, 2013)* [33] [34] provided interesting measurements of the static pressure distribution within a LPT's interstage cavity. They investigated the effects of several coolant flow rates up to 1.7% of the main annulus mass flow rate delivered straight radially. It was shown that the static pressure increases for low coolant ratios and a maximum is observed for $\dot{m}_c = 0.6\%\, \dot{m}_{FP}$. Then, a pressure drop appears as the coolant flow increases resulting in a smaller pressure compared to the main annulus. A possible explanation to this behavior can be given considering the results of *Andreini et al. (2008).* When the coolant flow rate is increased, the swirl of the inner flow also increases causing a strengthening of the pressure gradient in the radial direction similarly to the mechanism leading to the rotationally induced ingress (see section 2.2.6).

Measurements of the wall thermal effectiveness θ_t were carried out by *Coren et al. (2011)* [35] within an interstage cavity geometry similar to the one analyzed in *Andreini et al. (2008).* The main flow temperature was of about 400K and K-type thermocouples were installed on both the stator and the rotor surfaces of the cavity [36]. They evaluated the effects of four coolant mass flow rates from 0.71 $C_{w,ent}$ to 1.46 $C_{w,ent}$, where $C_{w,ent}$ is the non-dimensional disc entrainment mass flow rate. Their results are provided in figure 2.17 and figure 2.18 for the upstream cavity rotor and stator surfaces, respectively. First, the temperature measured at the outer radial position of the rotor is constant and close to the one of the main flow (figure 2.17). The changes of the temperature gradient, particularly in the outer position ($0.97 < r/b < 1$) of the rotor, is mainly due to the considerable changes in the local aerodynamics behavior that were investigated in *Andreini et al. (2008).* At the lowest coolant flow rate, there is a little change in gradient across the three highest radial positions. The gradient is observed to increase as the coolant flow rate is increased up to $1.13C_{w,ent}$, indicating that the coolant is penetrating to higher radial locations in the cavity. A further increase of the coolant flow rate from 1.13 $C_{w,ent}$ to 1.46 $C_{w,ent}$ yields to a lower increase in the temperature gradient. This indicates, according to the authors, that the cavity is likely to be well sealed and the changes in the cavity flow structures are small. The amount of coolant necessary to seal the cavity were found to be almost two times the one predicted with the correlation presented in section 2.2.6. This discrepancy between the predicted and measured values is likely due to the fact that the correlation of *Phadke and Owen (1988)* [9] does not consider the mechanism of ingestion lead by the pressure ratio across the cavity which, in this case, is predominant.

Similar considerations can be made referring to the results on the stator surface (figure 2.18). Particularly in the outer region, the normalized temperature reduces significantly at the higher coolant flow rates. This confirms that the cavity is sealed but also make evident that an egress of fluid from the cavity into the main annulus could occur at high rates of the coolant flow.

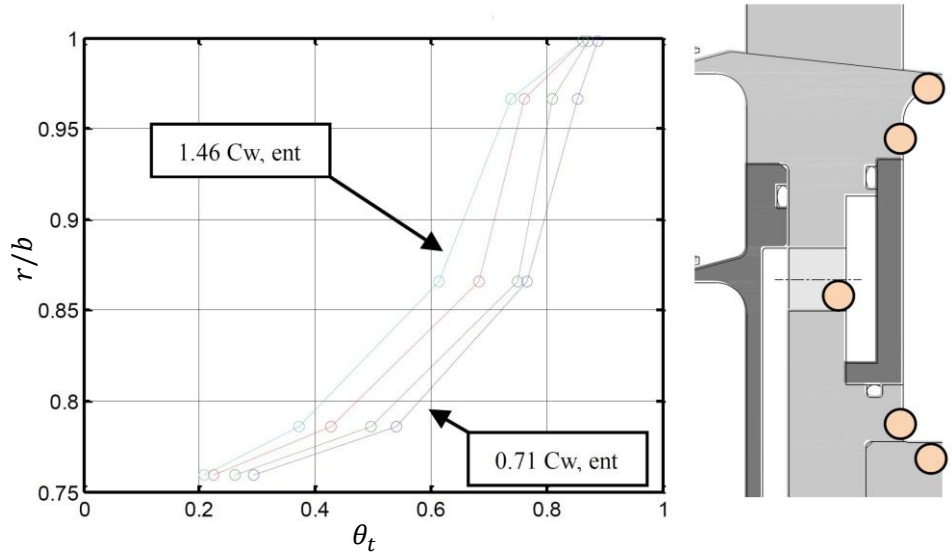

Figure 2.17 Measured rotor wall thermal effectiveness [35]

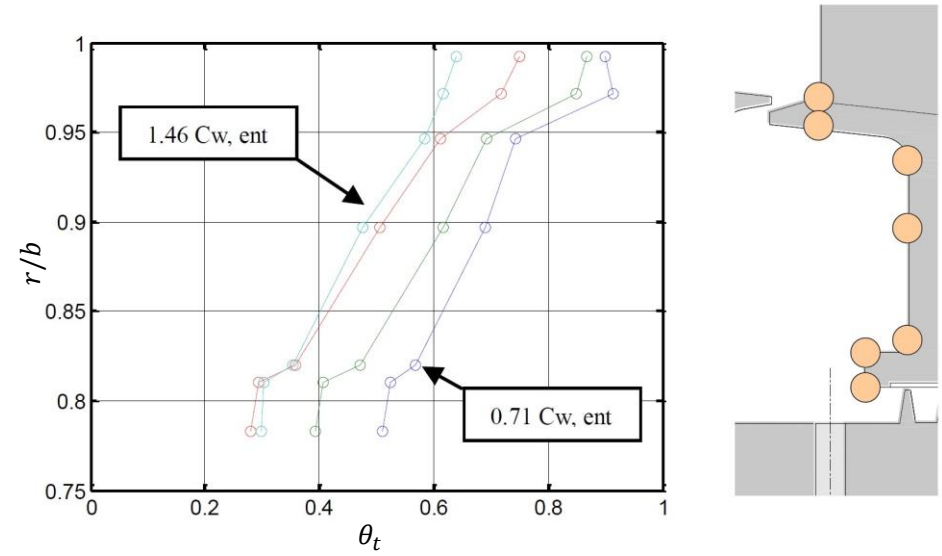

Figure 2.18 Measured stator wall thermal effectiveness [35]

2.4.2 Effect of the cooling supply geometry

In typical engine architectures, the coolant can be delivered either radially (as in the studies presented in the previous section) or axially. *Coren et al. (2011)* [35] investigated both the effects of an axially delivered and a radially delivered coolant in terms of thermal effectiveness. The results were similar suggesting that there is not a substantial difference between the two geometries. Only a slight reduction of the wall thermal effectiveness was observed at the cavity periphery for the axially delivered case with respect to the radially delivered case.

Measurements conducted by *Coren et al. (2011)* [35] showed an improvement of the cooling effectiveness using a delivery geometry with negative axially angled coolant, for a given coolant flow rate. Negative axial angling means that the coolant flow is injected into the cavity towards the rotor wall. Figure 2.19 reports the schematic representation of the measurements. A 10% reduction of the normalized rotor temperature was measured in the angled coolant case in comparison with the standard straight delivery geometry.

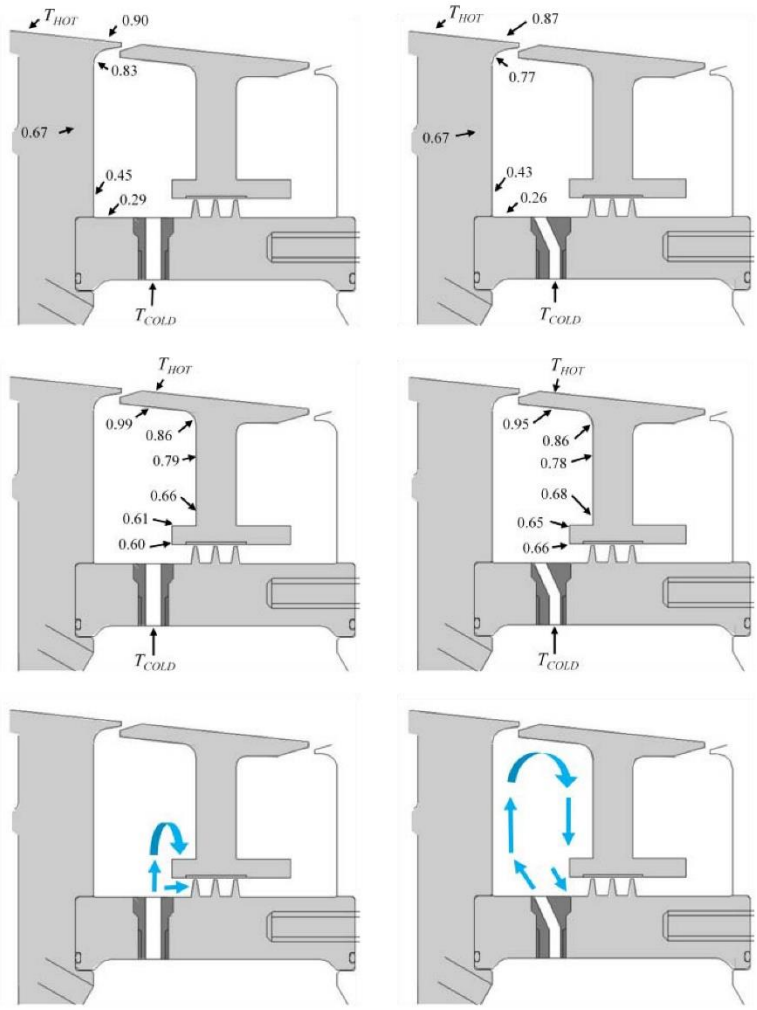

Figure 2.19 Wall thermal effectiveness for straight and axially angled coolant supply system [35]

Da Soghe et al. (2011) [32] characterized numerically the effects of different geometries of the cooling air supplying on wall thermal effectiveness and on the sealing mass flow rate. They considered different coolant supply angling and axial position of the supply holes. The positive axial angling turned the coolant towards the stator while the coolant was injected counter-rotating to the rotor for positive tangential angling.

The CFD results showed that for negative axial angling, the coolant impinges directly on the rotor disc surface and penetrates within the entire upstream cavity surface. On the other hand, for positive axial angling the coolant is injected directly into the interstage labyrinth seal and hence does not contribute to cool the upstream cavity walls. The tangential angling strongly influences the coolant jet penetration within the upstream cavity. With negative tangential angling, a major penetration of the coolant jet was observed. This is mainly due to the higher centrifugal forces acting on the coolant particles as well as a minor drag between

the coolant jet and the cavity flow (that rotates in the same direction of the coolant) making a radial penetration easier. The better enhancements in term of wall thermal effectiveness were found by coupling the negative axial angling with the negative tangential angling. In this case the computed streamlines of the coolant flow have been found to flow through the entire upstream cavity surface. The computed thermal effectiveness keeps extremely low on the stator surface and on the upstream rotor wall. Finally, this study also pointed out that a straight supply position close to the rotor side wall give enhancement similar to those shown by negative angling.

2.5 Main Annulus and Cavity Flows Interaction

The cavity flows and the main flow interact in the region where the gas enters and leaves the cavity [37]. The importance of the endwall cavity flows on the gas path aerodynamics have been largely investigated in literature due to their potential to provoke significant efficiency penalties in gas turbines [38]. The mixing process between the low momentum cavity fluid and the main annulus flow represents the main driver of these losses. Furthermore, the interaction results in a stronger secondary flow generation system [39] [40] and in a reduction of the incidence angle at the vane inlet that could lead to local flow separation on the vane pressure side [41] [42] [43]. Overall, these factors significantly affect the stage losses [44] [45].

Gier et. al (2005) [37] reported on a comparison between two CFD models of a two stages axial turbine. The first model considered an ideal flow path without endwall cavities while the latter introduced the hub interstage cavities at the bottom of the vane rows and the tip seals of the blade rows. The experimental data obtained on the same turbine geometry with cavities were also adopted for validation. They found a large reduction of the isentropic efficiency of the vane row in the endwall region between the ideal flow path and the cavity computation. This reduction is about 2.6% with respect to the no-cavity value, and depends on the operating Reynolds number.

The comparison between the two computations also showed an increased negative incidence at the vane inlet along the entire span height. Particularly, a reduction of about five degrees was observed close to the hub endwall. Consequently, at 10% of the span height, the vane aerodynamic load for the cavity computation is lower than the one for the ideal flow path. This is reported in figure 2.20 were also the experimental data that well match the CFD data (with cavity), are included.

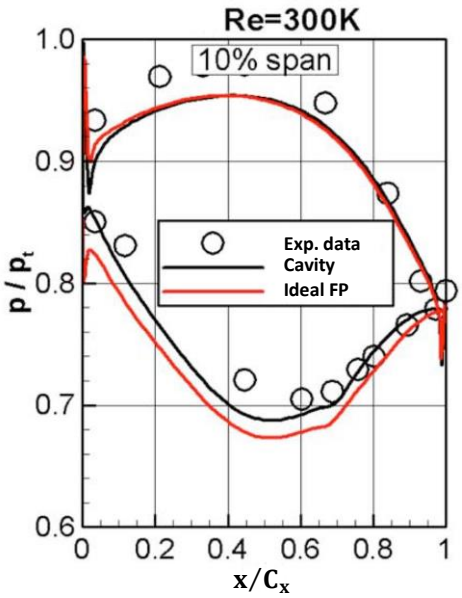

Figure 2.20 Static pressure distributions on the vane profile: ideal flow path computations(red line), cavity computations (black line), experimental data (round points) [37]

In *Gier et. al (2005)* [37] the effect of the cavity on the development of the secondary flow structures across the vane row was described. They reported on a thicker endwall boundary layer at the vane inlet position that intensifies the formation of the passage vortex through the vane channel. Figure 2.21 shows the total pressure fields computed for the two models. The total pressure minimum related to the passage vortices becomes more pronounced for the cavity computations but also moved radially away from the endwalls into the main flow. Several authors stated that the low momentum fluid that egress from the cavity remains entrained into the passage vortex in their path through the vane channel [42]. The strength of the passage vortex at the tip, is influenced by the tip leakage flow of the upstream rotor row. At the hub, the vortex intensification process is weaker than at the tip since a part of the boundary layer is sucked into the hub cavity upstream of the vane and hence does not contribute to disturb the vane inlet boundary layer.

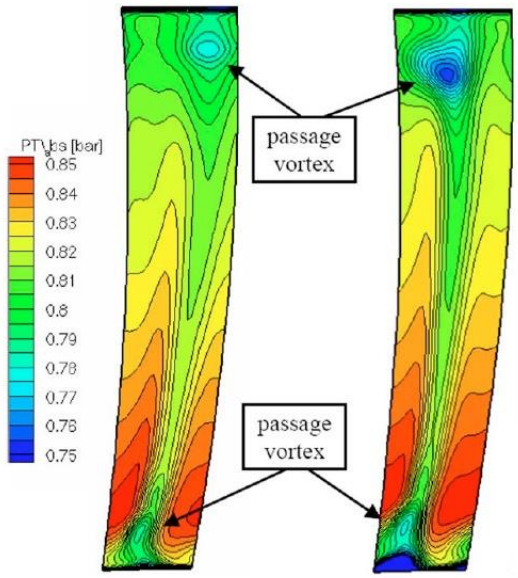

Figure 2.21 Total pressure distribution in axial plane downstream of the vane (outlet hub cavity location). On the left: ideal flow path computations; on the right: cavity computations [37]

Schrewe et al. (2012) [34] carried out an experimental campaign in a two stage axial turbine, with the aim of investigating the effect of several amount of flow rate on the interaction between rim seal and main annulus flow. The interstage cavity is located under the second vane row. They adjusted the coolant flow rate in order to generate ejection or injection of specific mass flow rate through the rim seal upstream of the vane row (see the scheme in figure 2.22). They considered a single case where the mainstream enters the cavity through the rim with a rate of flow around 0.28% of the main annulus mass flow rate and several cases where the fluid leaves the cavity with flow rates up to 3%.

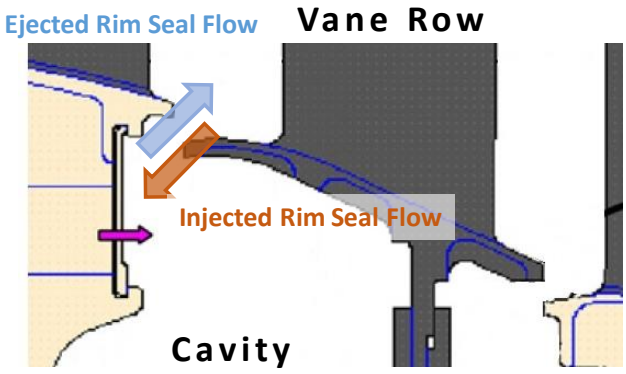

Figure 2.22 Representation of the rim seal flows

In the region from 0% to 20% of the span height at the vane inlet plane, the flow is decelerated, on averaged, as the rim seal flow rate is increased whereas the inner flow accelerated. This makes evident that the cavity flow entering the mainstream upstream of the vane acts as a blockage towards the main flow. In addition, the circumferentially averaged radial flow angle increases with increasing seal air mass flow so that, for small rim seal flow, the flow direction is towards the hub whereas for high seal air rates, it is towards the outer casing.

The measurements carried out by *Schrewe et al. (2012)* by means of a 5-hole pressure probe, indicated a strong variation of the pressure losses across the vane due to different rim flow rates. Figure 2.23 shows the contour plots of the total pressure loss coefficient (ζ), measured across the vane for different rim seal injections (the negative value means ingress of flow into the cavity whereas positive values are related to egress flow). There are no significant variations of the flow in the upper half of the annulus. Close the hub, the loss core related to the secondary vortices intensifies as more low momentum flow, that egress from the cavity upstream of the vane, remains entrained into the vane passage vortex [39]. This latter observation was also confirmed by temperature measurement in the main annulus using cold injected air. The loss core is pushed radially outward as the rim flow injection increases thus with increasing radial flow in the inlet vane section. This behavior is similar to what observed in the CFD investigation of *Gier et. al (2005)* (see figure 2.21).

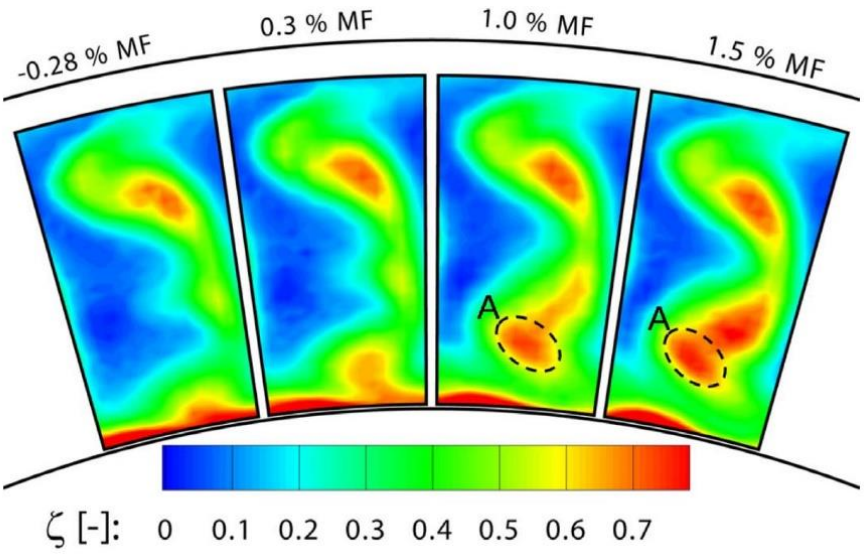

Figure 2.23 Total pressure loss coefficient for different coolant injection rates [34]

The pressure distribution of the vane profile effectively showed a variation of the load with the injected flow rate. The region close to the hub is influenced at the leading edge with a reduction of the load as the rim seal flow rate is increased. Moving towards midspan, it is the rear loading being affected by the flow ejected from the cavity. The pressure side remains unaltered but the pressure on the suction side decreased causing slight increase of the load. At midspan the pressure distribution was unaltered. This is due to the secondary flow that generates close to the hub at vane inlet and moves radially outward in its path through the vane channel.

Measurements of the Mach number revealed a global acceleration of the flow at the vane exit plane. Close to the hub, the Mach number is increased stronger than averaged due to the increased mass flow rate in the annulus downstream of the seal air injection. In addition, the tangential and the radial flow angles were observed to change significantly with the seal air injection rate. The spanwise distribution of the measured tangential flow (yaw) angle is shown in figure 2.24 with the reference metal angle of the vane profile. Particularly the underturning and overturning regions were intensified by the seal air injection. It is therefore evident that the cavity-main flow interaction not only affects the performances of the vane row but also influences the flow field at the subsequent row inlet. Hence, it could represent an additional source of losses for the stage. To this end, *Schadler et al. (2017)* [46] showed an improvement of the mainstream properties using a purge control feature at both the cavity rim seals in order to induce a higher tangential velocity to the rim seal flow and then reduce the mixing losses. The work indicates the possibility to improve the stage aerodynamic efficiency developing new optimized rim seal geometry.

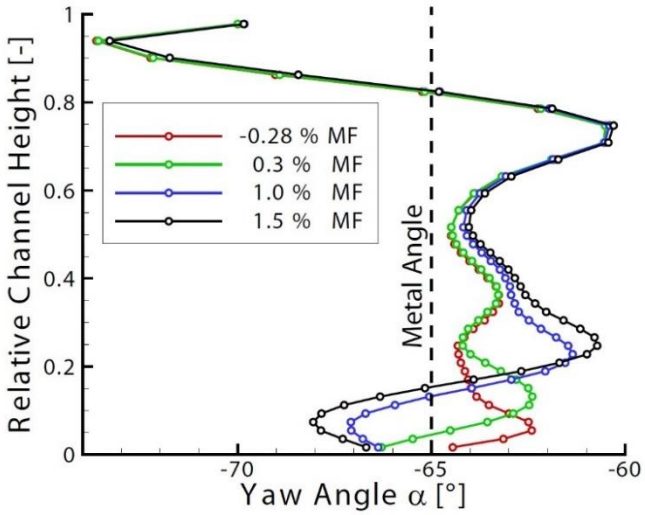

Figure 2.24 Radial distribution of the yaw angle downstream of the vane for different injected mass flow rate [37]

Chapter 3 - EXPERIMENTAL FACILITY

The experimental investigation of the flows evolving within a turbine interstage cavity and its interaction with the main flow path has been carried out on the dedicated test facility installed at the Aerodynamics and Turbomachinery Laboratory of the University of Genova shown in figure 3.1.

The test rig was specifically designed and developed with the aim of reproducing the main geometrical parameters and governing non-dimensional numbers that characterize the development of cavity flows in low pressure turbine modules in gas turbines for aeronautical applications. The experimental apparatus is a large scale rotating test facility. The test section is constituted by one-and-half turbine stages equipped with a realistic cavity configuration in the bottom of the vane row. Additional slots, realized on the rotor part of the cavity, allow simulating the coolant flow injection. The following chapter provides a detailed description of the test facility and the capabilities in terms of reproduced non-dimensional numbers hence test conditions.

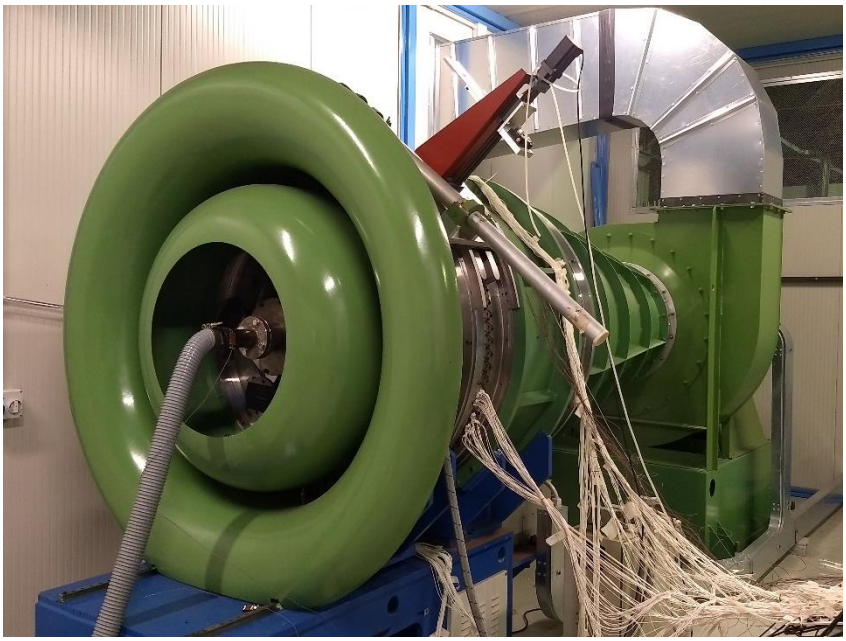

Figure 3.1 Test facility

3.1 Modelling Flow-Dynamics

Figure 3.2 provides a graphic representation of the interstage cavity geometry of interest and the flows involved within it. The cavity separates the two rotor disks upstream (*rotor#1*) and downstream (*rotor#2*) from the vane row (*stator#1*). The static part of the cavity is named T-bar (easily recognizable due to its shape). Two horizontal tooth are located at the cavity inlet and outlet section while a two-fins straight through labyrinth seal is installed in the middle. Particularly, in this architecture, the coolant is delivered axially through the upstream rotor sidewall.

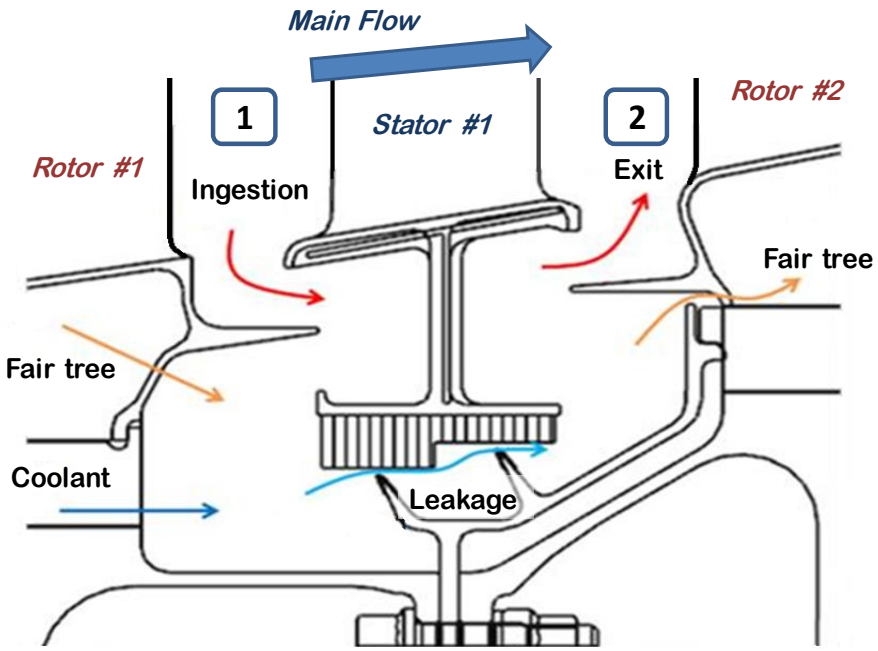

Figure 3.2 Schematic representation of the cavity engine configuration with characteristic flows

In order to reproduce the flow development in the real engine, the geometrical, kinetic and dynamic similarity conditions must be respected. Thus, the governing non-dimensional numbers and geometrical parameters had been identified during the early stages of the design. The insights provided by the literature survey suggest that the flow patterns within the cavity and in the hub region of the main annulus are mainly characterized by the leakage flow rate $\dot{m}_l$ and the main flow properties in the inlet and outlet sections of the vane. Thus, the Buckingham-π-theorem analysis allows identifying the non-dimensional numbers driving the cavity performances:

$$\frac{\dot{m}_l\sqrt{R_{gas}T_{t1}}}{Ap_{t1}} = C_D\mathcal{F}(\beta, k) \tag{3.01}$$

$$C_D = \mathcal{G}\left(Re, S_w, geometry, C_{w,c}\right) \tag{3.02}$$

where T_{t1} and p_{t1} are the inlet total pressure and total temperature of the fluid, A is the characteristic passage area of the leakage flow and k is the ratio between the specific heats that denotes the type of fluid. $\beta = p_{t1}/p_2$ is the total to static pressure ratio across the vane upside the cavity. It forces the passage the flow within the cavity and across the labyrinth seal while the discharge coefficient C_D accounts for real effects influencing the dynamics of the cavity flow during the migration from the inlet to the outlet section. The functional relation for the C_D has been written similarly to the one given by *Denecke et al.* for rotating labyrinth seals. The influence of the coolant has been introduced into the relation in the form of the non-dimensional coolant flow rate $C_{w,c}$. The general term *geometry* indicates the necessity to keep the geometrical similarity of the cavity thus reproducing the same cross-sectional area of the engine. The definition of the Reynolds number Re, inlet swirl factor S_w and non dimensional coolant flow rate, are given in the following:

$$Re = \frac{v_{z,id}L}{\nu} \tag{3.03}$$

$$S_w = \frac{v_{\phi,1}}{\Omega b} \tag{3.04}$$

$$C_{w,c} = \frac{\dot{m}_c}{\mu R_c} \tag{3.05}$$

the Reynolds number is defined with the axial velocity of the main flow considering an isentropic passage across the vane, and the axial length of the cavity. The swirl factor S_w is the ratio between the tangential velocity of the flow at the vane inlet section and the circumferential velocity of the rotor at the rim radius, thus taking into account the effects of rotation. It is directly related to the well known flow coefficient $\varphi = v_z/\Omega r$. It makes further evident the necessity to keep the kinematic similarity of the flow in the vane inlet and outlet planes. Finally, in the definition of $C_{w,c}$, $\dot{m}_c$ is the rate of coolant and R_c is the radius at which the coolant is delivered.

3.2 General Layout

The meridional view of the experimental apparatus can be observed in figure 3.3. It is a cold flow rotating test facility that uses atmospheric air as working fluid. The overall installed electric power of the facility is 300kW. A centrifugal fan of nominal 250 kW power, located downstream of the rig, is adopted to feed the main flow path and to apply the demanded expansion ratio in the test section. The design value mass flow rate in the main path is around 15 kg/s corresponding to a total-to-static pressure ratio across the vane of 1.2. The axis of rotation is horizontal and a 26.5 kW two-pole electric motor moves the turbine shaft up to 2000 rpm. Both rotational speed of the fan and the turbine shafts can be modulated continuously using inverters in order to vary the operating conditions.

The test section simulates one-and-half turbine stage with an upstream distributor row generating the needed inlet flow angle. The cavity is installed in the bottom of the vane row. The large amount of kinetic energy of the flow at the exit of the test section is recovered by a four row diffuser.

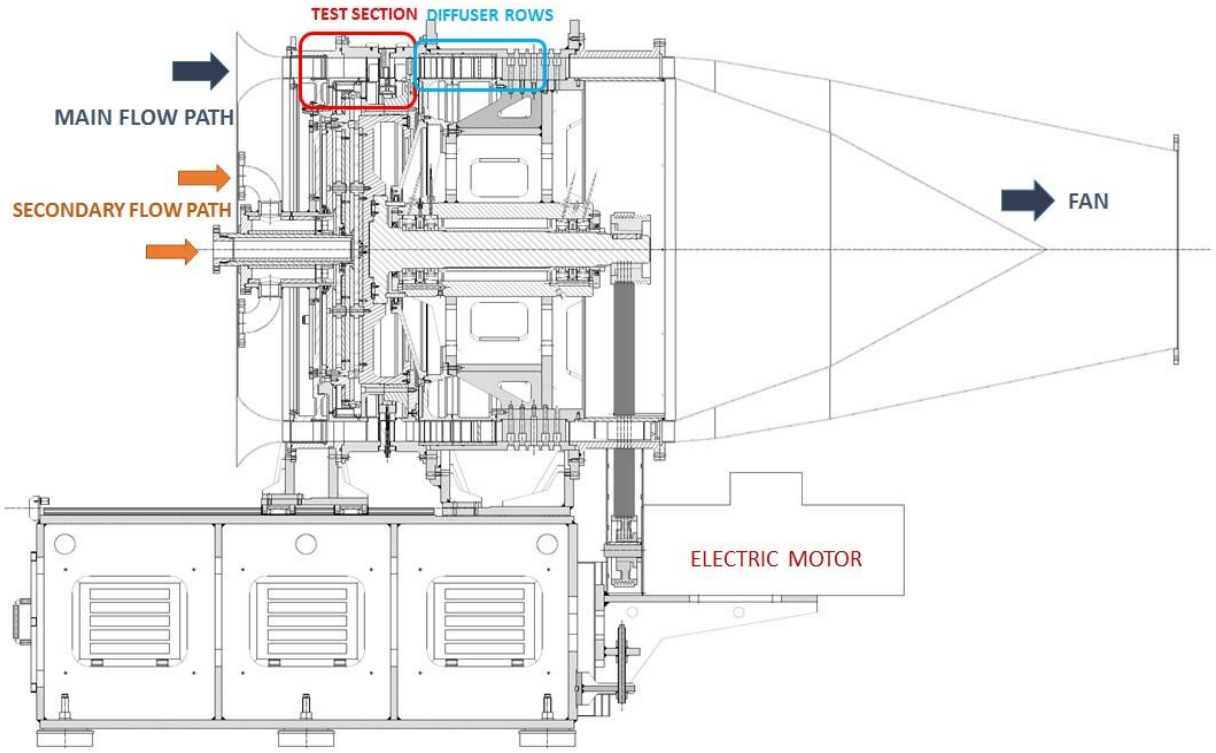

Figure 3.3 Meridional view of the test rig

3.2.1 Test section

A detailed view of the test section is given in figure 3.4. The main path simulates a one-and-half turbine stages with a real vane profile and two rotating bar systems simulating both viscous and potential effects on the vane and cavity aerodynamics. The bell-mouth inlet has been designed in order to have a high radius of curvature, thus minimizing the occurrence of boundary layer separation at the inlet, as well as to have a distance between the facility inlet and the stator assuring good inlet flow uniformity.

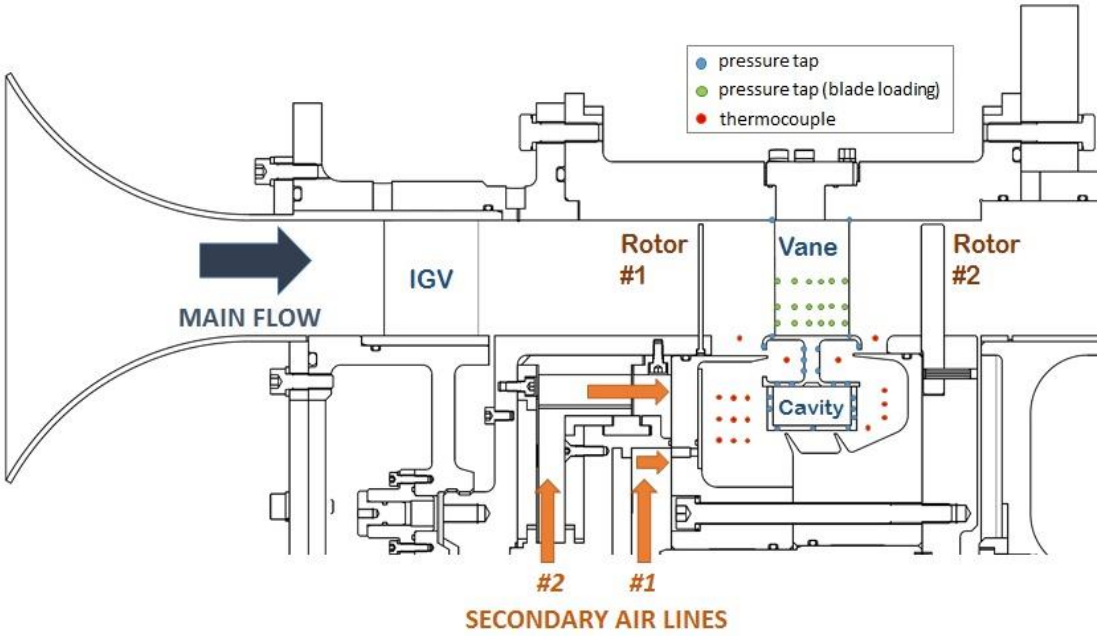

Figure 3.4 Cross-sectional view of the test section

The interstage cavity geometry is representative of an engine configuration (see figure 3.2) with an increased scale ratio of *1.5:1*. This increases the spatial resolution of the measurements and facilitates the access of the probes within the cavity. The streamwise length of the cavity is 117 mm and the outer rim radius is 501 mm. The nominal clearance of the labyrinth seal is 1.7 mm only. The picture on the left in figure 3.5 shows a cross-section of the vane row and the static part of the cavity. On the right picture, the rotating boundaries of the cavity and details of the teeth of the labyrinth seal are shown.

The vane row is constituted by 84 cylindrical blades. The blade-to-blade profile is directly scaled from a typical engine blade. The vane chord *C* is 59 mm with an aspect ratio equal to 1 while the pitch to chord ratio is 0.66 evaluated at the hub. The design flow angles at the vane inlet and exit planes are -39.8° and 68.8°, respectively with respect to the axial direction.

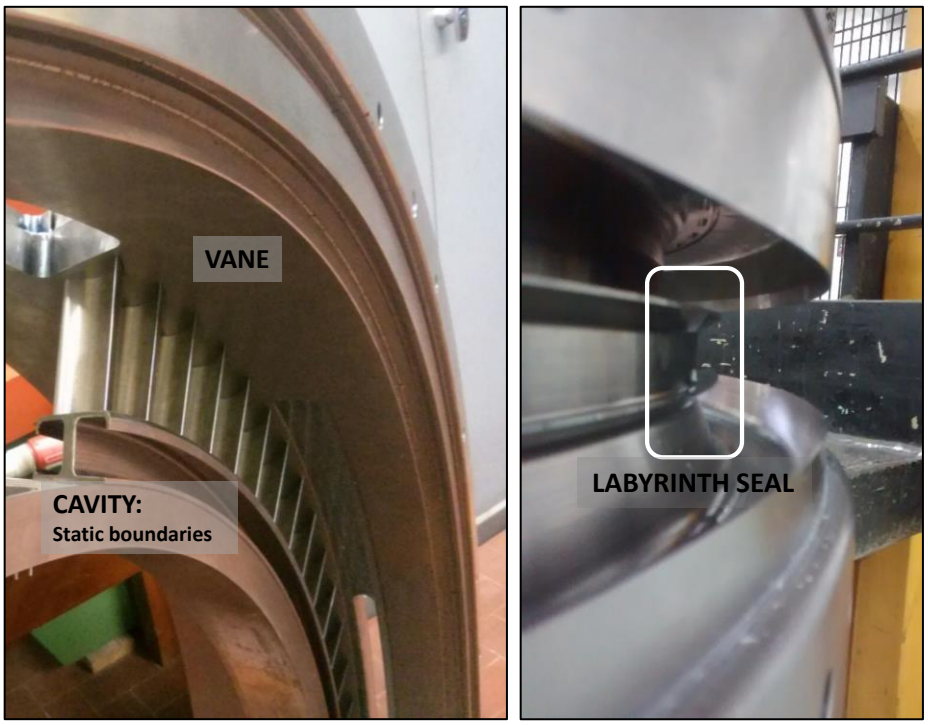

Figure 3.5 Static part of the cavity and vane row (on the left); rotating boundaries of the cavity with detailed view of the labyrinth seal fins (on the right)

The two rotating bar systems (*rotor #1* and *#2* in figure 3.4) are constituted by 63 bars each. The ratio between the vane number and bars is 4:3 in order to reduce computational efforts in simulating the rig geometry thus allowing comparison with unsteady CFD analysis to be carried out in the future. The upstream bar-vane gap is equal to 65% of the vane chord while the downstream bar row is located 75% of C far from the vane trailing edge. *Pfeil and Eifler* [47] showed that the wake shed by a blade can be accurately reproduced by a cylindrical bar which produces the same drag of the blade. Following their theory, in order to choose the upstream bar diameter, it has been used equation (3.06):

$$Y_p = \frac{c_d \cdot D}{g_{bar} \cdot \cos \alpha_1} \tag{3.06}$$

where Y_p is loss coefficient to reproduce, associated to the upstream row, g_{bar} is the bar pitch at midspan, c_d is the drag coefficient referred to a cylinder (for the considered interval of the Reynolds number in this work it is equal to 1), α_1 is the relative inlet flow angle and D is the desired bar diameter. Therefore, the upstream bar diameter has been set to 2 mm (see figure 3.6). On the other hand, the downstream bar diameter has been designed in order to reproduce the same potential field induced by the downstream blade row. *Opoka and Hodson (2008)* [48]

showed cascade testing results with both upstream and downstream rotating bars. The same ratio between the bar diameters (~6) of the rig of *Opoka and Hodson (2008)* has been adopted to scale the downstream bar diameter, so that 12 mm diameter bars have been installed. Detailed geometrical information on the bar systems are given in table 3.2.

The pre-distributor row, located just downstream of the bell-mouth inlet, turns the flow from the axial direction to around 40 degrees just upstream of the first rotating bars. The row is composed by 84 profiles with axial chord of 50.2 mm. The exit flow angle imposed for designing the IGV profile has been corrected considering the variation of the incidence angle induced by the rotating bars on the downstream vane (see [49]). To this end, the correlation developed by *Berrino et al. (2014)* [50] has been adopted to derive the design flow angle (see table 3.1 for further details).

Figure 3.6 Upstream rotating bar system

			IGV	VANE
Number of blades	*n*	[-]	84	84
Chord	*C*	[mm]	56.7	59
Axial chord	C_z	[mm]	50.2	39
Pitch at the hub	*g*	[mm]	37.5	37.5
Span	*S*	[mm]	59	59
Aspect ratio	*S/C*	[-]	1.04	1
Pitch to chord ratio	*g/C*	[-]	0.66	0.64
Inlet flow angle	α_1	[°]	0	39.8
Outlet flow angle	α_2	[°]	43.1	68.8

Table 3.1 Main features of the IGV and vane rows

			Rotor #1	Rotor #2
Number of bars	*n*	[-]	63	63
Diameter	*D*	[mm]	2.2	12
Pitch at the hub	*g*	[mm]	59	59
Span	*S*	[mm]	57	57
Distance from vane trailing edge	*d*	[mm]	76.9	38

Table 3.2 Main features of the rotating bar systems

3.2.2 Auxiliary air lines

The rig is equipped with two auxiliary air lines derived into the rotor disk. They are portrayed in figure 3.4 and allow delivering air flow within the cavity. The first (path #1 in figure 3.4) simulates the coolant flow that in the real engine is delivered to seal the cavity and refrigerate the discs. The latter (path #2) is introduced with the aim of reproducing the portion of the main flow that passes through the fair tree of the upstream rotor row (see the scheme of flows portrayed in figure 3.2). The air lines are fed by two independent centrifugal fans upstream of the rig. Maximum mass flow rates are summarized in table 3.4.

The delivery geometry is reproduced similarly to the engine one. Therefore, both air flows are purged axially into the cavity through two series of 63 slots each manufactured on the side wall of the rotor. A sector of these slot series is shown figure 3.7. The coolant flow enters the cavity through the down series that is composed by circumferentially extended slots. The fair tree leakage flow pass through the upper radial slots. Otherwise, the slots can be locked up in order to perform the aerodynamic characterization tests without additional flows.

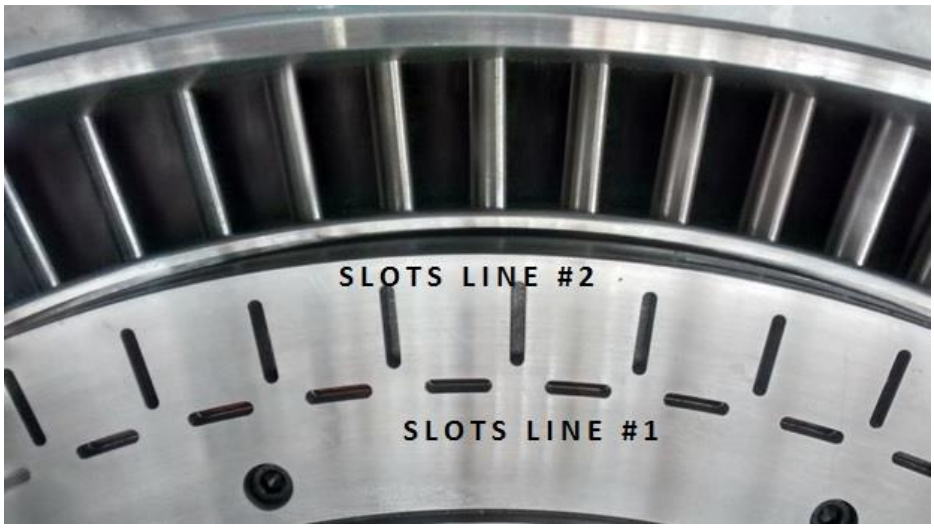

Figure 3.7 Delivering slots of the secondary air lines

The temperature of both the secondary air streamtubes can be varied in order to provide an evaluation of the thermal stratification between the different streams into the cavity, as well as the mixing process between the cooling air and the cavity flow. An electric heater of 35kW is adopted to heat the secondary air stream-tubes up to 100°C and 75°C, depending on the mass flow rate. In order to minimize the heat losses due to thermal dispersion at the wall, the boundaries of the secondary air lines are insulated using slabs made of teflon.

3.2.3 Downstream diffuser

The flow in the outlet plane of the test section possess a high amount of kinetic energy due to the high tangential flow angle at the exit of the vane. In the nominal operating conditions, the dynamic pressure associated to the tangential velocity of the flow is around 16 kPa. The recovery of this amount of pressure is of great importance to allow feeding the rig with the needed mass flow rate and keeping the power of the main fan within the installed electric power of the facility. A four row diffuser has been designed and installed downstream of the second bar row with the purpose of turning the flow from 70° up to around 0°.

The blades are made of steel foil of about 2 mm of thickness. The shape of the foil is molded upon an arc of circle where the curvature depends on the deflection imposed to the flow through each row. The overall turning angle of around 70° is distributed on the four rows with a lower deviation in the first row and a higher one in the subsequent rows (see table 3.3). The blades are manufactured with a 60 mm chord and the blade count has been obtained by considering a solidity of 1.5 for each row. Details of the diffuser geometrical parameter design quantities are given in the following table.

			DF row#1	DF row#2	DF row#3	DF row#4
Blade count	*n*	[-]	84	84	84	84
Inlet flow angle	α_1	[mm]	70	60	45	30
Flow deflection	ϑ_c	[°]	10	15	15	30
Stagger angle	γ	[°]	61.5	48.5	36	11
Chord	*C*	[mm]	60	60	60	60
Pitch at midspan	*g*	[mm]	40	40	40	40
Solidity	*C/g*	[-]	1.5	1.5	1.5	1.5

Table 3.3 Main fetures of the diffuser rows

3.3 Test Conditions

The design point of the rig is representative of the operative engine conditions at take-off. To this end, values of the non-dimensional parameters corresponding to the nominal operating point of the rig are summarized in table 3.4.

Operative parameters of the rig can be modulated in order to test different working points of different engines. The regime of rotation of the main fan can be varied via inverter so that the main annulus mass flow rate can be varied to test different Reynolds numbers and pressure ratios. Similarly, the rotational speed of the disk can be modulated acting on the inverter that controls the driving electric motor. This allows testing the effect of rotation on the aerodynamic performances of the cavity. The minimum rotor speed is around 200 rpm that can be increased up to 2000 rpm at the maximum mains frequency. In addition, the coolant and fair tree leakage flow rates, and their temperature, can be varied acting on the respective driving fans and the electric heater. The range of variation of each rig operating parameter is give in table 3.4.

The plot in figure 3.8 provides a representation of the rig testing capabilities. The area covers different characteristic operating conditions (from take-off to cruise) of different engines. The blue square represents the nominal design point of the rig while the other points corresponds to the operating conditions tested throughout the activity presented in this thesis. More details of the tested conditions will be provided in the following chapters.

It is worth mentioning that the facility has been designed also to allow an easy substitution of the rotor disk so that different cavity geometries and vane profiles could be tested. In addition, the rotor disk allows the installation of a blade row downstream of the vane in order to test the cavity related effects on the subsequent row.

			Nominal	Range of variation
Vane expansion ratio	β	[-]	1.2	1.001 ÷ 1.20
Reynolds number	*Re*	[-]	500000	50000 ÷ 600000
Swirl factor	S_w	[-]	0.7	0 ÷ 7
Rotational speed	Ω	[rpm]	1500	0 ÷ 1500
Main annulus mass flow rate	$\dot{m}_{FP}$	[kg/s]	14.6	1.5 ÷ 14.6
Coolant flow rate	$\dot{m}_C$	[kg/s]	0.6	0 ÷ 1
Fair tree leakage flow rate	$\dot{m}_{ft}$	[kg/s]	0.3	0 ÷ 1

Table 3.4 Rig operating parameters

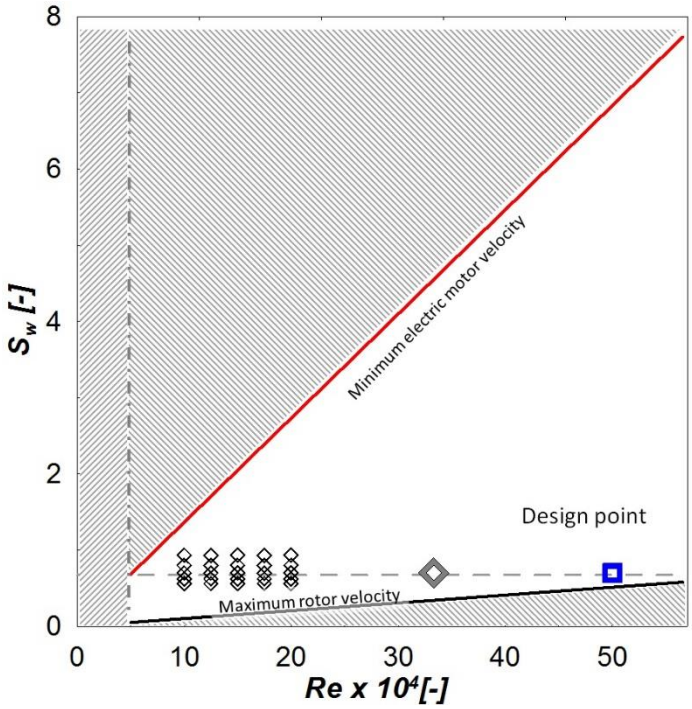

Figure 3.8 Range of variation of the rig main governing parameters

Chapter 4 - TEST RIG INSTRUMENTATION

The main objective of the experimental campaign presented in this thesis is to provide an aerodynamic characterization of cavity flows and the related effects on the flow developing through the stator row. To achieve these purposes, the test section has been heavily instrumented in order to measure the following quantities:

1. Static pressure distribution:
    a. Pressure drop across the labyrinth seal;
    b. Static pressure distribution on the T-bar;
    c. Circumferential static pressure distribution of the main flow at the vane hub and tip;
    d. Vane loading at different span heights;
2. Air temperature distribution inside the cavity;
3. Actual clearance of the labyrinth seal during tests;
4. Aerodynamic efficiency of the vane row due to main flow-leakage flow interaction upstream and downstream of the vane;
5. Leakage mass flow rate;

Three sectors of the rig test section, equally spaced along the circumferential direction, have been instrumented with an overall amount of 232 pressure taps and 27 thermocouples. The first sector is instrumented with the larger amount of probes (about 120 pressure taps and 20 thermocouples) while the remaining sectors allow verifying the circumferential periodicity of the flow. One additional section is equipped with a traversing system in order to perform measurements by means of kiel probe in the main annulus. Another section is equipped with a displacement sensor in order to measure the running clearance of the interstage labyrinth seal. An overview of the probe position in the main sector is given by figure 4.1.

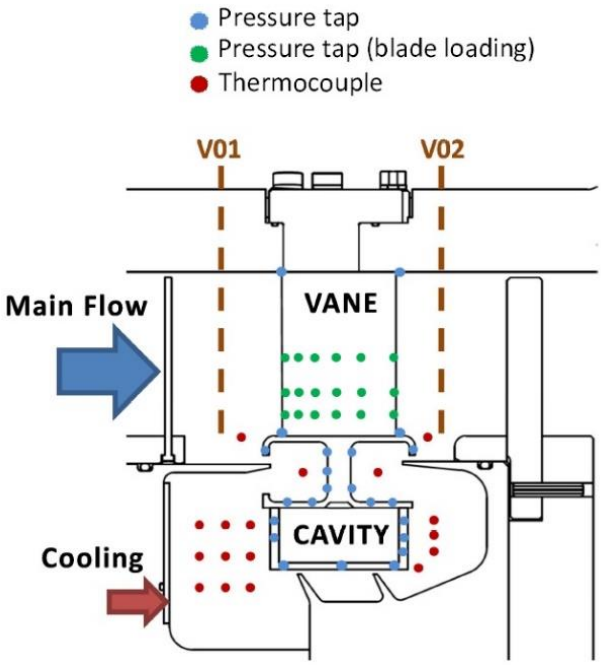

Figure 4.1 Probe position in the test section

4.1 Static Pressure Distributions

Pressure taps of about 0.5 mm of diameter are manufactured in the key points of the test section in order to describe the mainstream and cavity flow aerodynamics. A Scanivalve ZOC17 electronic pressure scanning module (shown in figure 4.2) has been adopted. The ZOC17 is equipped with 16 individual temperature compensate, piezo-resistive pressure sensors. The full scale range is ±2.5 kPa and the sensor accuracy is ±0.20% of the full scale value. An additional set of four SETRA differential pressure transducers have been adopted to acquire pressure signals. The full scale range is ±3 kPa with an accuracy of 0.08% of the full scale.

Figure 4.2 Scanivalve ZOC17 electronic pressure scanning module

4.1.1 Vane loading

The aerodynamic vane loading distributions are measured at different span heights. Three vanes were instrumented with 16 pressure taps each, at midspan, 25% and 10% of the span height. The pressure taps are evenly spaced along the blade surface: nine of them are located on the suction side, five on the pressure side and the remaining two on the trailing and leading edge, respectively. Figure 4.3 shows the pressure tap position on the vane profile. The three instrumented vanes are manufactured with DMLS additive manufacturing technique in order to realize the taps on the vane surface and create the inner paths that allow to connect the holes to the pressure transducers. The pictures of the three instrumented vanes are shown in figure 4.4.

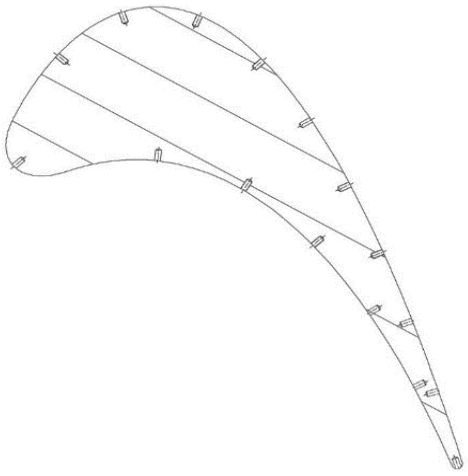

Figure 4.3 Pressure tap distribution on the vane profile

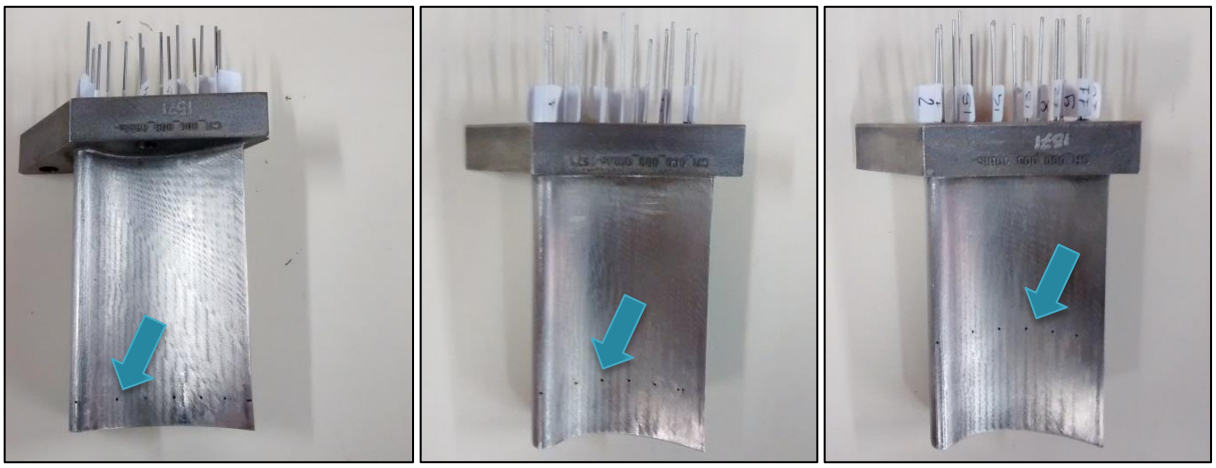

Figure 4.4 Instrumented vanes for loading measurement at 10%, 25% and 50% of the span height

4.1.2 Pressure distribution at the hub and tip

The circumferential static pressure distribution in the upstream and downstream plane of the vane has been measured in correspondence of the tip and the hub radius. To perform this measurement, three integral two-vane components are manufactured using DMLS additive manufacturing technique and installed in the three instrumented sectors of the rig. Four series of pressure taps each are manufactured at the vane hub and tip positions, 1 mm far from the leading edge (upstream of the vane) and 1 mm downstream of the training edge. Eight pressure taps equally spaced along one pitch of the vane compose each series. Figure 4.5 shows a detailed view of the tap series upstream of the vane located at the hub. In this way, the resulting spatial resolution is about 0.5° corresponding to ~4.5 mm at the hub and ~5.2 mm at the tip. Figure 4.6 shows a CAD section of this component that highlights the tap position at the hub, where y/g is the non dimensional pitchwise coordinate. The positioning at the tip is the same.

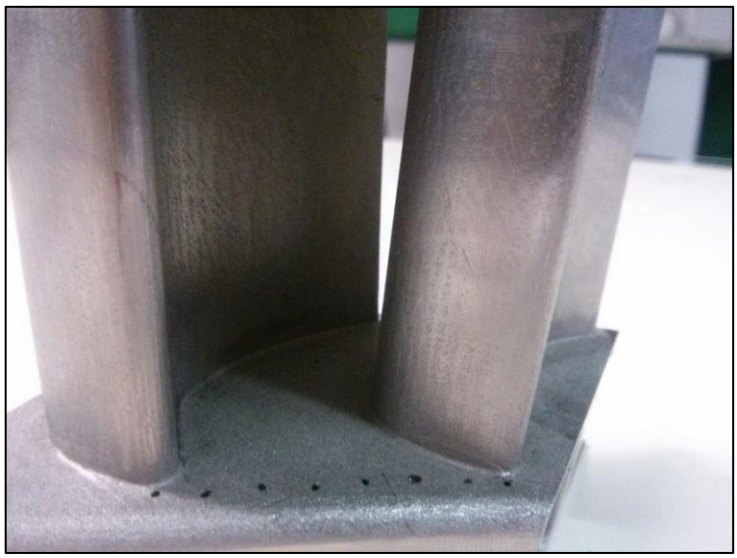

Figure 4.5 Pressure taps at the vane hub in correspondence of the leading edge

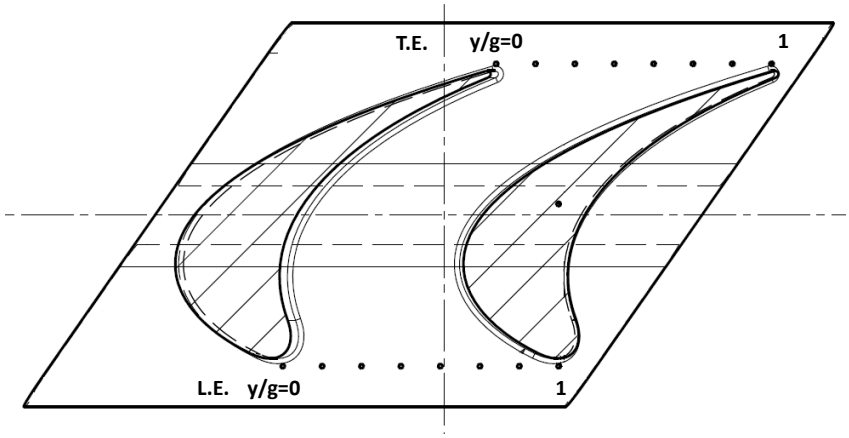

Figure 4.6 Pressure taps position at the vane hub

4.1.3 Cavity and interstage labyrinth seal

The static pressure distribution through the labyrinth seal is measured in each of the three instrumented sectors. The measurement is carried out by means of three series of taps manufactured on the upper stator plate of the labyrinth seal. These series are located upstream and downstream of the seal fins and in between the two tooth. Each series is constituted by 8 pressure taps (0.5 mm of diameter) equally spaced in the circumferential direction along an angular distance of two vane pitch. A spatial resolution of about 1° is ensured, that corresponds to 8 mm at the local radius. Figure 4.7 shows a look from above of the static part of the cavity that makes further evident the position of the pressure taps on the interstage labyrinth seal.

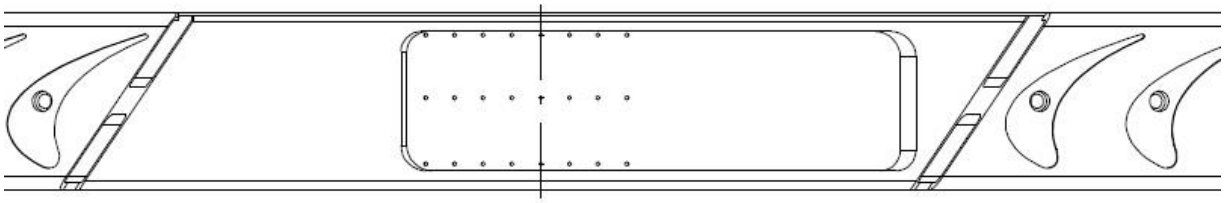

Figure 4.7 Design drawing of the tap position across the interstage labyrinth seal

The main instrumented sector is also equipped with a set of 16 pressure taps distributed at different radial positions in the upstream and downstream sidewalls of the stator disc. The graphic scheme of the pressure tap positions is provided in figure 4.8 where the blue arrow indicates the mainstream direction.

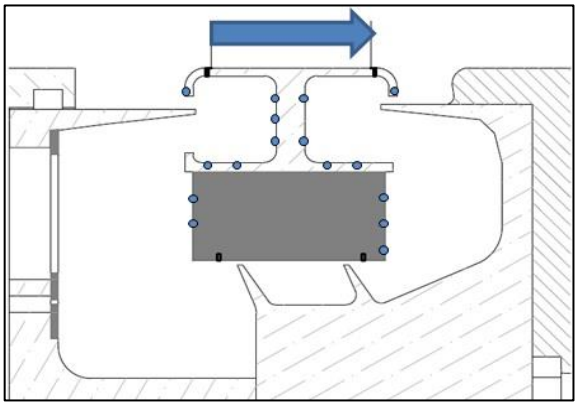

Figure 4.8 Pressure tap distribution on the stator walls (T-bar)

To allow the positioning of the pressure taps within the cavity and to connect them to the pressure transducers, dedicated empty spaces have been obtained into the static part of the cavity. Figure 4.9 shows the slot that corresponds to scheme of figure 4.7. The metallic tubes installed to connect the taps to the transducers can be observed.

Figure 4.9 Empty slot with metal tubes connected to the taps upside of the labyrinth seal

4.2 Air Temperature Distribution

Thermocouples are used to obtain measurement of the air temperature variation inside the cavity due to the mixing process of the seal mass flow with the hotter secondary air stream-tubes. A set of 20 thermocouples are installed into the cavity at different radial and circumferential positions following the scheme of figure 4.10. The position of the thermocouples has been set taking into account the CFD results provided by *GE AvioAero* that supported the design and instrumentation phases of the rig. The distribution of the total temperature is presented in figure 4.11; it shows a larger variation of the total temperature in the upstream region of the cavity just after the secondary air entrance. Therefore, 9 out of 20 probes are distributed in the three direction (axially, radially, and circumferentially) in that region. The pictures in figure 4.12 show the position of the installed thermocouples in the upstream (on the left) and downstream (on the right) cavity space. The thermocouples labeled with #1 and #2, and the ones labeled with #3 and #4, are located at the same radial position but spaced in the circumferential direction. Probes are type T thermocouples with insulated junction (*0.5 mm* diameter). The temperature signals are acquired simultaneously with pressure signals by means of chassis National Instruments Compact DAQ and a NI 9214 terminal for temperature acquisitions. The thermocouples are installed through the empty slots manufactured in the static part of the test section that were used for the pressure tap instrumentation.

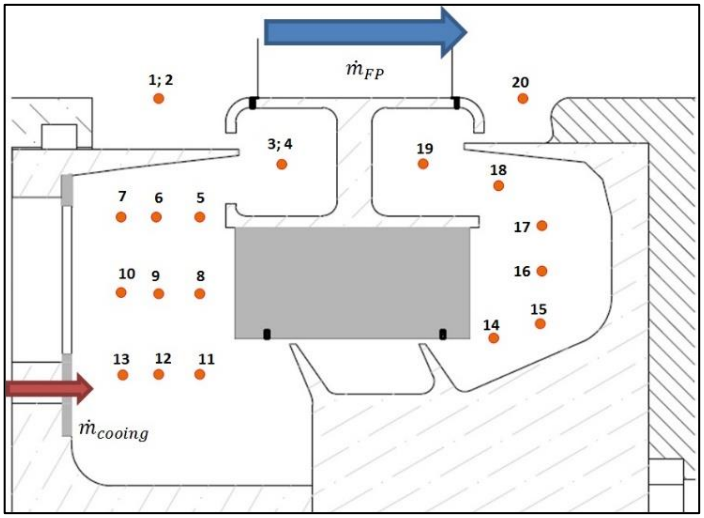

Figure 4.10 Thermocouple distribution

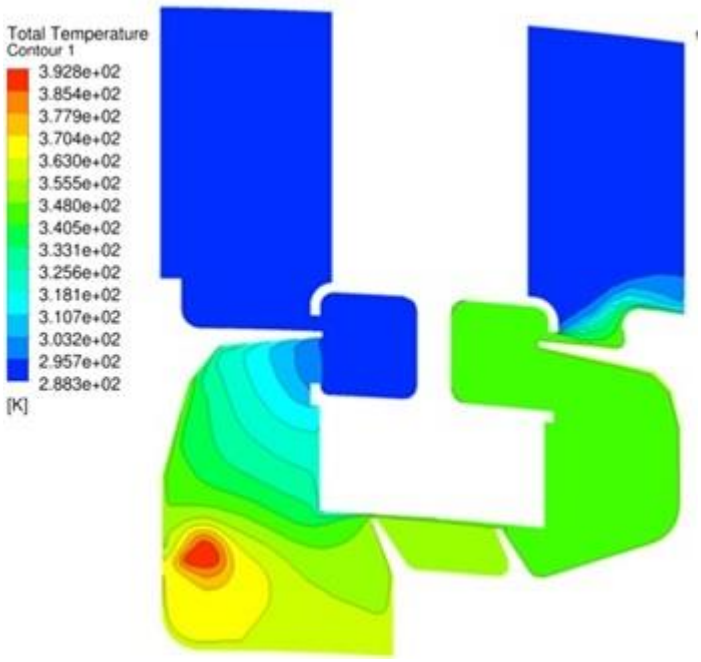

Figure 4.11 CFD results of the total temperature distribution (*GE AvioAero*)

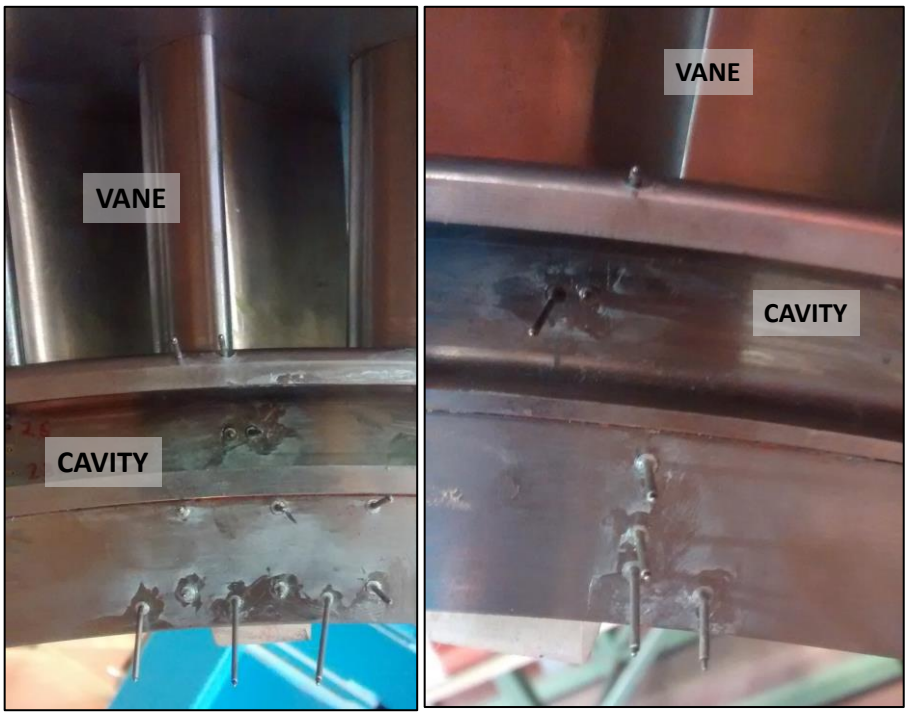

Figure 4.12 Picture of the thermouples installed within the cavity

4.3 Total Pressure Distribution

Measurements of the total pressure distribution are carried out through a kiel probe. Two axial slots have been manufactured in the rig casing to allow introducing the probe within the main annulus. The slots are located 46% of the axial vane chord upstream of the leading edge and at the same distance from the trailing edge, downstream of the row. A two axis traversing system is mounted on the top of the casing to allow performing measurements in both the radial and circumferential directions.

The kiel probe (figure 4.13) is a pneumatic probe useful to measure the time mean total pressure, with a high insensitivity to flow angle variation. The main characteristic of this probe is that the head is surrounded by a cone, working as a shield. This cone is the most important part since it guides the flow towards the head of the probe in order to measure always the total pressure and not a part of it due to a not correct probe alignment with the flow, making the kiel almost insensitive to the angle of attack. The range in which the kiel probe can always measure the total pressure is of $\pm 30°$ with respect to the flow direction.

Figure 4.13 Kiel probe head

4.4 Seal Clearance Measurement

A displacement sensor is located inside the inter-labyrinth seal in order to verify the actual clearance for the different operating conditions. This information is of particular importance when quantifying the inter-stage seal mass flow rate and then the discharge behavior of a contactless sealing system (see section 2.3). A Kaman non-contact eddy current sensor KD 2446 model is adopted. The operative range is up to 2.9 mm and 10 kHz of frequency response. The probe is located within the two seal fins as shown in the cross-sectional scheme portrayed in figure 4.14 on the left. A fillet connection, manufactured within a dedicated vane, allows the positioning of the probe.

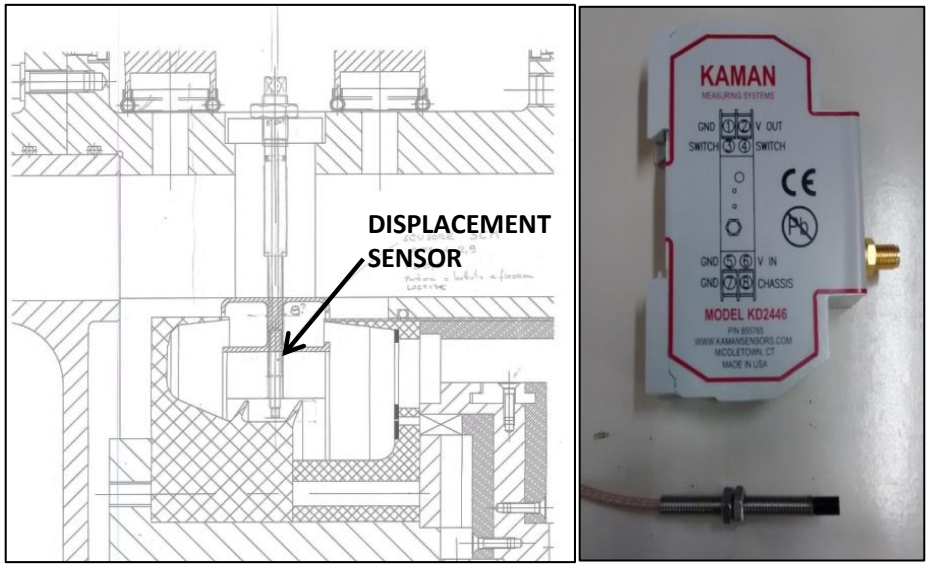

Figure 4.14 Installation scheme of the displacement probe (on the left) and kaman sensor (on the right)

The displacement sensor has been calibrated in loco to avoid any influence of the fins on the measurement. During the calibration, the probe has been put in contact with the down wall and then moved radially acting on the fillet connection. The screw pitch (1 mm) gives the distance of the probe from the solid wall. The calibration has been performed moving the probe up to 2 mm, away from the wall and acquiring the output signal every quarter of round, thus every 0.25 mm. The resulting calibration points are shown in figure 4.15. The best fitting curve of the points provides the relation to use for converting the electric signal into the physical quantity.

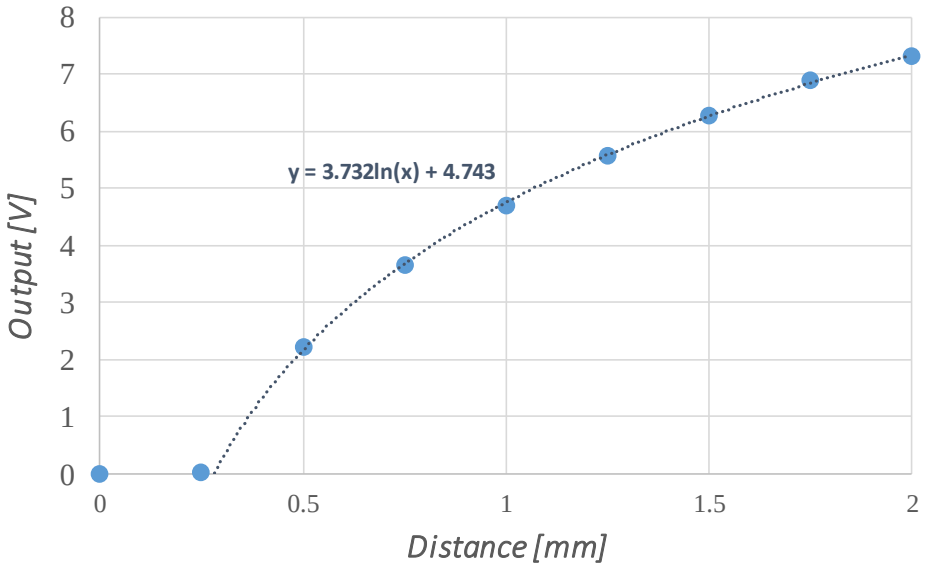

Figure 4.15 Kaman sensor calibration curve

4.5 Calibration Procedure for Leakage Mass Flow Rate Estimation

The measurement of the actual leakage mass flow rate during tests represents the main challenge in evaluating the sealing performances of the cavity. Indeed, since the leakage mass flow rate is expected to be only a small percentage of the main annulus mass flow rate, then a direct measurement of this quantity is not possible to be performed with a reasonable error. Therefore, a calibration procedure of the cavity has been setup specifically for the test rig.

The calibration tests have been performed with a "*locked vane path*" configuration of the rig. The vane channel is locked together with the secondary air paths, leaving only the rim seal clearance open to the flow passage. A system constituted by a venturi-meter and a settling chamber is mounted at the rig inlet. The settling chamber has the purpose of making the flow uniform at the rig inlet. In this configuration, the entire mass flow measured by the venturi-meter at the rig entrance is forced to pass across the labyrinth seal. Moreover, the pressure signal from each series of taps across the seal fins is physically averaged by connecting all the taps together in order to measure a representative pressure value of the flow across each of the labyrinth seal. To this end, we indicate the pressure measured in the front position with p_F, p_C is the pressure measured between the two fins and p_R is the one measured downstream of the seal.

The cross-sectional view of the test section during calibration is provided in figure 4.16. Furthermore, figure 4.17 shows a picture of the rig arrangement during calibration where the venturi-meter and the settling chamber at the rig inlet are visible.

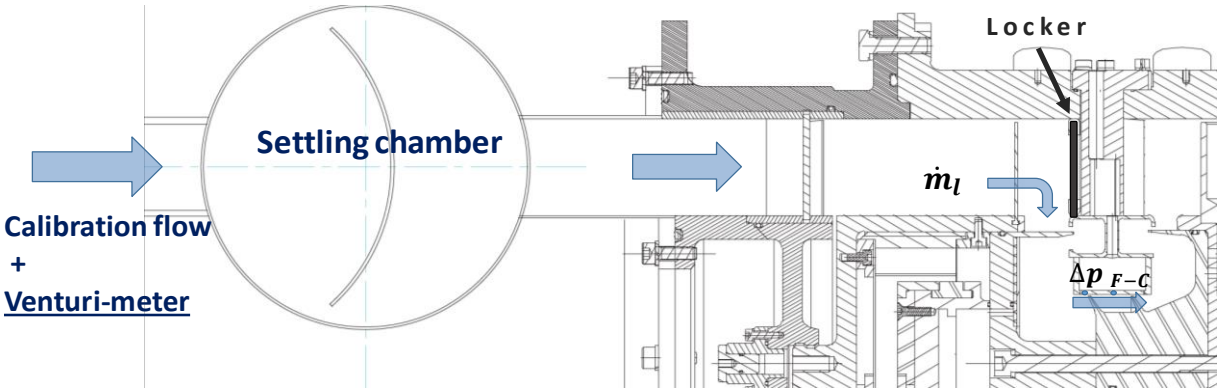

Figure 4.16 Cross-sectional view of the test section during calibration

Figure 4.17 Rig arrangment during calibration

Once the rotational speed, hence the swirl factor, is set, several leakage mass flow rates are imposed. Then the pressure drop induced by the leakage flow across the first fin of the labyrinth seal is measured, i.e. $\Delta p_{F-C} = p_F - p_C$. The measurement is extended to different operating conditions so that the set of data collected allow generating calibration curves of the type:

$$\dot{m}_l = f(\Delta p_{F-C}, S_w). \tag{4.01}$$

During the "real" tests, hence tests performed with the vane channel open, the pressure drop across the fin (Δp_{F-C}) is measured and used, for each swirl factor, to extract the mass flow rate value from the aforementioned calibration curves. The measurement error in evaluating the leakage mass flow rate is estimated to be within the 5% of the measured value.

4.5.1 Calibration test results

Calibration tests have been performed in a range of five different swirl factors and five leakage mass flow rates. Table 4.1 summarizes the calibration test conditions. In this way a set of 25 calibration data points have been collected. The values $\dot{m}_l$ have been decided in order to produce pressure drops Δp_{F-C} consistent with the ones expected in real tests at the same swirl factors and for Reynolds numbers from 100000 to 200000. In addition, stationary tests with $\Omega = 0$, thus $S_w = \infty$, have been conducted in order to provide the leakage mass flow rate without rotation, $\dot{m}_{l,0}$.

S_w	[-]	0.56	0.62	0.7	0.8	0.93
$\dot{m}_l$	[kg/s]	0.084	0.103	0.124	0.145	0.166

Table 4.1 Calibration test matrix

Figure 4.18 provides the main results of the calibration tests. The plot shows the leakage mass flow rate ($\dot{m}_l$) measured for each swirl factor as a function of the pressure drop Δp_{F-C}. The best fitting curve for the case $S_w = 0.7$ has been added to the plot. It can be observed that the leakage mass flow rate is related to the square root of Δp_{F-C}, as expected. On the other hand, the effect of the rotational speed on the dimensional leakage flow rate values appear almost negligible.

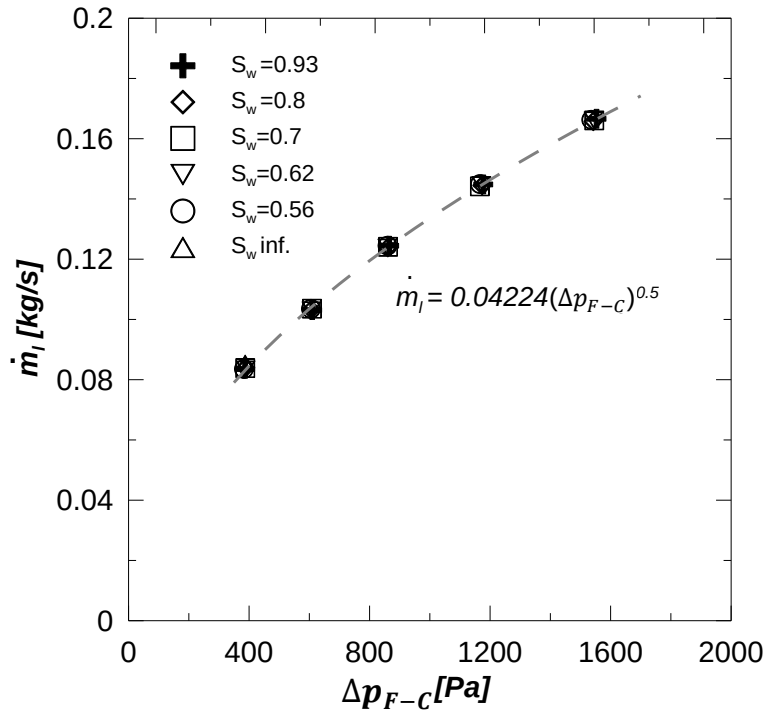

Figure 4.18 Calibration test results

4.5.2 Validation of the calibration procedure

In order to support the ability of the proposed procedure in linking the pressure drop measured during the tests and the calibration phase, a comparison of the static pressure distributions measured along the static surface of the cavity is provided in figure 4.19. Results refer to calibration and real tests. The operating conditions have been set in order to reproduce the same swirl factor and the same pressure drop of the leakage flow across the first labyrinth fin (i.e. $S_w = 0.7$ and $\Delta p = 380 Pa$). For the real test, the operating condition corresponds to a mainstream Reynolds number of 100000.

The pressure values are made non-dimensional by the pressure difference between taps *8* and *9* (located just upstream and downstream of the labyrinth seal fins). Results show that through the upstream cavity the pressure distribution keeps extremely similar in both conditions. A limited scatter of data is observed downstream of that labyrinth seal. This confirms that the flow behavior in the cavity during the normal operation is consistent with the development reproduced during the calibration phase, where the main flow expanding into the vane row is not present. This makes evident that the two data sets can be combined together in order to provide an accurate estimation of the mass flow-pressure drop dependence.

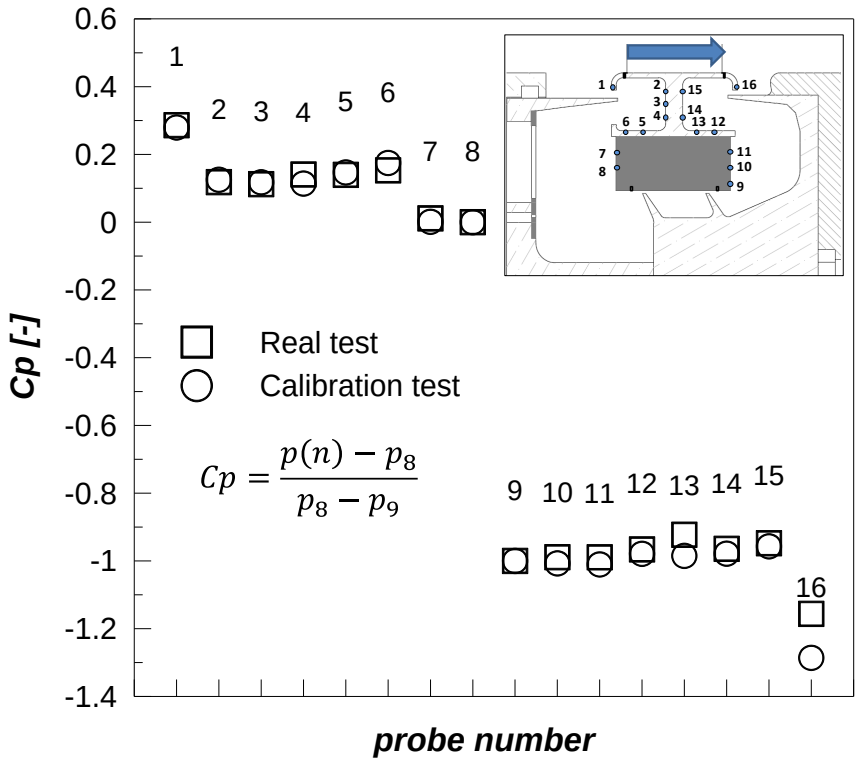

Figure 4.19 Comparison between the static pressure distribution along the cavity during tests in statndard rig and calibration configuration (S_w=0.7, Re=100000)

Chapter 5 - EXPERIMENTAL RESULTS

The experimental campaign has been carried out at low speed condition involving a largely subsonic flow. The isentropic Mach number, evaluated downstream of the vane, reaches the maximum value of $Ma = 0.2$ during tests. Consequently, operating conditions are identified through the Reynolds number and the swirl factor only. The isentropic Reynolds number is monitored by measuring the pressure drop across the vane using the pressure tap series located at the tip whereas the swirl factor is set by imposing the rotational speed to the rotor. The axial velocity, derived from the vane pressure drop, has been also used to estimate the main annulus mass flow rate. Finally, the coolant flow rate is measured by means of a venturi-meter installed at the inlet of the dedicated driving fan. The results are grouped into four blocks depending on their specific objective:

1. Characterization of the mainstream and cavity aerodynamics;
2. Estimation of the cavity discharge coefficient;
3. Investigation of the coolant related effects on the cavity aerodynamics;
4. Measurements of the mainstream total pressure distributions;

Point one is aimed at characterizing the working fluid flowing in the main annulus and the cavity. Measurements of the static pressure distributions have been performed in different sectors in order to verify the operating axial-symmetry of the rig. In addition, the impact of different rotational speeds has been investigated in these early tests.

For what concern the second point, calibration test results have been adopted to measure the leakage mass flow rate through the cavity for a wide range of Reynolds numbers and swirl factors. Then, the computation of the discharge coefficient allows the quantification of the viscous and rotational effects on the sealing effectiveness of the cavity. Two definitions for the C_D have been proposed with the aim of comparing the present results with literature data obtained in simplified configurations, as well as to provide a useful tool to be adopted in the preliminary design phase of the engine.

In the point three, the influence of several coolant flow rates is investigated. Pressure signals acquired into the cavity provide a direct measure of the pressurization level of the cavity, as well as the analysis of the effect induced by the coolant on the pressure drop provoked by the teeth. These latter measurements are adopted to evaluate the leakage mass flow rate and then the discharge coefficient. Moreover, the computation of the mass flow rate ingested from the mainstream provides an estimation of the minimum amount of coolant necessary to seal the cavity.

The last point is dedicated to the measurement of the total pressure distributions of the flow upstream and downstream of the vane, for a fixed Reynolds number but different swirl factors and coolant flow rates. These data give insights on the interaction mechanism between the cavity and the main annulus flows. Particularly, a strong modification of the secondary flow structures through the vane is observed for all the different tested conditions.

5.1 Aerodynamic Characterization of the Mainstream and Cavity Flows

The first tests have been carried out at constant Reynolds number (*Re=100000)* while the rotational speed has been modified in order to investigate three different swirl factors. The secondary air paths have been locked so that no additional flows have been considered during this early tests. The test matrix is presented in table 5.1. Results of the main flow properties in terms of the static pressure distributions are presented in order to give the boundary conditions imposed to the cavity. Subsequently, the static pressure distribution measured within the cavity, are shown.

$Re = 100000,\ \dot{m}_c/\dot{m}_{FP} = 0$			
S_w [-]	0.56	0.7	0.93

Table 5.1 Test conditions

5.1.1 Circumferential static pressure distribution

The measurements of the circumferential static pressure distribution have been carried out upstream and downstream of the vane hub and tip sections in the three instrumented sectors. The results are shown in figure 5.1 to figure 5.7 in terms of the non-dimensional static pressure coefficient C_p against the non-dimensional pitch-wise length y/g. The C_p is defined as follows:

$$C_p = \frac{p(y/g) - p_{amb}}{\Delta p_{vane}} \tag{5.01}$$

where $p(y/g)$ is the local static pressure, Δp_{vane} is the pressure drop across the vane row that, for a fixed operating Reynolds number, is kept constant.

Figure 5.1 and figure 5.2 show the results for the tip and hub positions, respectively, in correspondence of the three instrumented sectors and $S_w = 0.7$. The higher values in the plots correspond to the distributions measured at the vane leading edge (*L.E.*), while the lower ones are measured at the trailing edge of the vane (*T.E.*). The pressure drop that can be observed from the leading edge to the trailing edge of the vane is due to the expansion ratio of the flow across the vane. Moreover, the pressure drop measured at the hub results higher than the one measured at the tip. The distributions assume a sinuous-like form and are almost identical for the three sectors. This suggests a good axial symmetry of the flow developing inside the rig. Also, both hub and tip distributions appear rather similar. Relative peaks of the static pressure distribution are located at $y/g = 0.16$. They are due to potential effects of the vane trailing and leading edges in the upstream and downstream positions, respectively (see figure 4.6 for identifying tap position).

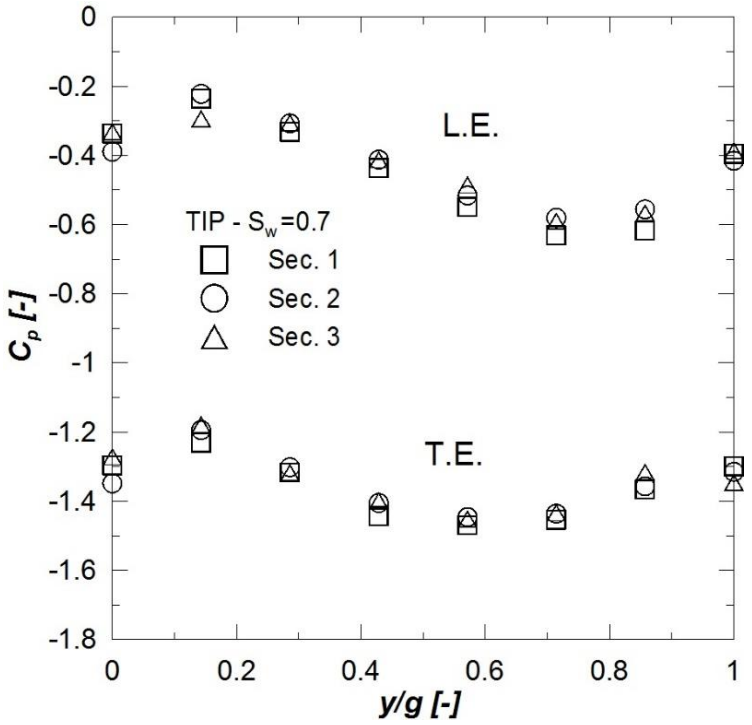

Figure 5.1 Circumferential static pressure distributions at the vane tip (inlet and outlet sections) measured in the three instrumented sectors

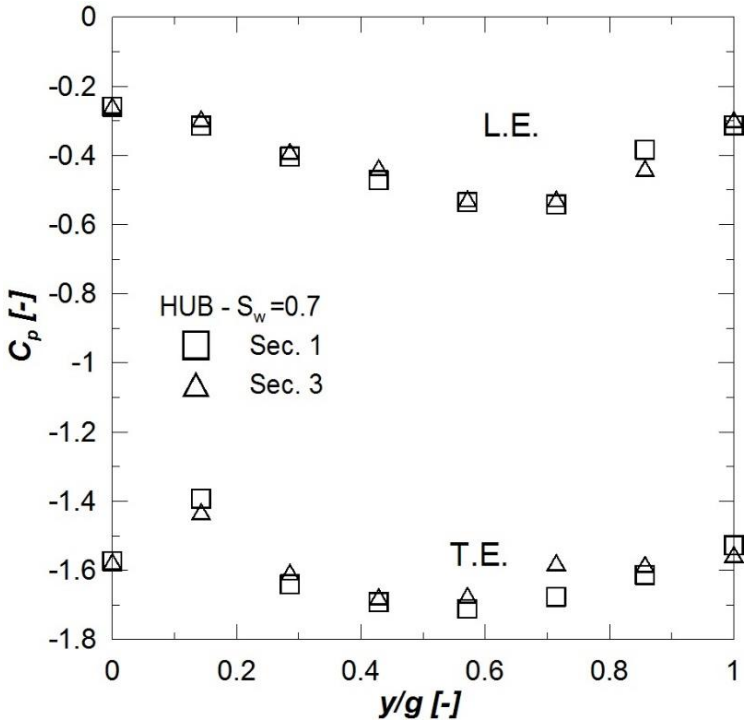

Figure 5.2 Circumferential static pressure distributions at the vane hub (inlet and outlet sections) measured in two instrumented sectors

Figures from 5.3 to 5.5 show the effect of the swirl factor variation on the pressure distribution in the different sectors at the tip section of the vane. Figures 5.6 and 5.7 show the analogous quantities measured at the hub section. The plots make evident that the static pressure distributions are not affected by the rotational regime of the rig neither at the tip, nor at the hub.

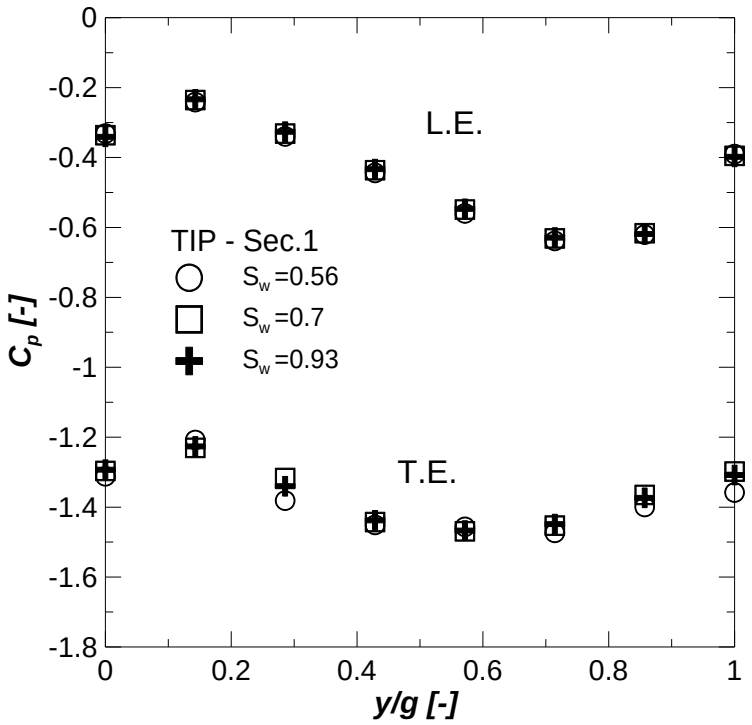

Figure 5.3 Effect of the swirl factor on the circumferential static pressure distributions at the vane tip: Sector 1

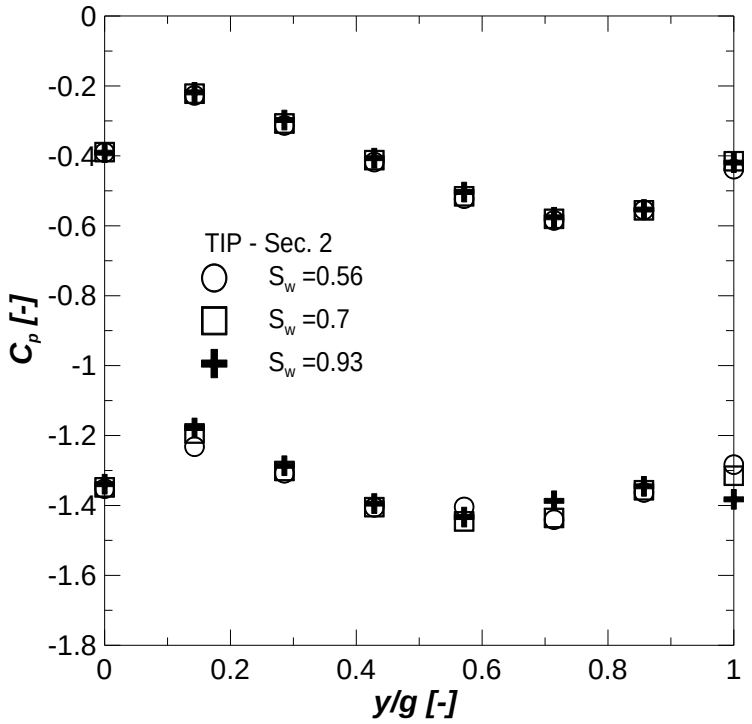

Figure 5.4 Effect of the swirl factor on the circumferential static pressure distributions at the vane tip: Sector 2

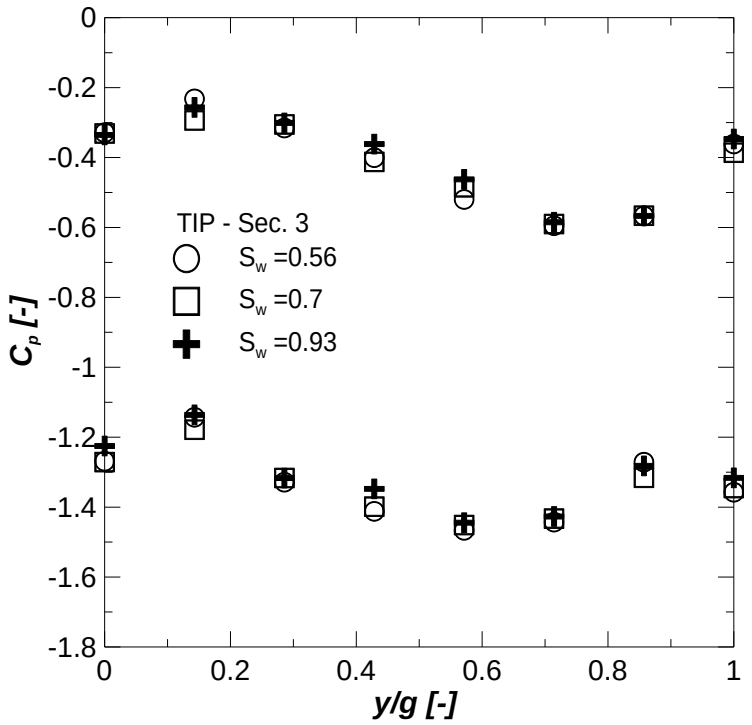

Figure 5.5 Effect of the swirl factor on the circumferential static pressure distributions at the vane tip: Sector 3

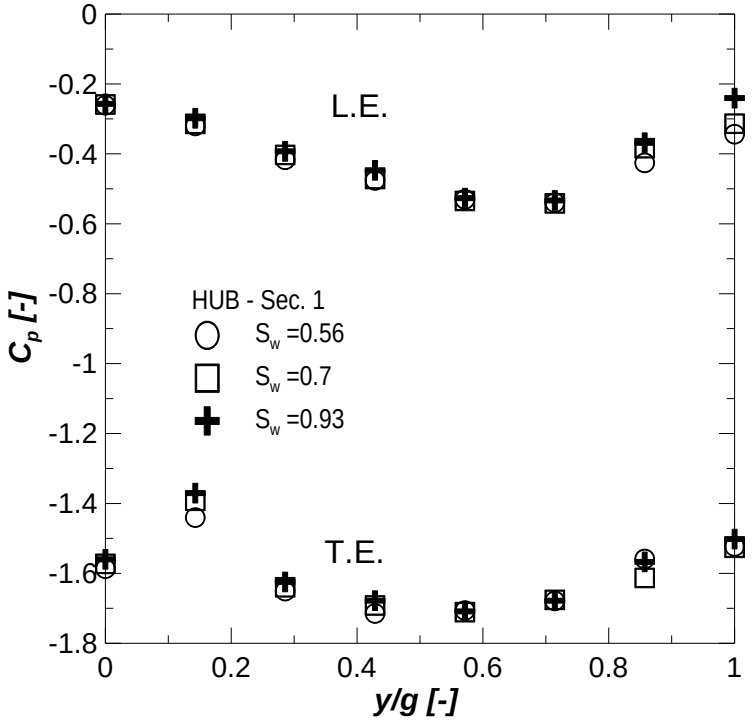

Figure 5.6 Effect of the swirl factor on the circumferential static pressure distributions at the vane hub: Sector 1

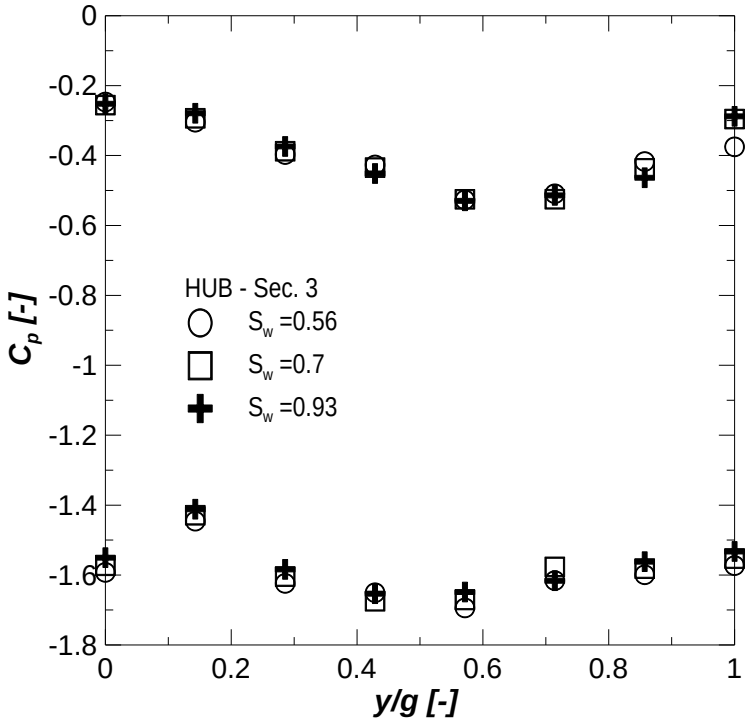

Figure 5.7 Effect of the swirl factor on the circumferential static pressure distributions at the vane hub: Sector 3

5.1.2 Vane loading distribution

The aerodynamic loading distributions are presented in figures from 5.8 to 5.10 for the three span heights. The static pressure coefficient is plotted against the non-dimensional axial chord length z/C_z, where C_z is the axial chord of the vane. The static pressure coefficient for the vane loading distribution is defined as follows:

$$C_p = \frac{\overline{p_{t,1}}(r) - p(z/C_z)}{\overline{p_{t,1}}(r) - p(z = C_z)} \tag{5.02}$$

where $\overline{p_{t,1}}(r)$ is the pitchwise averaged total pressure measured at the vane inlet plane using a kiel probe; $p(z = C_z)$ is the outlet static pressure. Both quantities have been obtained in correspondence of the spanwise position where the vane loading is measured.

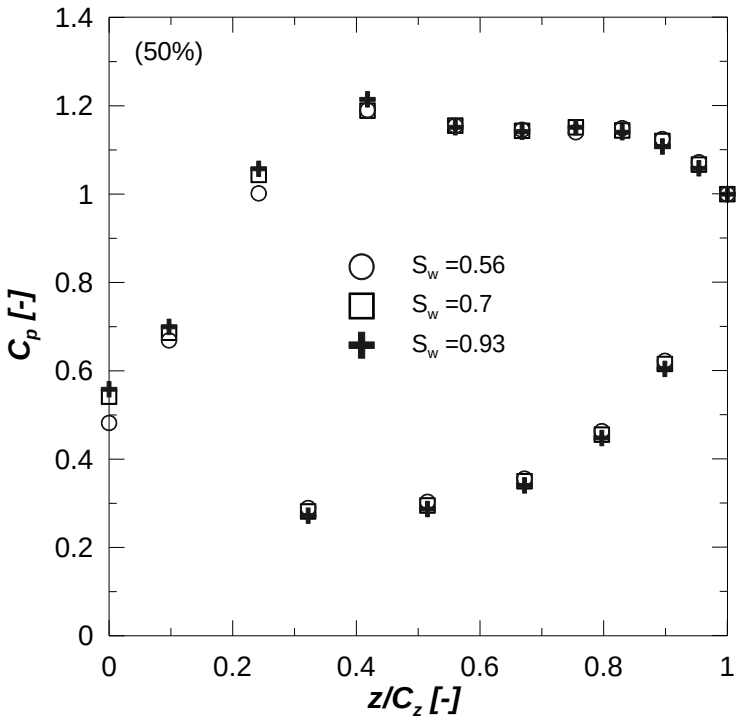

Figure 5.8 Effect of the swirl factor on the vane aerodynamic loading at midspan

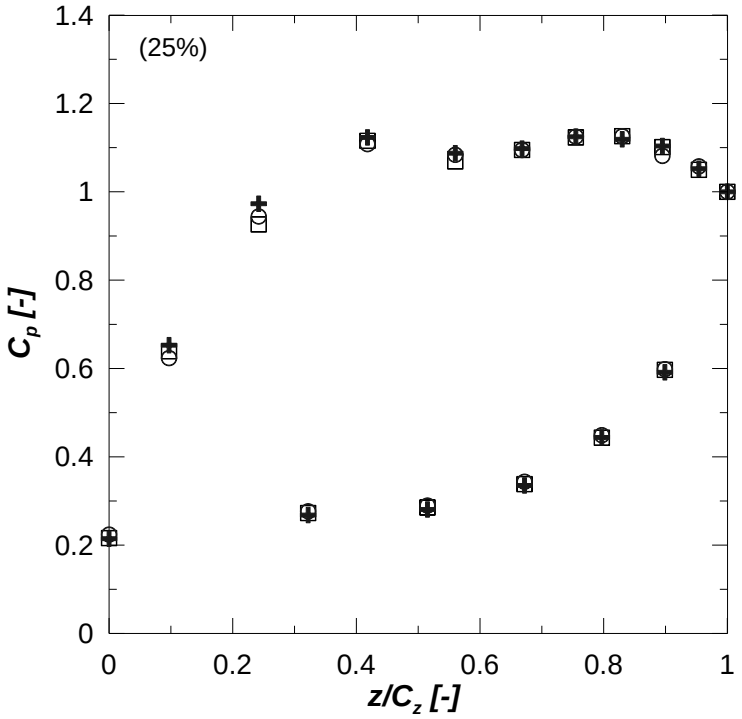

Figure 5.9 Effect of the swirl factor on the vane aerodynamic loading at 25% of the span

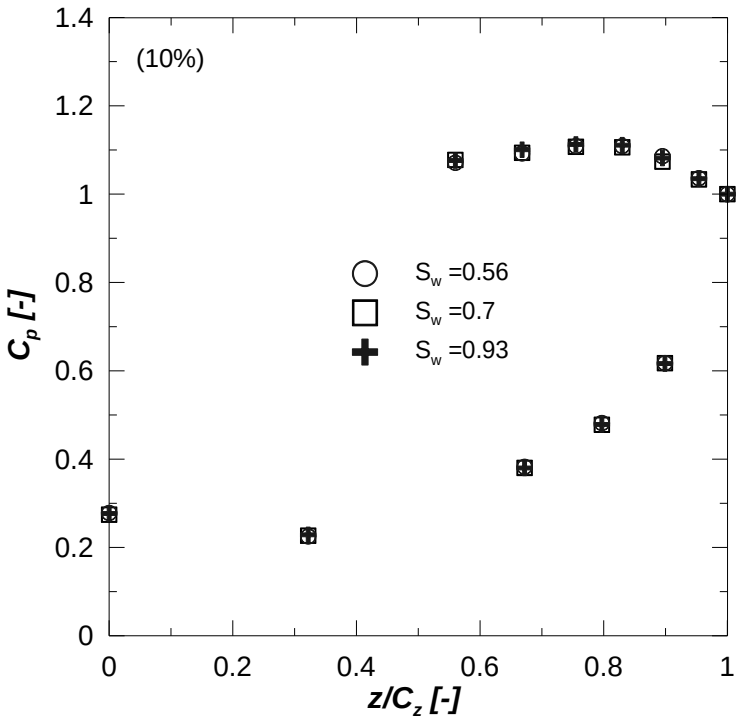

Figure 5.10 Effect of the swirl factor on the vane aerodynamic loading at 10% of the span

The location of the peak value of the pressure coefficient, which corresponds to the location of maximum velocity, is around $x/C_z = 0.42$ and keeps identical for the three spanwise sections. The peak value of the pressure coefficient is maximum at midspan where $C_{p,peak} = 1.18$, and is lower at the 25% section where $C_{p,peak} = 1.11$. Unlikely, the first three static pressure taps on the suction side of the vane instrumented at the 10% of span height resulted not available for measurements. Therefore, only a partial view of the profile loading in this section is given. However, the pressure coefficient in the rear part of the suction keeps similar to the one measured at the higher sections, while values on the pressure side are lower.

Modifications of the rotational speed appear to affect only marginally the fore part of the aerodynamic loading distribution. Indeed, the vane loading increases as the swirl factor reduces, while the peak value of the pressure coefficient keeps constant in each section. The rear part of the suction side and the entire pressure side of the vane are practically uninfluenced by the swirl factor variation.

5.1.3 Cavity static pressure distribution

The static pressure distribution along the static part of the cavity ("T-bar") is presented in figure 5.11 for the three different swirl factors. The pressure measured in each tap position $p(n)$ is made non-dimensional by the pressure drop across the vane similarly to definition (5.01), so that:

$$C_p = \frac{p(n) - p_{amb}}{\Delta p_{vane}} \tag{5.03}$$

The data show a first pressure drop between the first and the second pressure tap, due to the flow lamination induced by the horizontal tooth. Moving along the cavity surface, pressure is almost constant up to tap n°6, while a larger pressure drop is observed between positions *8* and *9*. This is provoked by the labyrinth seal system, effectively inducing the largest pressure drop into the flow. In the rear cavity, the pressure keeps almost constant from tap n°9 to n°14. Finally, the pressure drop between position 15 and 16 is due to the flow passing through the horizontal teeth located in the downstream rim seal.

The modification of the operating swirl factor does not affect the static pressure of the flow in the fore part of the cavity. On the other side, a major data scatter characterizes the measurements downstream of the labyrinth seal at different operating rotational speeds. However, also in this part of the cavity the pressure keeps almost constant up to the tap 15, prior to readjust to the imposed exit pressure at the tap n°16.

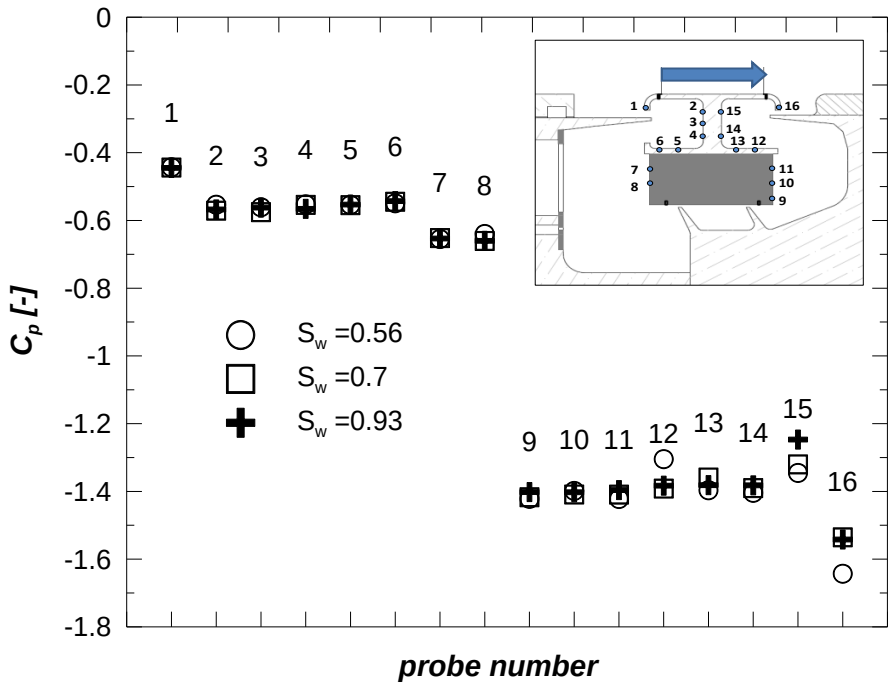

Figure 5.11 Cavity T-bar static pressure distributions

Results describing the circumferential pressure distribution in the fore and rear part of the labyrinth seal are shown in the following figures. The top right scheme in figure 5.12 helps to understand the probe position where F indicates the front taps, R the rear series and C the one between the two fins. This kind of measurements is of great importance, since they allow us to verify the circumferential variation of the pressure drop induced by the teeth on the leakage flow. Results are reported in terms of the static pressure coefficient C_p (see definition 5.01) against the non-dimensional pitch-wise length y/g.

Figure 5.12 shows the circumferential distributions in the three sectors for constant $S_w = 0.7$, upstream (larger data into the plot) and downstream of the labyrinth fins (smaller data into the plot). The differences between the two measured levels directly quantify the pressure drop due to the flow passing across the two labyrinth fins. Results clearly show that data are completely overlapped in the three sectors, thus again indicating that the flow is strongly uniform in the circumferential direction, and lamination occurs with the same strength in the overall annulus. This will also emphasize the opportunity to account for this pressure drop as a robust signal to be related with the leakage mass flow rate in calibration tests.

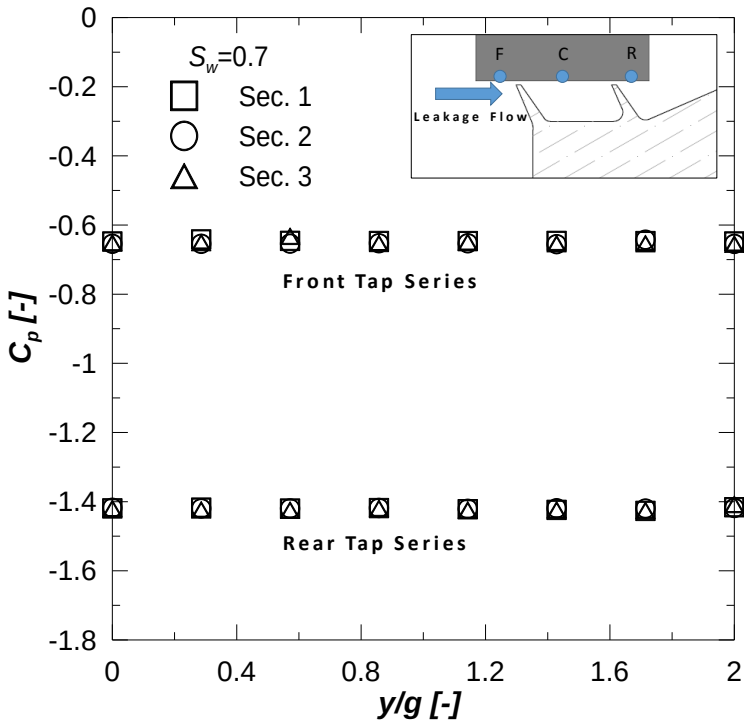

Figure 5.12 Circumferential static pressure distribution at the labyrinth seal inlet and outlet positions in the three instrumented sectors

Figures from 5.13 to 5.15 show the swirl factor variation effects on the circumferential distribution of the pressure coefficient in the three sectors. The data in these plots clearly show that no significant modification of the pressure distribution can be observed as the swirl factor varies. Indeed, the pressure values keep uniform in the circumferential direction for all the test conditions and in all the three sectors.

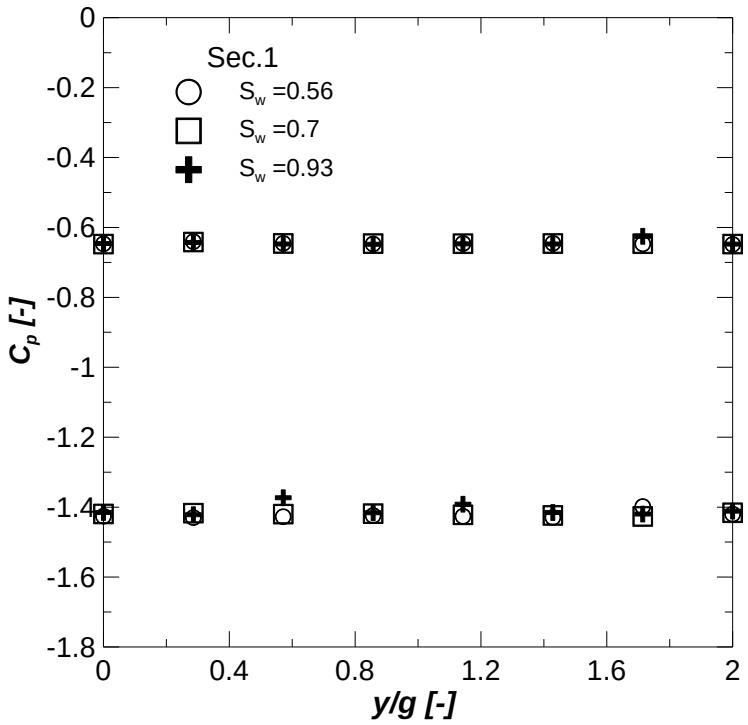

Figure 5.13 Effect of the swirl factor on the seal inlet and outlet pressure: sector 1

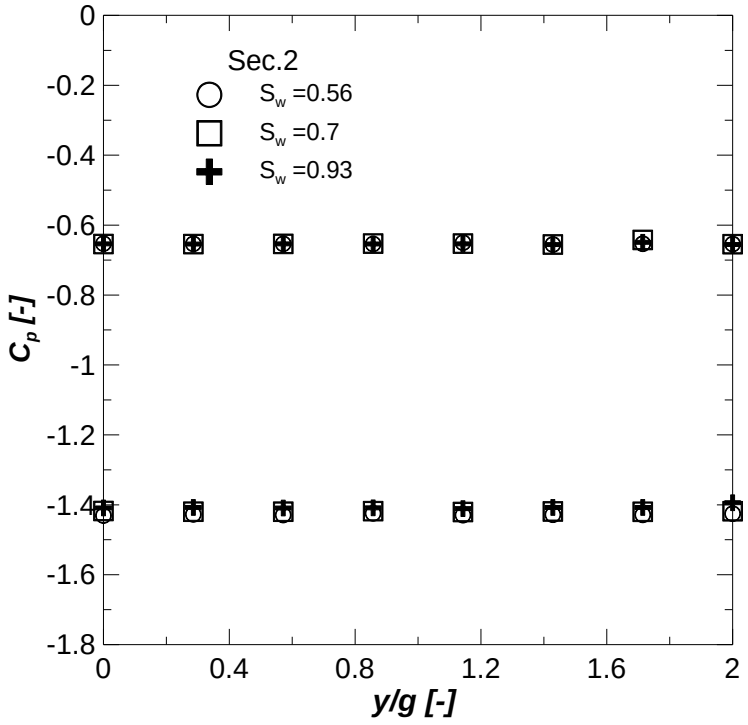

Figure 5.14 Effect of the swirl factor on the seal inlet and outlet pressure: sector 2

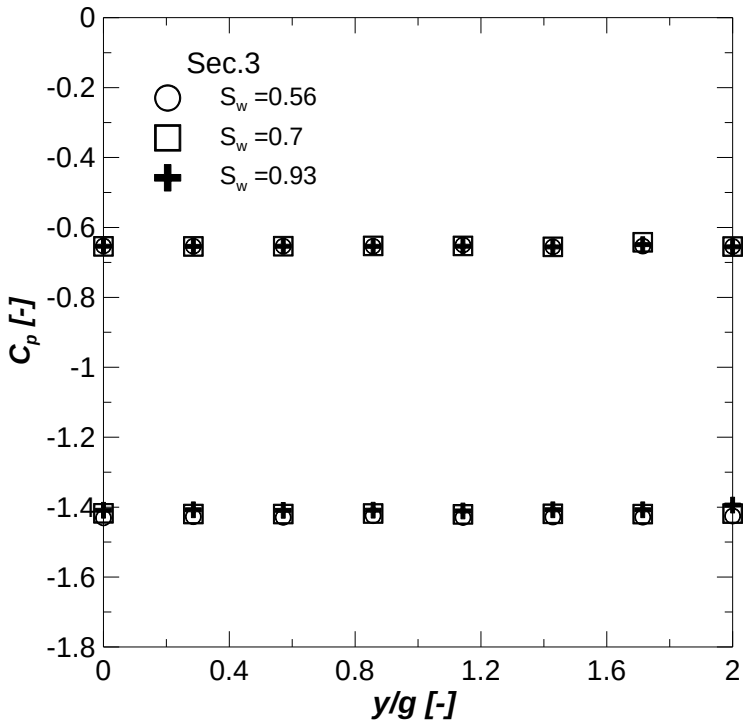

Figure 5.15 Effect of the swirl factor on the seal inlet and outlet pressure: sector 3

The strong axialsymmetry of the pressure across the labyrinth seal allows considering a single reference value for each position. As already mentioned in the description of the calibration procedure (section 4.5), the pressure signal has been averaged over the circumferential direction for each of the three tap series and over the three sectors. Hence, p_F is the pressure measured in the front position, p_C is the pressure measured between the two fins and p_R is the one measured downstream of the seal.

Table 5.2 reports the pressure drops of the flow across each of the two fins, hence $p_F - p_C$ and $p_C - p_R$, as a percentage of the overall pressure drop $\Delta p_{F-R} = p_F - p_R$. The major reduction of the static pressure is caused by the passage across the first fin, which constitutes around 85% of the overall pressure drop. This value is observed to slightly decrease with smaller rotational speed, thus with increasing swirl factors, hence the drop related to the second fin increases.

Re [-]	S_w [-]	$(p_F - p_C)/\Delta p_{F-R}$	$(p_C - p_R)/\Delta p_{F-R}$
100000	0.56	85.9%	14.1%
	0.7	85.2%	14.8%
	0.93	83.3%	16.7%

Table 5.2 Pressure drop across each labyrinth seal fin

5.2 Discharge Coefficient Estimation

The evaluation of the discharge coefficient describing the sealing performances of the cavity, has been performed for a series of 25 test conditions. They are constituted by five different Reynolds numbers and five different swirl factors, which are indicated in table 5.3. Additional stationary tests performed with $\Omega = 0$, thus $S_w = \infty$, provides the discharge coefficient in stationary conditions ($C_{D,0}$). All the results have been obtained without additional coolant.

Re [-]	100000	125000	150000	175000	200000
S_w [-]	0.56	0.62	0.7	0.8	0.93

Table 5.3 Test conditions

During tests, the reference pressures of the fluid across the labyrinth seal fins (namely p_F, p_C and p_R) have been measured. The pressure drop across the first fin has been adopted to determine the leakage mass flow rate using the calibration curves that are provided in section 4.5. The boundary conditions of the cavity flow, such as the total pressure at midspan of the vane inlet plane and the static pressure across the vane, have been measured. Moreover, the measurement of the actual seal clearance is carried out to correctly evaluate the passage area of the flow across the labyrinth seal.

The discharge coefficient C_D of a labyrinth seal for subcritical pressure ratios is defined in section 2.3 as the ratio between the real and the ideal leakage mass flow rates. The ideal mass flow ($\dot{m}_{id}$) is that flowing through an ideal nozzle with the same pressure ratio and cross-sectional area of the gap of the labyrinth seal, so that:

$$C_D = \frac{\dot{m}_l}{\dot{m}_{id}} \tag{5.04}$$

$$\dot{m}_{id} = \frac{p_t A}{\sqrt{T_t}} \sqrt{\frac{2k}{R_{gas}(k-1)} \left[1 - \left(\frac{1}{\beta}\right)^{\frac{k-1}{k}} \right]} \left(\frac{1}{\beta}\right)^{\frac{1}{k}} \tag{5.05}$$

The leakage mass flow rate is determined entering calibration curves of section 4.5 with the value of Δp_{F-C}. The ratio between the leakage and main annulus mass flow rate keeps constant for all the test condition with $\dot{m}_c/\dot{m}_{FP} = 2.78\%$. The relative error in evaluating the discharge coefficient is considered to be lower than 10%.

The cross-sectional area (A) across the labyrinth seal fin, has been obtained, for the different operating conditions, by averaging the clearance-meter signal. The ratio between the actual passage area and the design value (A_0) is plotted in figure 5.16 against the rotational speed Ω. As expected, the actual seal clearance reduces during tests due to centrifugal forces acting on the rotor disk. The maximum area reduction is almost 3% of the design value, and occurs at the highest rotational speed ($\Omega = 750\, rpm$). The area variation observed with the swirl factor is due to the elastic hysteresis of the disc.

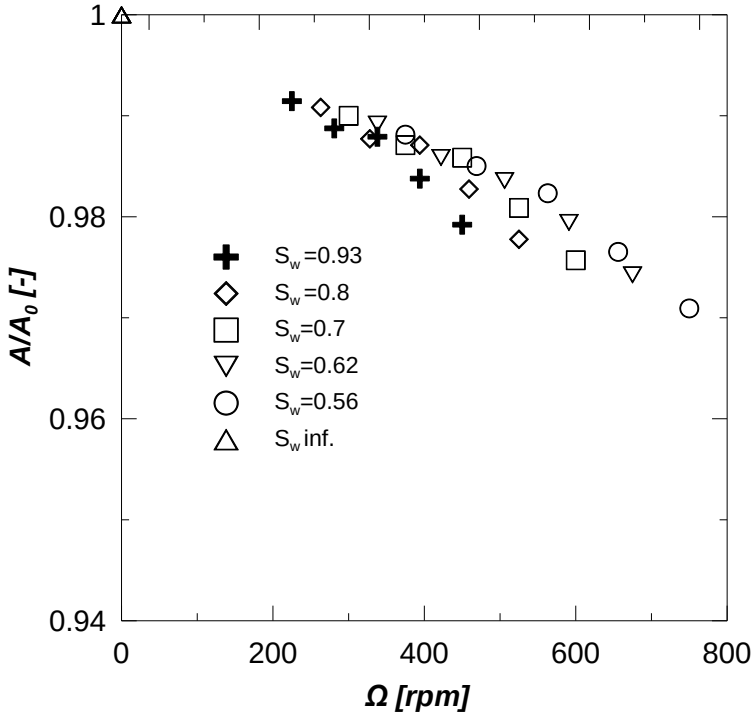

Figure 5.16 Leakage flow passage area during tests

Once collected all the data, the discharge coefficient has been calculated following equations (5.04) and (5.05). Two different definitions of the expansion ratio appearing in equation (5.05) have been used, providing two different C_D charts. The first definition allows the comparison of the current measured C_D with literature data concerning the discharge coefficient of labyrinth seals only (hence where the vane is not present). A second definition has been introduced in order to provide a tool useful for designers to define the sealing performances of the cavity during the preliminary design phase of engines.

For the comparison with literature data, the total to static pressure ratio (β) is evaluated as the ratio between the static pressure of the fluid before the first labyrinth fin, hence p_R, plus the dynamic term related to the axial velocity (which gives the inlet total pressure p_t), and the static pressure downstream of the labyrinth seal (p_R). It represents the "effective pressure ratio" (β_{eff}) introduced in section 2.3 for labyrinth seals with preswirled inlet flow:

$$p_t = p_F + \frac{1}{2}\rho\left(\frac{\dot{m}_l}{\rho A}\right)^2 \tag{5.06}$$

$$\beta_{eff} = \frac{p_t}{p_R} \tag{5.07}$$

Results are shown in figure 5.17 where the C_D is plotted against the Reynolds number for each swirl factor. In addition, the stationary value derived from the test case without rotation ($C_{D,0}$) is added to the plot. The discharge coefficient rises with the Reynolds number in both the stationary and the rotating cases from around 0.475, to almost $C_D = 0.5$ at the highest Reynolds number. Values appear similar to the one shown in open literature for similar test conditions (see *Zimmermann and Wolff (1998), Waschka et al. 1992*). Particularly, measured values of the C_D are similar to the one assumed in *Coren et al. (2011)* for a three fins straight through labyrinth seal employed in their test rig, which is $C_D = 0.48$. This further confirm the ability of the calibration procedure to estimate the discharge coefficient in aeroengine-like cavity operating under realistic conditions.

The disk rotation appears only to marginally reduce the discharge coefficient with respect to the stationary case as predicted by *Waschka et al. (1992)* and *Witting, et al. (1992)*, since in the present tests, the ratio between the axial velocity of the fluid at the fins and the rotor circumferential velocity ($v_{z,l}/\Omega R$) resulted largely lower than the unity. The effects of the variation of the swirl factor appear confined to the smaller Reynolds numbers, as made evident by the plot, while they become negligible at the higher Reynolds number conditions. This

behavior is consistent with the results of *Waschka, et al. (1992)* for a straight-through labyrinth configuration, reported in figure 2.13.

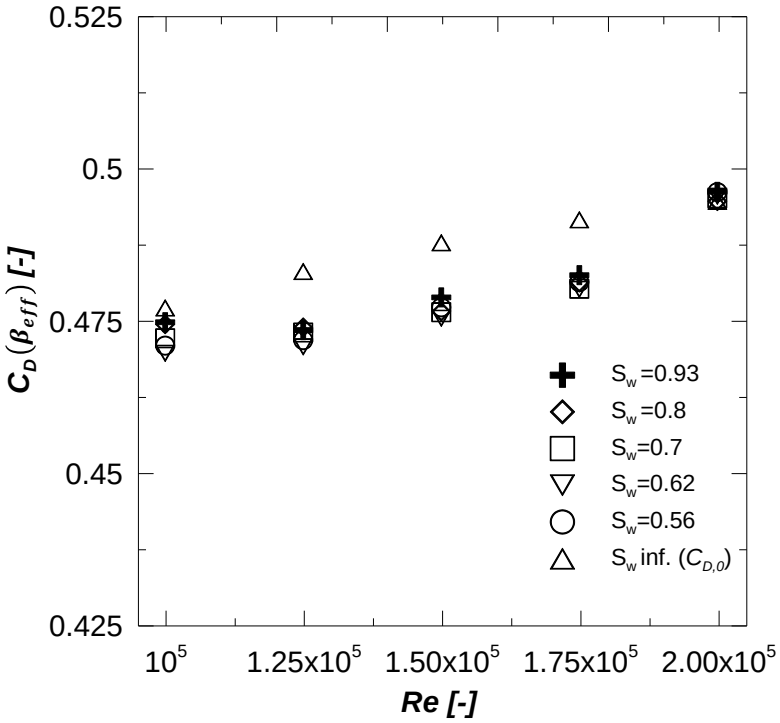

Figure 5.17 Influence of the Reynolds number and the swirl factor on the discharge coefficient

The second definition of the discharge coefficient is based on data characterizing the vane expansion ratio. It adopts the ratio between the total pressure of the main flow measured at midspan upstream of the vane and the static pressure measured at the hub downstream of the vane to compute the pressure ratio (β_{FP}). This definition directly links the flow properties through the vane, which represent design parameters of the stage, to the discharge behavior of the cavity system.

The new values are plotted in figure 5.18 against the Reynolds number for different swirl factors. They show slightly lower values than the ones plotted in the previous figure. Indeed, the new definition accounts for a higher inlet total pressure that leads to a higher ideal mass flow rate. Values keep rising with the Reynolds number and the appear only barely effected by the swirl factor for each Reynolds number. This results provide a different scenario with respect to the results provided in the previous figures or the ones available in literature for simplified test sections.

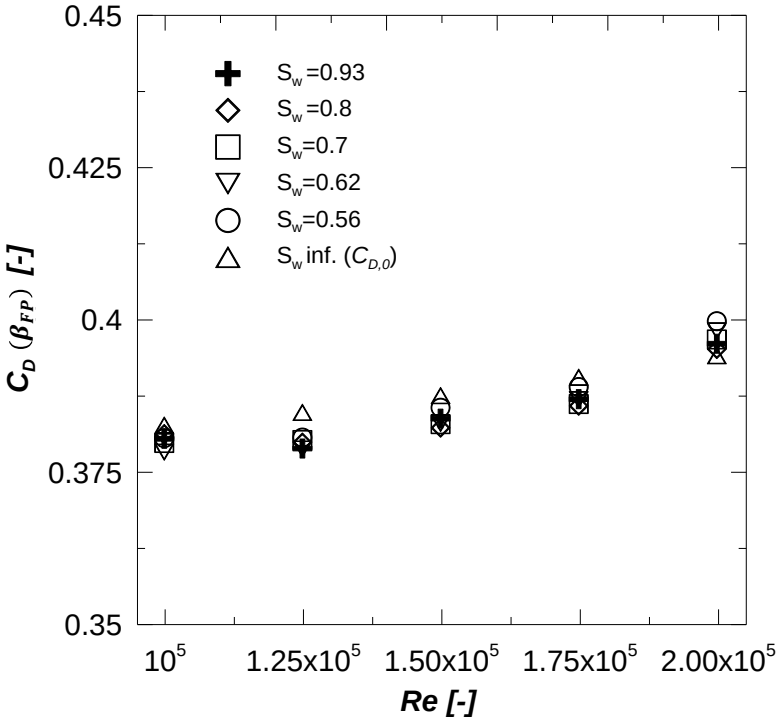

Figure 5.18 Influence of the Reynolds number and the swirl factor on the discharge coefficient defined using design parameters

5.3 Effect of the Coolant Flow Rate

The effects of the coolant on the cavity aerodynamics has been investigated by delivering several amounts of fluid into the cavity through the dedicated secondary air line (#1 in figure 3.4). A cold flow is considered. Figure 5.19 provides a schematic representation of the flows, and the related terminology involved in this analysis. The coolant flow is delivered axially into the fore cavity through the bottom side wall of the rotor (red arrow). The rim seal flow ($\dot{m}_{rim}$) represents the time averaged amount of fluid that passes through the upstream rim clearance (orange arrow).

The operating conditions of the external flow have been kept constant and corresponding to $Re = 100000$ and $S_w = 0.7$. The coolant flow rate has been varied from 0.3% to 2.7% of the main annulus mass flow rate. According to literature, the coolant flow rate is also expressed in terms of non-dimensional quantity $C_{w,c} = \dot{m}_c/\mu R_c$, where R_c is the radius at which the coolant is supplied. Then, $C_{w,c}$ is compared to the reference value corresponding to the non-dimensional mass flow rate entrained into a partial rotor $C_{w,ent}$. $C_{w,ent}$ has been calculated following equations described in section 2.2.4, where the inner radius a is the one of the

upstream cavity while the outer radius, named b, is the rim seal radius. Table 5.4 reports all the tested coolant flow rates in terms of percentage ratio of the main flow and of $C_{w,ent}$.

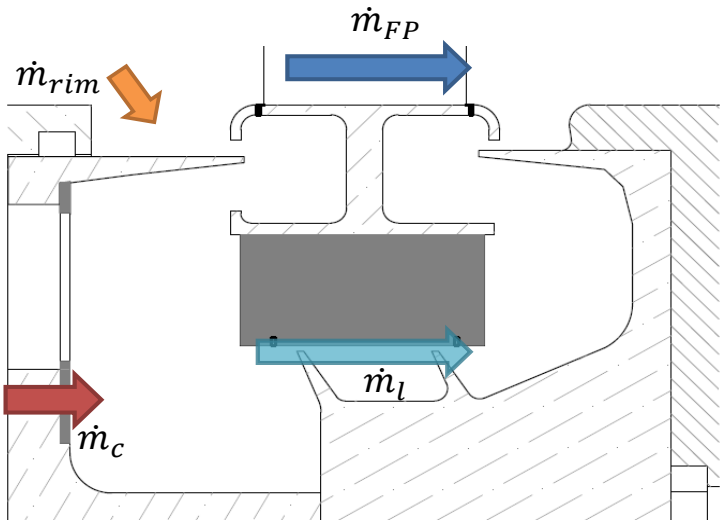

Figure 5.19 Representation of flows in the cavity

$Re = 100000 \;\; S_w = 0.7$									
$\dot{m}_c/\dot{m}_{FP}$ [%]	0.3	0.4	0.6	1	1.4	1.8	2.2	2.5	2.7
$C_{w,c}/C_{w,ent}$	0.4	0.5	0.8	1.3	1.8	2.3	2.9	3.3	3.5

Table 5.4 Test conditions

5.3.1 Static pressure distribution within the cavity

Figure 5.20 shows the static pressure distributions, in terms of non-dimensional pressure coefficient C_p (equation 5.03) measured along the static part of the cavity for different values of the coolant flow rates. To make further clear the distribution, the pressure tap location is indicated in the top right corner in figure 5.20. The square points represent the results for the no-coolant case and have been described previously. Introducing the coolant flow, the pressure measured by taps 2 to 8 increases significantly reducing the pressure difference with the first tap that is linked with the main flow pressure. As a consequence, the pressure drop across the labyrinth seal increases.

At the maximum coolant flow rate, the pressure in the fore part of the cavity becomes uniform and the pressure drop of the flow across the labyrinth seal is almost equal to the drop across the vane, hence the difference between the pressure coefficients upstream and downstream of the seal is identically 1.

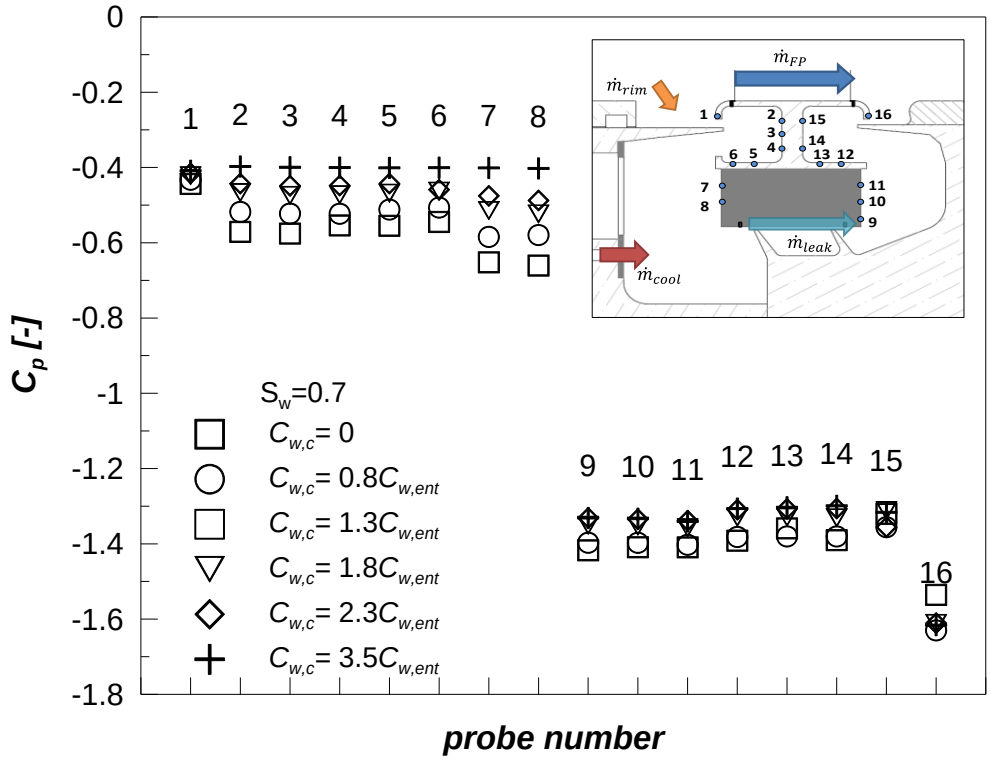

Figure 5.20 Influence of the coolant flow rate on the cavity T-bar static pressure distribution

5.3.2 Analysis of the leakage flow behavior

The effect of the coolant on the leakage flow behavior has been analyzed deriving the leakage mass flow rate for each condition. In addition, the time averaged mass flow rate that is ingested from the main annulus through the rim seal has been also evaluated. In the case without coolant flow, the flow demanded by the labyrinth seal is completely delivered by the main flow. Increasing the coolant flow rate, the rim flow results from the difference between the leakage flow rate and the coolant flow rate coherently with the scheme in figure 5.19. Hence:

$$\dot{m}_{rim} = \dot{m}_l - \dot{m}_c \tag{5.08}$$

The plot in figure 5.21 shows both the leakage and the rim seal mass flow rate in terms of percentage ratio with respect to the main flow mass flow rate. Very small variation of the leakage mass flow rate can be observed with increasing coolant flow rate, coherently to what observed in *Andreini et al. (2008)*. It slightly increases when $C_{w,c}/C_{w,ent} < 1$ and then starts to reduce but values remain very close to 2.7% of the main annulus mass flow for all the different conditions.

On the other hand, the rim seal mass flow rate reduces almost linearly. At the last condition, the cavity is completely sealed since the coolant flow rate is equal to the one demanded by the labyrinth seal, so that $\dot{m}_{rim} = 0$. We refer to this state as "*purged*" condition as it corresponds to the flow state condition characterized by an iso-pressure in the fore part of the cavity (see figure 5.20), that avoids ingestion of fluid from the main flow.

The purged condition is obtained for $C_{w,c}/C_{w,ent} = 3.5$, corresponding to $\dot{m}_c/\dot{m}_{FP} = 2.7\%$, according to table 5.4. It is worth mentioning that this value is almost three times higher than the one evaluated by *Coren et al. (2011)* using temperature measurements, for which the cavity is sealed with $C_{w,c}/C_{w,ent} = 1.13$.

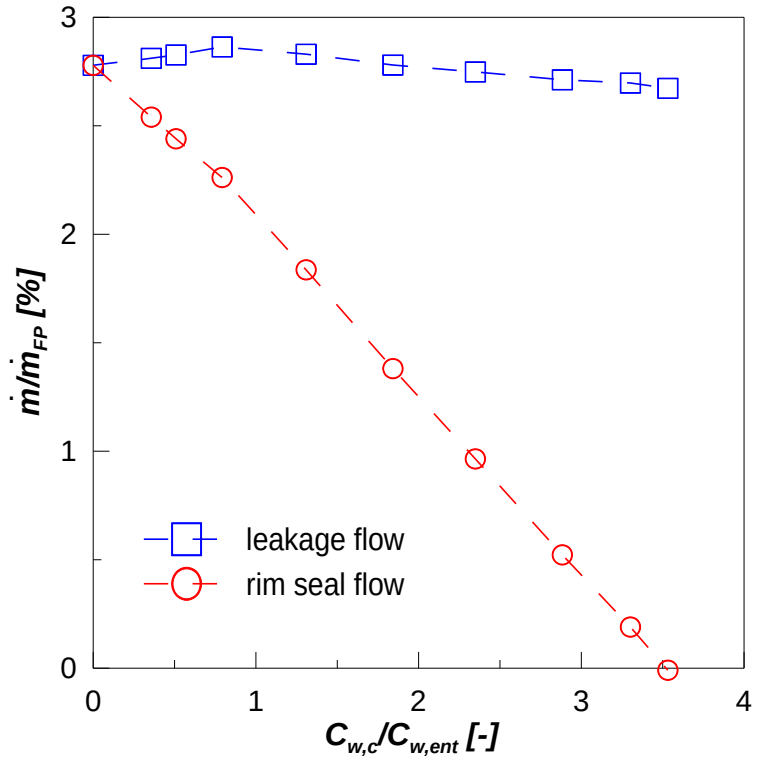

Figure 5.21 Leakage and rim seal mass flow rate variation due to different coolant flow rates

The discharge coefficient has been computed following the first definition introduced in section 5.2: the ideal mass flow rate has been derived by considering the effective pressure ratio β_{eff} of the labyrinth seal. Figure 5.22 provides the discharge coefficient as function of the non-dimensional coolant flow rate. It can be observed that as far as the ratio between the coolant flow and the entrainment flow rate remains lower than unity the discharge coefficient remains close to the no-coolant value ($C_D = 0.47$). Subsequently, the discharge coefficient drastically reduces to $C_D = 0.42$ at the highest coolant flow rate, corresponding to a 10% reduction with respect to the no-coolant value. The behavior of the discharge coefficient suggests that a sudden modification of the flow field occurs in the fore cavity when the coolant flow overcome the disk pumping capacity. This is in agreement with the observations of *Andreini et al. (2008)* reported in figure 2.15.

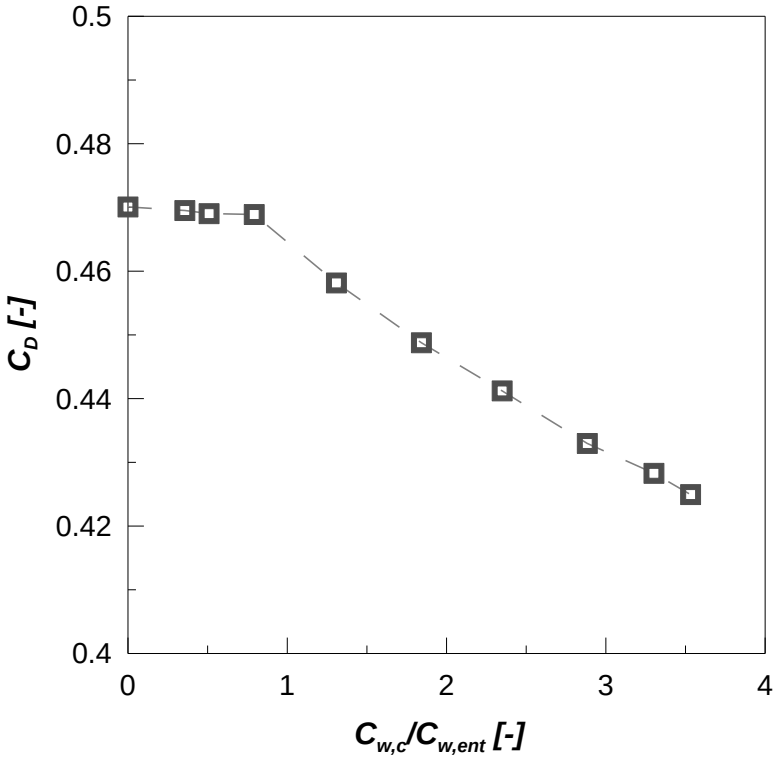

Figure 5.22 Discharge coefficient variation due to different coolant flow rates

5.4 Mainstream Total Pressure Distributions

The influence of rotation and the coolant flow rate on the interaction mechanism between the cavity and the main annulus flows has been investigated by measuring the total pressure distribution upstream and downstream of the vane row. Six different operating conditions have been considered for this analysis: three swirl factors ($S_w = 0.56, 0.7$ and 0.93 without coolant) to investigate the effect of rotation, and three different coolant flow rates (corresponding to 0.6%, 1.2% and 2.7% of the main annulus mass flow rate) at constant swirl factor of $S_w = 0.7$. The Reynolds number has been kept constant equal to 100000 for all tests.

The time mean total pressure distributions have been measured by means of the kiel probe and the traversing system described in the previous chapter. The measurement grid is constituted by 21 points equally distributed along one pitch of the vane and 21 points in the radial direction from the outer radius of the cavity ($r/R_{tip} = 0.895$) up to $r/R_{tip} = 0.984$, around 3 mm far from the tip endwall. A finer mesh has been applied to the hub endwall to provide a better description of the secondary flow structures near the cavity.

5.4.1 Effect of the disk rotational speed

Figure 5.23 shows the radial distribution of the pitch-wise averaged total pressure upstream of the vane. The total pressure is provided in terms of the non dimensional total pressure coefficient defined as:

$$C_{\overline{p_{t,1}}} = \frac{p_{amb} - \overline{p_{t,1}}(r)}{p_{amb} - \overline{p_{t,mid}}} \tag{5.09}$$

where the overbar denotes the pitchwise average, p_{amb} is the ambient pressure and $\overline{p_{t,mid}}$ is the averaged inlet total pressure at midspan.

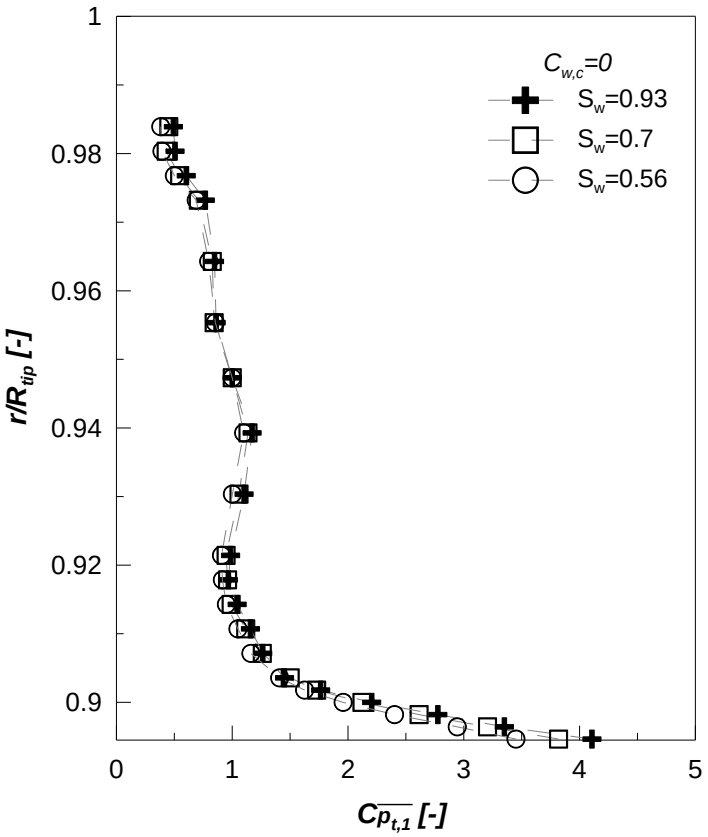

Figure 5.23 Pitchwise averaged total pressure distributions at the vane inlet plane: effect of the swirl factor

A low momentum region is observed close to the cavity entrance section located at $r/R_{tip} = 0.895$, and extends for 22% of the channel height. This portion of the fluid is indeed characterized by the interaction between the incoming boundary layer developing at the rotor hub and the low momentum flow just inside the cavity. Effects of the rotational speed variation appear negligible at the vane inlet plane.

The measurements, carried out in the vane outlet plane, are presented in figure 5.24 in terms of the total pressure coefficient defined as follows:

$$C_{p_t} = \frac{p_{t,1}(r,y) - p_{t,2}(r,y)}{0.5\rho v_{2,id}^2} \tag{5.10}$$

The upper term represents the difference between the inlet and outlet total pressure computed in each point of the measurement grid. The bottom term is the dynamic pressure associated to the exit velocity of an ideal isentropic fluid.

In figure 5.24 the rotational speed increases from left to right, hence the swirl factor reduces. The main features that can be observed, are the superposition of the wake and the secondary flow cores of the stator, and the relative modifications due to the cavity flow for the different swirl factors.

The vane wake is recognized by the green strip that extends for the whole radial domain around $y/g = 0.4$. A small bi-dimensional flow region is recognized around midspan, at $r/R_{tip} = 0.947$. High total pressure loss cores are identified close to the hub at $r/R_{tip} = 0.925$ and around $r/R_{tip} = 0.965$ and 0.98 close to the tip radius. They are the evidence of the secondary flow structures (passage and horse-shoe vortices) that develop through the vane row and transport the low momentum fluid coming from the endwall boundary layers at the vane exit section.

The modification of the swirl factor affects the secondary losses in the hub region. Indeed, the C_{p_t} values related to the passage vortex at the hub (located around $r/R_{tip} = 0.925$) increase as the swirl factor reduces, while their position moves slightly towards the hub. High values of the C_{p_t} are also observed close to the outlet radius of the cavity ($r/R_{tip} = 0.895$) along the entire pitch. In this region, a low momentum flow is generated as a consequence of the mixing process between the flow leaving the cavity and the incoming boundary layer of the main flow at the hub. In addition, the radial extension of the loss band and the loss magnitude decrease with smaller swirl factors.

A possible explanation to this behavior is given. As observed by *Kong et al. (2016)*, the higher the rotational speed of the rotor the higher the swirl of the downstream rim seal fluid in the direction of rotation. Then the higher tangential momentum of the fluid reduces the mixing losses in the hub region. This is consistent with the reduction of the total pressure coefficient observed with rotation near the hub. On the other hand, the swirled flow from the rim seal supply the passage vortex, then strengthen the viscous dissipation mechanism. This mechanism produces the higher total pressure losses observed with rotation in figure 5.24c.

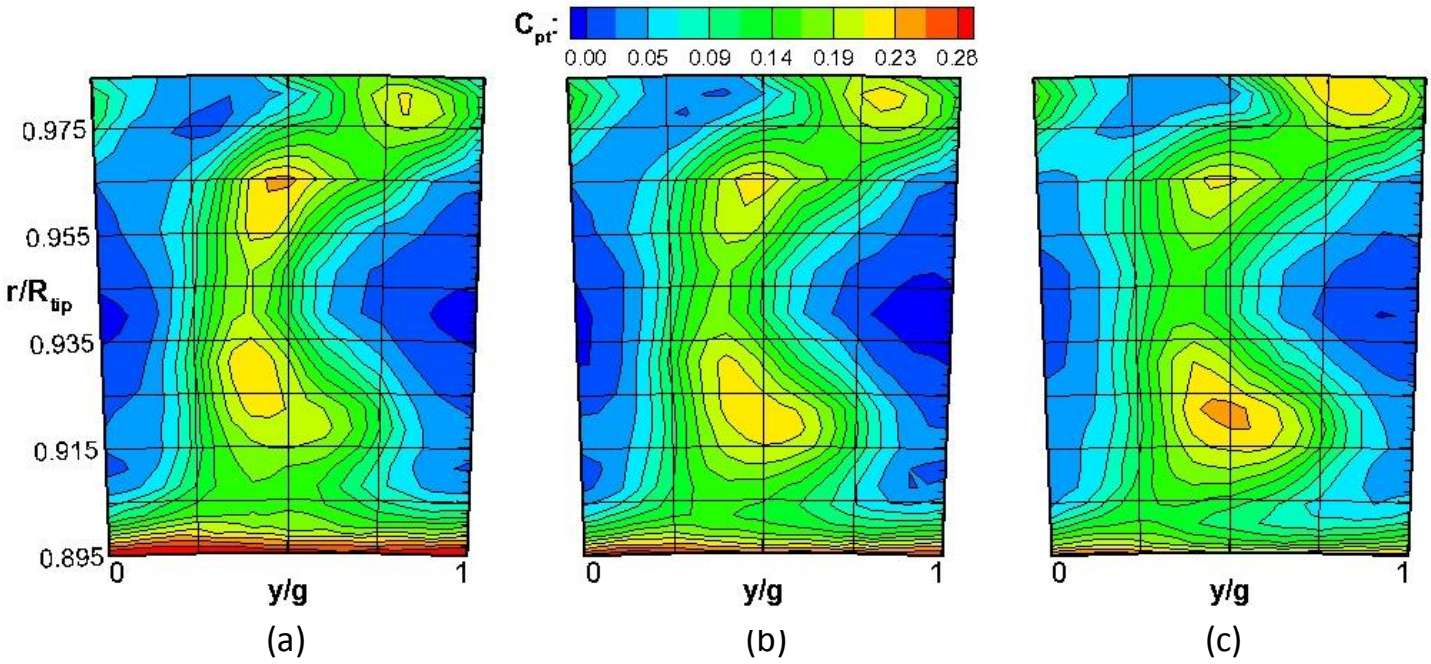

Figure 5.24 Total pressure coefficient distributions downstream of the vane for $S_w = 0.93$(a), $S_w = 0.7$(b) and $S_w = 0.56$(c)

The pitch-wise averaged total pressure coefficients are showed in figure 5.25, where:

$$C_{\overline{p_t}} = \frac{\overline{p_{t,1}}(r) - \overline{p_{t,2}}(r)}{0.5\rho v_{2,id}^2} \tag{5.11}$$

The loss core due to the vane passage vortex is located at $r/R_{tip} = 0.92$ which corresponds to 22% of the channel height. The vortex position keeps constant with the swirl factor while its strength decreases of about 15% from $S_w = 0.56$ to $S_w = 0.93$. The low total pressure coefficient band observed close to the cavity outlet occupies 15% of the channel height at $S_w = 0.93$ and reduces to 11% and 8% respectively for $S_w = 0.7$ and $S_w = 0.56$.

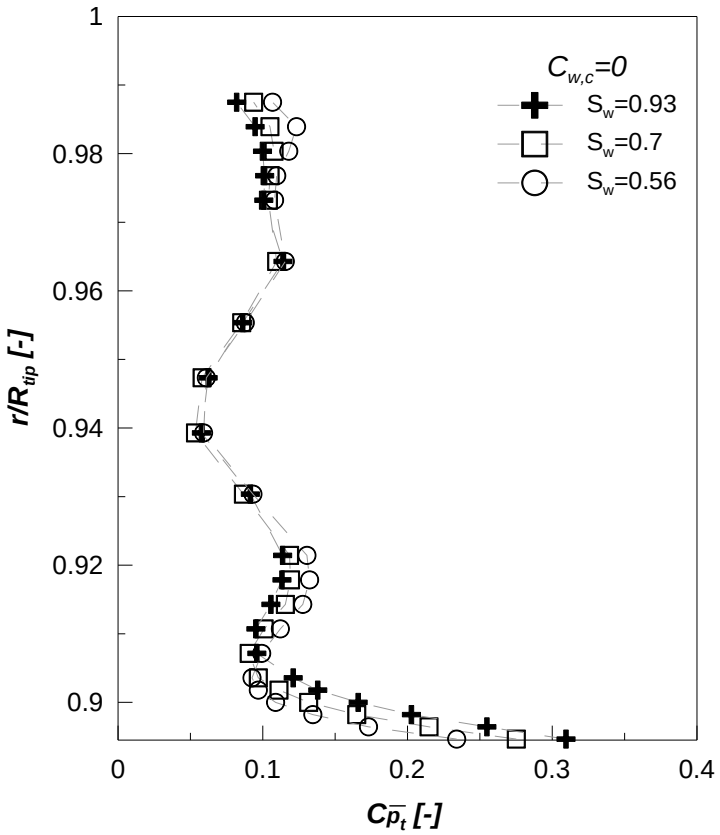

Figure 5.25 Pitchwise averaged total pressure distributions at the vane outlet plane: effect of the swirl factor

5.4.2 Effect of the coolant flow rate

The effect of the coolant for a fixed swirl factor on the upstream distribution of the pitchwise averaged total pressure $C_{\overline{p_{t,1}}}$ (see equation 5.09) is provided in figure 5.26. The distribution for the no-coolant case is also added to the plot for comparison (square points). It is evident that there is no significant variation between the different conditions, meaning that the effects of the coolant flow are negligible even at the highest coolant flow rate.

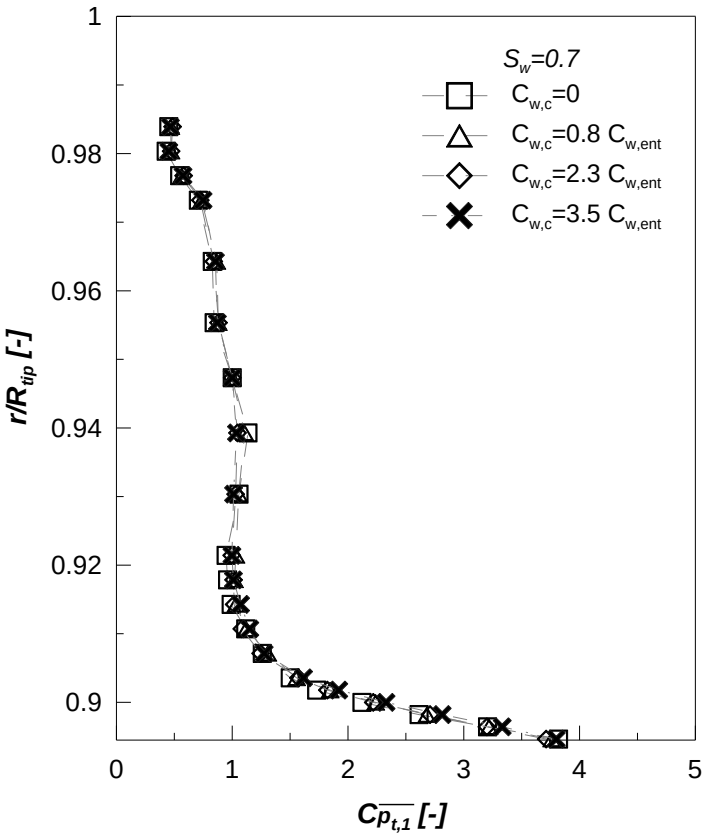

Figure 5.26 Pitchwise averaged total pressure distributions at the vane inlet plane: effect of the coolant flow rate

The contour plots of the total pressure coefficient C_{p_t} (equation 5.10) downstream of the vane are shown in figure 5.27. The distributions indicate a strong influence of the coolant flow rate on the total pressure loss mechanism. The reference case with $C_{w,c} = 0$ can be observed in figure 5.24b. The green strip revealing the presence of the vane wake can be identified again at $y/g = 0.4$ and the bi-dimensional flow field remains in the surround of $r/R_{tip} = 0.947$. Moreover, C_{p_t} values keep similar at midspan suggesting that the profile losses are not affected by the coolant flow rate, as expected.

The flow patterns around midspan appear unchanged with respect to the contour plots of figure 5.24b, while the effects of the coolant flow rate are observed in the region close to the hub. Increasing the coolant flow rate, the position of the secondary loss core moves towards the center of the channel and increases in strength as suggested by the higher values of the C_{p_t}, similarly to what observed in *Schrewe et al. (2012)* (see figure 2.23).

This latter is a consequence of the development of the flow near the endwall upstream and inside the vane row. The more coolant flow is delivered the less amount of flow from the main annulus is ingested into the cavity (see figure 5.21), thus a thicker boundary layer is expected

upstream of the vane. This intensifies the formation of the passage vortex as largely documented in literature. Conversely, the higher the coolant flow rate introduced into the cavity the higher the total pressure of the fluid leaving the cavity downstream of the cavity. This lead to the formation of a band close to the hub ($r/R_{tip} < 0.91$) where the C_{p_t} decreases with increasing coolant flow rate.

This behavior is likely a consequence of the swirl development of the cavity flow with the coolant. Figure 5.20 shows that increasing the coolant flow rate, the static pressure in the rear cavity remains almost unaltered. Since the coolant flow only marginally affects the leakage flow rate, the higher total pressure measured in that region is mainly related to a higher tangential momentum of the cavity flow. It means that the higher the coolant flow rate the higher the swirl of the flow in the rear cavity, coherently with the results of *Andreini et al. (2008)* presented in figure 2.16.

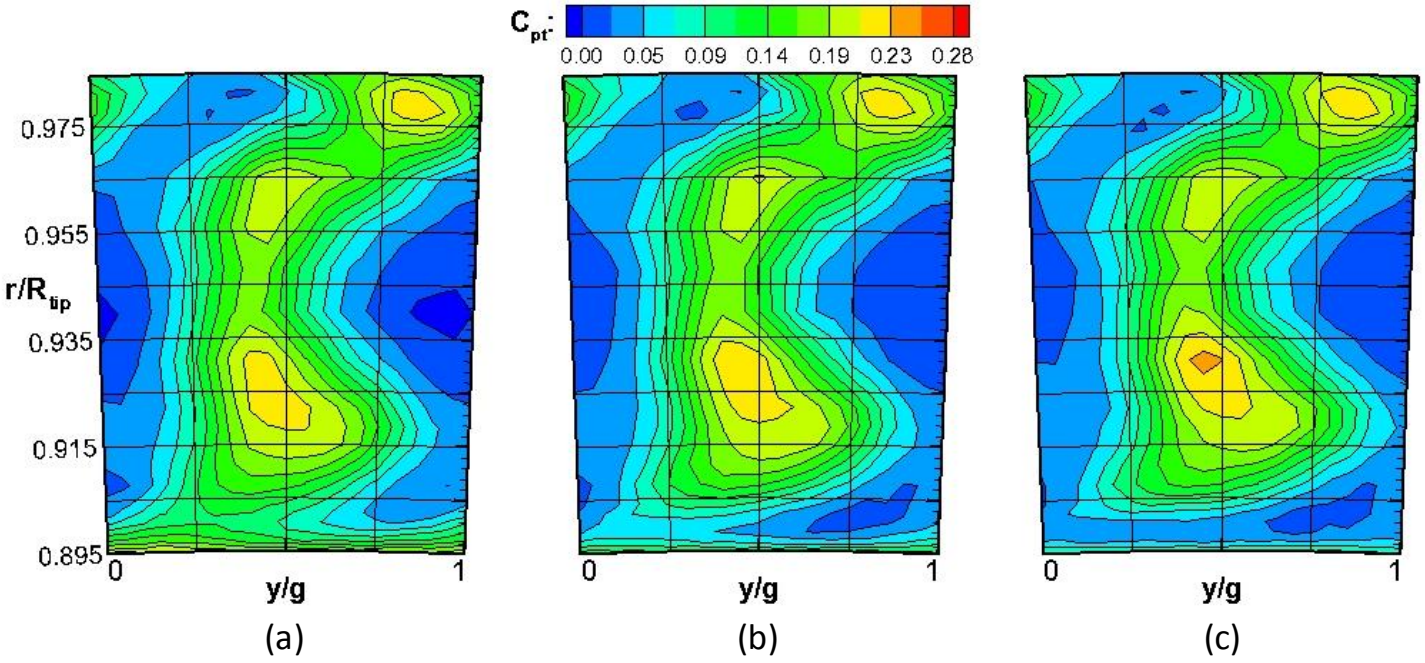

Figure 5.27 Total pressure coefficient distributions downstream of the vane for $C_{w,c} = 0.8C_{w,ent}$(a), $C_{w,c} = 2.3C_{w,ent}$(b) and $C_{w,c} = 3.5C_{w,ent}$(c)

Figure 5.28 shows the radial distributions of the pitchwise averaged total pressure coefficient. It makes further evident the previous observations. Radially, over $r/R_{tip} = 0.947$ the distributions are overlapped meaning that there is no effect of the coolant on the flow pattern in that region. Under this position, the loss core related to the passage vortex, located in the surround of $r/R_{tip} = 0.92$, becomes wider towards the center as the coolant flow rate increases. Closer to the rim seal, the diagram shows a gradual reduction of the minimum value of the total pressure coefficient and the shift of the peak position towards the hub. The minimum value of the $C_{\overline{p_t}}$ reduces to $C_{\overline{p_t}} = 0.03$ at $r/R_{tip} = 0.897$ for $C_{w,c}/C_{w,ent} = 3.5$ while, in the no-coolant case, we observe the minimum $C_{\overline{p_t}} = 0.09$ located at $r/R_{tip} = 0.907$. This behavior indicates that the interaction between the cavity flow and the main flow is also affected by the coolant. Particularly, the higher the coolant flow rate, the better the overall vane row efficiency.

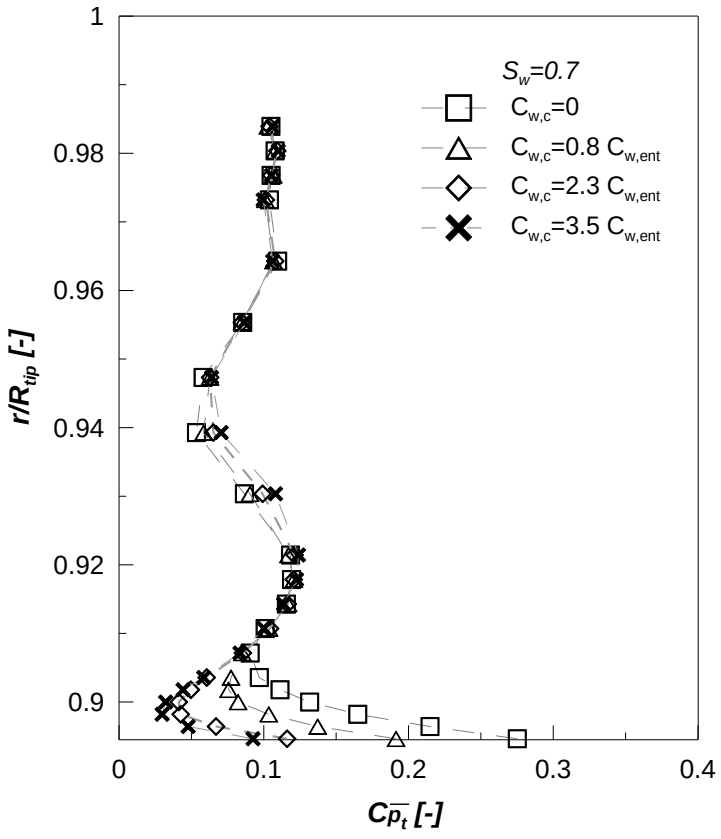

Figure 5.28 Pitchwise averaged total pressure distributions at the vane outlet plane: effect of the coolant flow rate

Chapter 6 - CONCLUSIONS

Throughout this Ph.D. thesis a new rig has been designed and commissioned at the Aerodynamics and Turbomachinery Laboratory of the University of Genova. The rig is a large scale one-and-half stages, rotating test facility, opportunely designed to reproduce the main features characterizing the cavity flows developing in real low pressure turbine modules of aero-engines. The test section is constituted by a realistic cavity configuration (scaled *1.5:1* with respect to the engine) installed in the bottom of a LP turbine vane row.

The rig has been heavily instrumented in order to provide a deeply characterization of the flow field that establishes within a LPT interstage cavity and its interaction with the main flow path. Large efforts have been made to develop a calibration procedure for evaluating the leakage mass flow rate during the tests. Particularly, calibration functions linking the mass flow rate to the pressure drop across the labyrinth fins and the swirl factor have been obtained running tests in a modified configuration of the facility.

The tests have been carried out in largely subsonic conditions as the vane expansion ratio has been kept lower than 1.1. The rotational and viscous effects have been investigated by reproducing a wide range of Reynolds numbers and swirl factors. The influence of the coolant has been analyzed by delivering several flow rates into the cavity. The results are grouped into four blocks depending on their specific objective:

1. Characterization of the mainstream and cavity aerodynamics;
2. Estimation of the cavity discharge coefficient;
3. Investigation of the coolant related effects on the cavity aerodynamics;
4. Measurements of the mainstream total pressure distributions;

The first kind of results are aimed at characterizing the flow field in the main annulus and inside the cavity. Measurements of the static pressure distributions in the main flow path and the labyrinth seal show a strong axial symmetry of the flow developing into the rig during tests. The sinuous distributions of the static pressure measured in the main annulus endwalls show the potential effects of the vane leading edge and trailing edge upstream and downstream of the vane, respectively. These distributions are not affected by the rotational speed variation. The vane aerodynamic loadings are measured at 50%, 25% and 10% of the span height. A slight decrease of the pressure distribution in the fore part of the suction side id observed as the swirl factor reduces. The rear part of the suction side and the entire pressure side remain uninfluenced. The measurements of the static pressure distributions inside the cavity reveal that the main pressure drop is provoked by the labyrinth seal fins. The minor drops are due to

the rim seals at the cavity inlet and exit sections. A substantial independence from the rotational speed variation is revealed.

The second kind of results provide the evaluation of the cavity discharge coefficient for different operating conditions in terms of Reynolds numbers and swirl factors. The Reynolds number has been varied from 100000 to 200000 and five different swirl factors are considered between 0.56 and 0.93. Two different definitions of the ideal mass flow rate have been used to compute the C_D. The first allows a direct comparison with literature works concerning labyrinth seals, the second being defined with vane boundary conditions, is more useful for designers. The C_D defined according to literature shows values in the surround of 0.48 and are in agreement with available data for both stationary and rotating operative conditions. Conversely, the discharge coefficient defined using the total to static pressure ratio of the fluid evolving across the vane shows lower values with respect to the previous case. Also, a less dependence with rotation is observed even at low Reynolds numbers.

Furthermore, the effect of the coolant has been investigated for a constant swirl factor and Reynolds number, namely $S_w = 0.7$ and $Re = 100000$. Results indicate that increasing the coolant flow rate, the amount of leakage flow keeps almost constant and the flow ingested from the main annulus decreases linearly. The cavity resulted completely sealed when the coolant flow rate equalizes the leakage flow rate demanded by the labyrinth seal, thus with $\dot{m}_c/\dot{m}_{FP} = 2.7\%$, which corresponds to $C_{w,c}/C_{w,ent} = 3.5$. In this condition, the pressure level in the fore part of the cavity becomes uniform, equal to the value measured by the first tap located in correspondence of the outer radius of the cavity. The discharge coefficient remains close to the no-coolant value as far as $C_{w,c}/C_{w,ent} < 1$. Then, it drastically reduces to $C_D = 0.42$ at the "*purged*" condition suggesting that a sudden modification of the flow field in the cavity occurs when $C_{w,c}/C_{w,ent}$ becomes larger than 1.

The kiel probe measurements in the main annulus upstream and downstream of the vane clearly highlight the modification of the secondary flow structures for the different conditions tested. In the case without coolant, the loss core related to the hub passage vortex intensifies as the rotational speed is increased, while the low momentum flow region at the cavity exit becomes thinner. Apparently, both are a consequence of a higher tangential momentum of the rim seal fluid downstream of the vane, provoked by higher rotational speeds. Increasing the tangential momentum, the mixing losses reduces in the hub region whereas the viscous dissipation due to the passage vortex intensifies. The coolant modifies this flow pattern moving the loss core towards higher radius. In addition, its strength is observed to intensify at higher coolant flow rates, likely due to a thicker boundary layer at the vane inlet plane. The peak of $C_{\overline{p_t}}$ inside the low momentum region is shifted towards inner radius with increasing

coolant flow rates. In addition, the peak value is observed to increase due to an increasing tangential momentum of the rim seal fluid with increasing coolant flow rate.

All the results provide evidence of the capabilities of the test rig designed to reproduce the main features characterizing cavity flows in real turbines for aeroengine applications. In the end, this work gives a major understanding of the complex flow evolving into rotor-stator cavities in gas turbines and of its interaction with the main annulus flow. This latter is of great importance for evaluating the performances of the subsequent blade row and thus should be properly accounted for in design phases and reproduced as inlet conditions in cascade testing.

BIBLIOGRAPHY

[1] J. M. Owen e R. H. Rogers, Flow and Heat Transfer in Rotating-Disc Systems, 1989.

[2] N. Gregory, J. T. Stuart e W. S. Walker, «On the stability of three-dimensional boundary layers with application to the flow due to a rotating disk,» *Philosophical Transactions of the Royal Society of London A: Mathematical, Physical and Engineering Sciences,* vol. 248.943, pp. 155-199, 1955.

[3] J. W. Chew, «The Effect of Hub Radius on th eFlow Due to a Rotating Disc,» *Journal of Turbomachinery,* vol. 110, pp. 417-418, 1998.

[4] J. W. Daily e R. E. Nece, «Chamber Dimension Effects on Induced Flow and Frictional Resistance of Enclosed Rotating Disks,» *Journal of Basic Engineering,* vol. 82, pp. 217-232, 1960.

[5] K. Stewartson, «On the flow between two rotating coaxial disks,» *Mathematical Proceedings of the Cambridge Philosophical Society,* vol. 49, n. 2, pp. 333-341, 1953.

[6] A. S. Sambo, A theoretical and experimental study of the flow between a rotating and a stationary disc, PhD Thesis. University of Sussex., 1983.

[7] U. P. Phadke e J. M. Owen, «Aerodynamic aspects of the sealing of gas-turbine rotor-stator systems: part 1: the behavior of simple shrouded rotating-disk systems in a quiescent environment,» *International journal of heat and fluid flow,* vol. 9, n. 2, pp. 98-105, 1988.

[8] J. M. Owen, «Prediction of Ingestion Through Turbine Rim Seals—Part I: Rotationally Induced Ingress,» *Journal of Turbomachinery,* vol. 133(3), 2011.

[9] U. P. Phadke e J. M. Owen, «Aerodynamic Aspects of the Sealing of Gas-Turbine Rotor-Stator Systems: Part 3: The Effect of Nonaxisymmetric External Flow on Seal Performance,» *International journal of heat and fluid flow,* vol. 9, n. 2, pp. 113-117, 1988.

[10] J. M. Owen, «Prediction of Ingestion Through Turbine Rim Seals—Part II: Externally Induced and Combined Ingress,» *Journal of Turbomachinery,* vol. 133(3), 2011.

[11] P. R. Childs, Rotating flow, Elsevier, 2010.

[12] W. Gartner, «A prediction method for the frictional torque of a rotating disc in a stationary housing with superimposed radial outflow,» in *ASME paper(97-GT),* 1997.

[13] D. Eastwood, D. D. Coren, C. A. Long, N. R. Atkins, P. R. N. Childs, T. J. Scanlon e A. Guijarro-Valencia, «Experimental Investigation of Turbine Stator Well Rim Seal, Re-Ingestion and Interstage Seal Flows Using Gas Concentration Techniques and Displacement Measurements,» *Journal of Engineering for Gas Turbines and Power,* vol. 134(8), p. 082501, 2012.

[14] F. J. Bayley e J. M. Owen, «The fluid dynamincs of a shrouded disk system with a radial outflow of coolant,» *Journal of Engineering for Power,* vol. 92, pp. 335-341, 1970.

[15] U. P. Phadke e J. M. Owen, «Aerodynamic aspects of the sealing of gas-turbine rotor-stator systems: Part 2: The performance of simple seals in a quasi-axisymmetric external flow,» *International journal of heat and fluid flow,* vol. 9, n. 2, pp. 106-122, 1988.

[16] K. Willenborg, S. Kim e S. Witting, «Willenborg, K., Kim, S., & Wittig, S. (2001). Effects of Reynolds number and pressure ratio on leakage loss and heat transfer in a stepped labyrinth seal,» *Journal of Turbomachinery,* vol. 123(4), pp. 815-822, 2001.

[17] X. Kong, G. Liu, Y. Liu e Q. Feng, «Kong, X., Liu, G., Liu, Y., & Feng, Q. (2016, June). Investigation on the Leakage Flow, Windage Heating and Swirl Development of Rotating Labyrinth Seal in a Compressor Stator Well,» in *ASME Turbo Expo 2016: Turbomachinery Technical Conference and Exposition,* 2016.

[18] S. Witting, L. Dorr e S. Kim, «Scaling effects on leakage losses in labyrinth seals,» *Journal of Engineering for Power* , vol. 105, n. 2, pp. 305-309, 1983.

[19] S. Wittig, U. Schelling, S. Kim e K. Jacobsen, «Numerical predictions and measurements of discharge coefficients in labyrinth seals,» in *ASME paper, 87,* 1987.

[20] H. Zimmermann e K. H. Wolff, «Air system correlations, Part 1: Labyrinth seals,» in *ASME paper 98-GT*, 1998.

[21] J. K. Denecke, K. Dullenkopf e S. Witting, «Influence of preswirl and rotation on labyrinth seal leakage,» in *Proceedings of the Tenth International Symposium on Transport Phenomena and Dynamics of Rotating Machinery*, 2004.

[22] S. Witting, T. Geis, V. Schramm e K. Willenborg, «Technical Report: Innovative Konzepte zu Wärmehaushalt und Dichtungen von Triebwerken – Teil 3: Durchfluß und Wärmeübergang in Labyrinth-dichtungen mit Honeycomb-Anstreifbelägen,» Institut für Thermische Strömungsmaschinen, Universität Karlsruhe, TH, 1999.

[23] M. F. Blair, «Influence of Free-Stream Turbu-lence on the Turbulent Boundary Layer Heat Transfer and Mean Profile Development, Part II Analysis of the results,» *ASME Journal of Heat Transfer,* vol. 105, pp. 41-45, 1983.

[24] W. Waschka, S. Witting e S. Kim, «Influence of high rotational speeds on the heat transfer and discharge coefficients in labyrinth seals,» *Journal of Turbomachinery*, vol. 114(2), pp. 462-468, 1992.

[25] J. Denecke, K. Dullenkopf, S. Witting e H. J. Bauer, «Experimental investigation of the total temperature increase and swirl development in rotating labyrinth seals,» in *ASME Turbo Expo 2005: Power for Land, Sea, and Air. American Society of Mechanical Engineers*, 2005.

[26] J. Denecke, J. Färber, K. Dullenkopf e H. J. Bauer, «Interdependence of discharge behavior, swirl development and total temperature increase in rotating labyrinth seals,» in *ASME Paper No. GT2008-51429*, 2008.

[27] J. Denecke, J. Färber, K. Dullenkopf e H. J. Bauer, «Dimensional analysis and scaling of rotating seals,» 2005.

[28] J. A. Dixon, A. G. Valencia, D. Coren, D. Eastwood e C. Long, «Main Annulus Gas Path Interactions—Turbine Stator Well Heat Transfer,» *Journal of Turbomachinery*, vol. 136, n. 2, 2014.

[29] J. A. Dixon, I. L. Brunton, T. J. Scanlon, G. Wojciechowski, V. Stefanis e P. R. Childs, «Turbine stator well heat transfer and cooling flow optimisation,» in *ASME Paper No. GT2006-90306.*, 2006.

[30] J. Pohl, J. A. Dixon e V. Fico, «Turbine Stator Well Cooling: Improved Geometry Benefits,» in *ASME Turbo Expo 2015: Turbine Technical Conference and Exposition (pp. V02CT45A008-V02CT45A008)*, 2015.

[31] A. Andreini, R. Da Soghe, B. Facchini e S. Zecchi, «Turbine stator well CFD studies: effects of cavity cooling air flow,» in *Proceedings of the ASME Turbo Expo*, 2008.

[32] A. Andreini, R. Da Soghe e B. Facchini, «Turbine stator well CFD studies: Effects of coolant supply geometry on cavity sealing performance,» *Journal of Turbomachinery*, vol. 133, n. 2, 2011.

[33] J. Pueblas, R. Corral e S. Schrewe, «Interaction of Rim Seal and Main Annulus Flow in a Low-Speed Turbine Rig,» in *ASME Turbo Expo 2013: Turbine Technical Conference and Exposition*, 2013.

[34] S. Schrewe, H. Werschnik e H. P. Schiffer, «Experimental analysis of the interaction between rim seal and main annulus flow in a low pressure two stage axial turbine,» *Journal of Turbomachinery*, vol. 135(5), p. 051003, 2013.

[35] D. D. Coren, N. R. Atkins, D. Eastwood, P. R. N. Childs, A. Gujarro-Valencia e J. A. Dixon, «The Influence of Turbine Stator Well Coolant Flow Rate and Passage Configuration on Cooling Effectiveness,» in *ASME*, 2011.

[36] D. D. Coren, N. R. Atkins, J. R. Turner, D. E. Eastwood, S. Davies, P. R. N. Childs, J. Dixon and T. S. Scanlon, "An advanced multi-configuration stator well cooling test facility," in *PROCEEDINGS OF THE ASME TURBO EXPO*, 2010.

[37] J. Gier, B. Stubert, B. Brouillet e L. De Vito, «Interaction of shroud leakage flow and main flow in a three-stage LP turbine,» *Journal of Turbomachinery*, vol. 127(4), pp. 649-658, 2005.

[38] A. M. Wallis, J. D. Denton e A. A. J. Demargne, «The control of shroud leakage flows to reduce aerodynamic losses in a low aspect ratio, shrouded axial flow turbine,» ASME Turbo Expo 2000: Power for Land, Sea, and Air.

[39] J. H. P. Ong, R. J. Miller e S. Uchida, «The Effect of Coolant Injection on the endwall Flow of a High Pressure Turbine,» *Jpurnal of Turbomachinery*, vol. 134, n. 5, p. 051003, 2012.

[40] S. Zerobin, A. Peters, S. Bauinger, A. Ramesh, M. Steiner, F. Heitmair e E. Gottlich, «The behavior of turbine center frames under the presence of purge flows,» in *ASME Turbo Expo 2017: Turbomachinery Technical Conference and Exposition*, 2017.

[41] K. Reid, J. Denton, G. Pullan, E. Curtis e J. Longley, «The effect of stator-rotor hub sealing flow on the mainstream aerodynamics of a turbine,» in *ASME turbo expo 2006: power for land, sea, and air*, 2006.

[42] S. D. Hunter e S. R. Manwaring, «Endwall Cavity Flow Effects on Gaspath Aerodynamics in an Axial Flow Turbine: Part I—Experimental and Numerical Investigation,» in *ASME paper 2000-GT (2000): 651.*.

[43] S. D. Hunter e S. R. Manwaring, «Endwall Cavity Flow Effects on Gaspath Aerodynamics in an Axial Flow Turbine: Part 2–Source Term Model Development,» in *ASME paper 2000-GT 513*, 2000.

[44] J. Denton e N. A. Cumpsty, «Loss Mechanism in Turbomachinery,» *Journal of Turbomachinery*, vol. 115, n. 4, pp. 621-656, 1993.

[45] S. R. Wellborn e T. H. Okiishi, «The influence of shrouded stator cavity flows on multistage compressor performance,» *Journal of Turbomachinery,* vol. 121(3), pp. 486-497, 1999.

[46] R. Schädler, A. I. Kalfas, R. S. Abhari, G. Schmid, T. auf dem Kampe e S. B. Prabhu, «Novel high-pressure turbine purge control features for increased stage efficiency,» in *GPPF 2017*, 2017.

[47] H. Pfeil e J. Eifler, «Turbulenzverhältnisse Hinter Rotierenden Zylindergittern,» *Forschung im Ingenieurwesen*, vol. 42, pp. 27-32, 1976.

[48] N. M. Opoka e H. P. Hodson, «Transition on the T106 LP turbine blade in the presence of moving upstream wakes and downstream potential field,» *Journal of turbomachinery,* vol. 130(4), n. 041017, 2008.

[49] M. Vera e H. Hodson, «Low Speed vs High Speed Testing of LP Turbine Blade-Wake,» in *The 16th Symposium on Measuring Techniques in Transonic and Supersonic Flow in Cascades and Turbomachines*, 2002.

[50] M. Berrino, D. Simoni, M. Ubaldi, P. Zunino e F. Bertini, «Off-Design Performance of a Highly Loaded Low Pressure Turbine Cascade Under Steady and Unsteady Incoming Flow Conditions,» *ASME Journal of Turbomachinery,* vol. 137, 2017.